# USING LONG- AND SHORT-LIVED SEDIMENT-ASSOCIATED ISOTOPES TO TRACK EROSION AND SEDIMENT MOVEMENT THROUGH RIVERS IN YUNNAN, SW CHINA

A Thesis Presented

by

Thomas Bundgaard Neilson

to

The Faculty of the Graduate College

of

The University of Vermont

In Partial Fulfillment of the Requirements
For the Degree of Master of Science
Specializing in Geology

January 2016

Defense Date: September 3, 2015
Thesis Examination Committee:

Paul Bierman, Ph.D., Advisor
Donna Rizzo, Ph.D., Chairperson
Andrea Lini, Ph.D.
Cynthia J. Forehand, Ph.D, Dean of the Graduate College

# Abstract

This research aims to understand the natural and human influences on erosion in three tributary watersheds to the Mekong River, Yunnan Province, China and to assess the utility of a novel application of isotopic indicators of erosion. It explores how erosion varies through time and space as a function of physical characteristics of the landscape, tectonic forces, and human alteration of the landscape for forestry and agriculture. To accomplish these goals, I use four sediment-associated radionuclides: *in situ* $^{10}$Be, meteoric $^{10}$Be, $^{210}$Pb$_{ex}$, and $^{137}$Cs. These isotopes accumulate in or on sediment grains, and each accumulates to a different depth on the landscape and has a different half-life. Thus, the isotopes can be used to track sediment as it moves across Earth's surface, each providing unique insight into processes occurring over a certain time period (from ~50 to 50,000 years) or eroding to a certain depth on the landscape.

The studied watersheds range from 22° to 27° N latitude, and from 200 to 2500 km$^2$ in area. I collected 54 samples of river-borne sediment within the three study watersheds, and measured the concentration of each isotope in every sample. In addition to the measured isotopic concentrations, I utilize on over 20 years of daily sediment yield data at the outlet of each watershed, hillslope steepness, normalized channel steepness ($k_{sn}$), contemporary land-use data, elevation, and 56 years of mean annual precipitation data (MAP).

Long-term erosion rates scale with topographic parameters in two of the three study basins, indicating that topography, or the underlying tectonic forces responsible for topography, control erosion rates over the past 6,000 to 50,000 years. Isotopic data also show that contemporary erosion is higher in cultivated areas than un-cultivated areas, a direct result of agricultural practices. Contemporary sediment yield, however, has not increased notably due to land-use change; however, under-representation of large stochastic events and sediment trapped by agriculture have reduced sediment yield relative to the long-term average in two of the studied watersheds.

Overall, the data imply changes in contemporary erosion that are consistent with Chinese policies that promoted deforestation from the 1950's to the late 1980's and conservation from the late 1990's to present. This proves to be a significant finding, as the result of the top-down approach China has taken with conservation policy has been widely called into question in previous studies.

While each isotope has the potential to provide unique information regarding erosional processes, *in situ* $^{10}$Be and $^{210}$Pb$_{ex}$ proved to be the most useful, while meteoric $^{10}$Be was the most challenging to utilize. Though interpretation is complex, measuring all four isotopes on the same sediment samples helps to fully realize the potential of *in situ* $^{10}$Be to estimate background erosion by simultaneously allowing for assessment of contemporary and human induced erosion.

## Acknowledgements

The research and work I present here would not have been possible without the continued support, guidance, and wisdom of a number of wonderful people I have been fortunate enough to find in my life, academic and otherwise. Chief among them are my advisors, Paul Bierman and Amanda Schmidt. Thank you both for your insight, support, and patience throughout this process. Dylan Rood was the source of significant wisdom, particularly when it came time to measure and interpret data on the AMS. My committee members, Andrea Lini and Donna Rizzo, are also well deserving of thanks for their contribution to my success. I would also like to acknowledge Will Ouimet and Veronica Sosa Gonzalez for their productive and insightful contributions as co-authors on the manuscript that makes up the body of this thesis.

The financial support of National Science Foundation grants EAR-1114166 to Amanda Schmidt, EAR-1114159 to Paul Bierman, and EAR-1114436 to Dylan Rood were critical to all aspects of my research, from fieldwork to presenting at conferences.

Thanks to all of my fellow graduate students in geology at UVM, past and present, who have been the sources of invaluable information, criticism, motivation, entertainment, and friendship during my time at the University of Vermont.

I want to extend my deepest appreciation to those close to me who have constantly asked me about my research, provided a willing ear, a willing distraction, or motivation to keep at it. Of course my parents, Pia and Will, are due particular recognition in these regards, but certainly not at the expense of those others who have given their time and energy as well.

# Table of Contents

# List of Tables

**Chapter 2: Manuscript for *Journal of Geophysical Research: Earth Surface***

# List of figures

## Chapter 1: Introduction



## Chapter 2: Manuscript for *Journal of Geophysical Research: Earth Surface*

# Chapter 1: Introduction

## 1 Motivation and project goals

Humans have become one of the most effective geomorphic agents on the planet, altering 54% of the total land area on Earth, with agriculture and forestry accounting for 47% of that alteration [*Hooke*, 2012]. Large quantities of sediment are mobilized and redistributed by human alteration of the landscape, often supplanting significantly slower and more diffuse geomorphic processes that would otherwise govern sediment movement across Earth's surface [*Hooke*, 1994]. Until relatively recently, basin-scale rates of erosion were difficult to quantify, often relying upon inaccurate estimates from fluvial sediment yield [*Trimble*, 1977]. With the discovery and refinement of methods that utilize radioactive isotopes as tracers for sediment movement, the past several decades have seen a boom in the number of studies that seek to quantify erosion at the basin-scale [cf., *Willenbring and von Blanckenburg*, 2010; *Portenga and Bierman*, 2011; *Matisoff and Whiting*, 2012].

Here, I build upon an expanding body of research aimed at untangling the variable influence of natural and human processes on erosion of Earth's surface through the application of multiple sediment associated isotopes. To accomplish this goal, I measured excess $^{210}Pb$ (referred to as $^{210}Pb_{ex}$), $^{137}Cs$, *in situ* $^{10}Be$ (referred to as $^{10}Be_i$), and meteoric $^{10}Be$ (referred to as $^{10}Be_m$) on fluvial sediment collected from three tributaries of the Mekong River, in Yunnan Province, southwest China (Figure 1). Accompanying the isotopic measurements I also use over 20 years of daily suspended sediment yield data at the outlet of each watershed, remotely sensed land-use data, 56 years of mean annual

precipitation (referred to as MAP) records, normalized channel steepness (referred to as $k_{sn}$), and hillslope angle. I utilize the unique soil depth profiles and half-lives of each isotope in conjunction with the sediment yield, land-use, and physiographic data to determine what erosional processes dominate over the short- and long-term and how humans have perturbed the natural system.

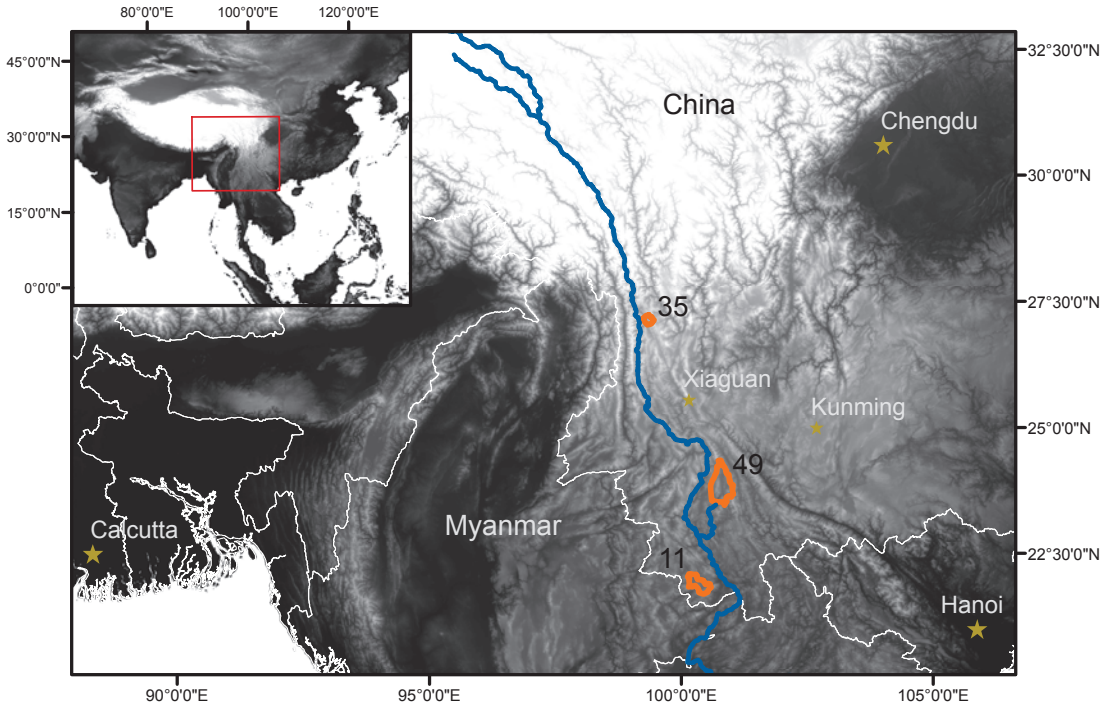


**Figure 1.** A map showing the location of the study basins within the general region overlain on a digital elevation model. The study basins are outlined in orange, while the Mekong River and selected tributaries are shown in blue. The inset in the top right places the study area in the context of Southeast Asia.

I address several geologically and societally relevant questions. First, I quantify how well fluvial sediment is mixed at river junctions and explore why sediment does not always mix well. Fully homogenized sediment is a critical component to basin-scale studies that rely on sediment transported by rivers. Second, I determine the primary

controls on long- and short-term erosion (averaged over ~6,000 – 50,000 yr and ~50 – 100 yr, respectively) in each watershed using quantitative and qualitative methods. Understanding how erosion changes through time is key to contextualizing the influence of humans, climate change, or other processes on the landscape. Third, I place the information gleaned from erosion analysis in the context of national changes in China's land-use policies, showing that multiple isotopic techniques can be used to directly assess the effectiveness of resource management plans. Finally, I address the relative merit of measuring all four isotopes on the same samples of fluvial sediment as a method for assessing erosion over a range of timescales. The application of all four isotopic systems used here on the same samples is a novel attempt at increasing the spatial and temporal resolution of erosion studies. It builds upon previous work leveraging one or two of these isotopes and is one of the first studies to combine all four isotopes.

## 2 Geographic background

### *2.1 Study sites*

The Mekong River watershed flows from the southeastern Tibetan plateau east and south to its outlet in the South China Sea and is situated between the Salween River to the west and the Yangtze River to the east. The samples included in this research are from the Yongchun (198 $km^2$), Weiyuan (2508 $km^2$), and Nankai (1006 $km^2$) Rivers, however, I refer to them by the ID's assigned by *Schmidt et al.* [2011]: basins 35, 49, and 11, respectively. Basins 35 and 49 are within the Lanping Simao unit, a component of the Indochina crustal extrusion, and primarily composed of thick terrestrial Jurassic and early

Cenozoic redbeds [*Akciz et al.*, 2008]. Basin 11 is within the Chengling-Mengliang and Linchang units, a component of the Sibumasu crustal extrusion, and primarily composed of low to high-grade metamorphic rocks [*Akciz et al.*, 2008]. The region is dominated by east-west trending right-lateral strike-slip faults accommodating the northward movement of India relative to China with smaller normal and reverse faults in certain areas [*Burg et al.*, 1997]. Previous studies have used $^{10}$Be to estimate millennial scale erosion rates in the Mekong River Basin that range from 0.1-0.4 mm yr$^{-1}$, with the highest erosion rates found in the narrowest portion of the Mekong River corridor [*Henck et al.*, 2011]. Monsoon rains from May – October account for > 80% of the precipitation in the region, and the study basins experience less precipitation in the north and greater precipitation in the south [*Fan et al.*, 2013].

### *2.2 Overview of contemporary Chinese land-use policy*

Human over-use of the landscape in China was recorded as early as the 11$^{th}$ century [*Elvin*, 2004], and modern exploitation of the landscape is often met with concern over environmental degradation. During the 50 – 60 year transition from insular Communist China to the current manifestation of Chinese communism, Chinese forests were subject to three major clearance events, sometimes referred to as the "Three Great Cuttings" [*Trac et al.*, 2007]. The first of the cuttings began with the Great Leap Forward in 1958, when forests were collectivized and harvested as an energy source for the small-scale production of steel. The Cultural Revolution, from 1966 – 1976, brought about the second of the cuttings as forests were converted to agricultural land to support the rapidly

increasing population. The transition to a market economy in the early 1980's spurred the third cutting, as forests were returned to individual control and timber production became a profitable industry [*Hyde et al.*, 2003].

Continued recognition of the risk of environmental degradation due to land-use practices during and after the Three Great Cuttings resulted in sporadic attempts at policy to mitigate the impacts of forest clearance, however, meaningful results were not widely achieved until after a devastating flood in the Yangtze River in 1998 that claimed over 3000 lives [*Trac et al.*, 2007]. In 2000 the Chinese government implemented the Natural Forest Protection Program to restore damaged forests and protect remaining forestland, which included a ban on logging in much of SW China [*Trac et al.*, 2007]. In 2001, the "Returning Farmland to Forest" program was rolled our nationally, incentivizing the conversion of agricultural land back to forest, particularly on slopes greater than 25°, marking one of the largest conservation programs in the world [*Trac et al.*, 2007; 2013]. Both policies identified erosion and flood mitigation as primary goals of landscape restoration. Official government results claim nearly all benchmarks for success were met or exceeded, however, several small-scale studies have cast doubt on the veracity of these reports [*Trac et al.*, 2007; 2013].

Chinese land use and conservation policies are generally considered to be some of the most comprehensive, particularly among developing nations, however, the programs often suffer from inadequate implementation [*Bao*, 2006; *Trac et al.*, 2013]. In some cases, evidence has even been found of falsified results being reported to governmental agencies [*Trac et al.*, 2013]. Basin-scale analysis of sediment yield from rivers in SW

China do not clarify the issue, and did not find any significant correlation between sediment yield and land use or development [*Schmidt et al.*, 2011]. In spite of significant work attempting to clarify the impact of Chinese land-use history on the environment in a range of natural and social science fields, the question still remains: Has human influence on the landscape significantly degraded China's environment?

I address a portion of this question in this research, specifically: Has Chinese land use changed the pace of erosion over the past century? The half-lives and deposition periods of the isotopes used in this study, particularly $^{210}Pb_{ex}$ and $^{137}Cs$, allow for qualitative assessment of erosion occurring over the period of both widespread deforestation and conservation from the basin-scale. Therefore, where appropriate in this work, I attempt to place the erosion observed via the isotopic data in the context of recent Chinese land-use policies implemented in the study region.

## 3 Introduction to isotopic tracers of erosion

In this work, I use four different sediment associated isotopes to trace erosion. Isotope production occurs either *in situ* where the atoms are retained within the crystal structure of mineral grains ($^{10}Be_i$) or in the atmosphere, from which isotopes are delivered to Earth's surface through precipitation and dry-fall ($^{10}Be_m$, $^{210}Pb_{ex}$, and $^{137}Cs$). Atmospherically produced nuclides are often referred to as fallout radionuclides. Once fallout radionuclides are delivered to the surface of the Earth, they strongly adhere to the exterior of sediment grains and are assumed to mobilize exclusively through the

movement of sediment [*Willenbring and von Blanckenburg*, 2010; *Parsons and Foster*, 2011; *Mabit et al.*, 2014].

*In situ*-produced and fallout radionuclides have been used extensively to quantify erosion, fingerprint unique sediment sources, and investigate sediment mixing in rivers [e.g., *Brown et al.*, 1988; *Walling and Woodward*, 1992; *Brown et al.*, 1995b; *Bierman and Steig*, 1996; *Granger et al.*, 1996; *Mabit et al.*, 2008; *Yanites et al.*, 2009; *Reusser and Bierman*, 2010; *Willenbring and von Blanckenburg*, 2010]. In this study, I use the isotopes to assess sediment mixing in streams ($^{10}Be_i$ and $^{10}Be_m$), calculate long-term average erosion rates ($^{10}Be_i$), estimate the balance between atoms leaving a basin on sediment vs. atoms delivered to the basin via precipitation, called the erosion index ($^{10}Be_m$), and to qualitatively assess contemporary erosion ($^{210}Pb_{ex}$ and $^{137}Cs$).

References

Akciz, S., B. C. Burchfiel, J. L. Crowley, Y. Jiyun, and C. Liangzhong (2008), Geometry, kinematics, and regional significance of the Chong Shan shear zone, Eastern Himalayan Syntaxis, Yunnan, China, *Geosphere*, *4*(1), 292.

Bao, M. (2006), The Evolution of environmental policy and its impact in the People's Republic of China, *Conservation and Society*, *4*(1), 36-54.

Bierman, P. R., and E. Steig (1996), Estimating rates of denudation and sediment transport using cosmogenic isotope abundances in sediment, *Earth Surface Processes and Landforms*, *21*, 125-139.

Brown, E. T., R. F. Stallard, M. C. Larsen, G. M. Raisbeck, and F. Yiou (1995b), Denudation rates determined from the accumulation of *in situ*-produced $^{10}$Be in the Luquillo experimental forest, Puerto Rico, *Earth and Planetary Science Letters*, *129*, 193-202.

Brown, L., M. Pavich, R. E. Hickman, J. Klein, and R. Middleton (1988), Erosion of the eastern United States observed with $^{10}$Be, *Earth Surface Processes and Landforms*, *13*, 441-457.

Burg, J.-P., P. Davy, P. Nievergelt, F. Oberli, D. Seward, Z. Diao, and M. Meier (1997), Exhumation during crustal folding in the Namche-Barwa syntaxis, *Terra Nova*, *9*(2), 53-56.

Elvin, M. (2004), *The Retreat of the Elephants: An Environmental History of China*, Yale University Press.

Fan, H., J. Hu, and D. He (2013), Trends in precipitation over the low latitude highlands of Yunnan, China, *J. Geogr. Sci.*, *23*(6), 1107-1122.

Granger, D. E., J. W. Kirchner, and R. Finkel (1996), Spatially averaged long-term erosion rates measured from *in situ*-produced cosmogenic nuclides in alluvial sediments, *Journal of Geology*, *104*(3), 249-257.

Henck, A. C., K. W. Huntington, J. O. Stone, D. R. Montgomery, and B. Hallet (2011), Spatial controls on erosion in the Three Rivers Region, southeastern Tibet and southwestern China, *Earth and Planetary Science Letters*, *303*(1-2), 71-83.

Hooke, R. L. (1994), On the efficacy of humans as geomorphic agents, *GSA Today*, *4*(9), 217,224-225.

Hooke, R. L. M.-D., Jose F. (2012), Land transformation by humans: A review, *GSA Today*, *22*(12), 4-10.

Hyde, W. F., B. Belcher, and J. Xu (2003), *China's forests: global lessons from market reforms*, Resources for the Future and CIFOR, Washington, DC.

Mabit, L., M. Benmansour, and D. E. Walling (2008), Comparative advantages and limitations of the fallout radionuclides $^{137}Cs$, $^{210}Pb_{ex}$ and $^{7}Be$ for assessing soil erosion and sedimentation, *Journal of Environmental Radioactivity*, *99*, 1799-1807.

Mabit, L., M. Benmansour, J. Abril, D. Walling, K. Meusburger, A. Iurian, C. Bernard, S. Tarján, P. Owens, and W. Blake (2014), Fallout $^{210}Pb$ as a soil and sediment tracer in catchment sediment budget investigations: A review, *Earth-Science Reviews*, *138*, 335-351.

Matisoff, G., and P. Whiting (2012), Measuring Soil Erosion Rates Using Natural ($^{7}Be$, $^{210}Pb$) and Anthropogenic ($^{137}Cs$, $^{239,240}Pu$) Radionuclides, in *Handbook of Environmental Isotope Geochemistry*, edited by M. Baskaran, pp. 487-519, Springer Berlin Heidelberg.

Parsons, A. J., and I. D. L. Foster (2011), What can we learn about soil erosion from the use of $^{137}Cs$?, *Earth-Science Reviews*, *108*(1), 101-113.

Portenga, E. W., and P. R. Bierman (2011), Understanding Earth's eroding surface with $^{10}Be$, *GSA Today*, *21*(8), 4-10.

Reusser, L. J., and P. R. Bierman (2010), Using meteoric $^{10}Be$ to track fluvial sand through the Waipaoa River basin, New Zealand, *Geology*, *38*(1), 47-50.

Schmidt, A. H., D. R. Montgomery, K. W. Huntington, and C. Liang (2011), The question of communist land degradation: new evidence from local erosion and basin-wide sediment yield in Southwest China and Southeast Tibet, *Annals of the Association of American Geographers*, *101*(3), 477-496.

Trac, C., S. Harrell, T. Hinckley, and A. Henck (2007), Reforestation programs in Southwest China: Reported success, observed failure, and the reasons why, *J. Mt. Sci.*, *4*(4), 275-292.

Trac, C. J., A. C. H. Schmidt, S. Harrell, and T. M. Hinckley (2013), Is the Returning Farmland to Forest Program a Success? Three case studies from Sichuan, *Environmental Practice*, *15*(3), 350-366.

Trimble, S. W. (1977), The fallacy of stream equilibrium in contemporary denudation studies, *American Journal of Science*, *277*, 876-887.

Walling, D. E., and J. C. Woodward (1992), Use of radiometric fingerprints to derive information on suspended sediment sources, *Erosion and Sediment Transport Monitoring Programmes in River Basins*(210), 153-163.

Willenbring, J. K., and F. von Blanckenburg (2010), Meteoric cosmogenic Beryllium-10 adsorbed to river sediment and soil: Applications for Earth-surface dynamics, *Earth-Science Reviews*, *98*, 105-122.

Yanites, B. J., G. E. Tucker, and R. S. Anderson (2009), Numerical and analytical models of cosmogenic radionuclide dynamics in landslide‐dominated drainage basins, *Journal of Geophysical Research: Earth Surface (2003‐2012)*, *114*(F1).

# Chapter 2: Manuscript for *Journal of Geophysical Research: Earth Surface*

## Using long- and short-lived sediment-associated isotopes to track erosion and sediment movement through rivers in Yunnan, SW China

Thomas B. Neilson[a], Paul Bierman[a], Amanda H. Schmidt[b], Dylan H. Rood[c], William B. Ouimet[d], Veronica Sosa Gonzalez[e]

For submission to the *Journal of Geophysical Research: Earth Surface*

Corresponding Author: Thomas B. Neilson, tneilson@uvm.edu

[a] Department of Geology, University of Vermont, 180 Colchester Ave., Burlington, VT 05405
[b] Geology Department, Oberlin College, 403 Carnegie Building, 52 W. Lorain St., Oberlin, OH 44074
[c] Department of Earth Science and Engineering, Imperial College London, South Kensington Campus, London SW7 2AZ, UK
[d] Department of Geography and Center for Integrative Geosciences, University of Connecticut, Storrs, CT, 06269
[e] Rubenstein School of Environment and Natural Resources, University of Vermont, Burlington, VT 05405

Key Points

Combining short- and long- lived sediment-associated isotopes

Sediment mixes well in basins with significant human influence

Multiple isotopes in one sample improves understanding of erosion

Abstract

Modern Chinese land use policies are widely believed to have substantially increased erosion in western China, but extensive sediment yield data from the region shows no sign of such erosion. In order to better understand catchment-wide patterns in erosion and untangle natural and anthropogenic processes, we measured *in situ*-produced $^{10}Be$, meteoric $^{10}Be$, $^{210}Pb_{ex}$, and $^{137}Cs$ on the 250-850 μm fraction of 54 fluvial sediment samples from three tributary catchments (200-2500 $km^2$) of the Mekong River, Yunnan, China. Each study basin has over 20 years of daily sediment yield data, and includes a wide range of topography and land-use. Long-term erosion rates scale with topographic parameters in two of the three study basins. Isotopic data also show that erosion is higher in cultivated areas than un-cultivated areas. Contemporary sediment yield has not increased notably due to land-use change, however, under-representation of large stochastic events and sediment trapped by agriculture have reduced sediment yield relative to the long-term average. While each isotope potentially provides unique information regarding erosional process, *in situ* $^{10}Be$ and $^{210}Pb_{ex}$ are the most useful, and meteoric $^{10}Be$ the most challenging to utilize. Overall, the data imply changes in contemporary erosion that are consistent with national policies promoting deforestation

from 1950 – 1980's and conservation from the late 1990's to present. While interpretation is complex, measuring all four isotopes on the same sediment samples helps to fully realize the potential of *in* situ $^{10}$Be to estimate background erosion by simultaneously allowing for assessment of contemporary and human induced erosion.

# 1 Introduction

Understanding the source and volume of sediment moving across the landscape, and the role of humans in sediment generation and transport, are fundamental issues in Earth science [*NRC*, 2012]. There is a growing body of research that uses long- and short-term measures of sediment generation and/or erosion derived both from sediment-associated isotopes and from sediment yield data to disentangle the influence of natural and human processes at a range of temporal and spatial scales [*Judson*, 1968; *Trimble*, 1977; *Ritchie and McHenry*, 1990; *Walling and Woodward*, 1992; *Wallbrink and Murray*, 1993; *Walling*, 1999; *Bierman et al.*, 2001; *Hewawasam et al.*, 2003; *Bierman and Nichols*, 2004; *von Blanckenburg*, 2005; *Vanacker et al.*, 2007; *Mabit et al.*, 2008; *Willenbring and von Blanckenburg*, 2010; *Portenga and Bierman*, 2011; *Granger et al.*, 2013; *Reusser et al.*, 2015]. Most investigations rely on one or, at most, two methods (e.g., *in situ* $^{10}$Be, meteoric $^{10}$Be, $^{137}$Cs, $^{210}$Pb$_{ex}$, sediment yield data, and/or thermochronology). Only a few use isotopes with both short ($^{210}$Pb$_{ex}$, $^{137}$Cs) and long ($^{10}$Be) half-lives to quantify erosion over differing time scales or to track the source of sediment moving through river networks [*O'Farrell et al.*, 2007; *Belmont et al.*, 2014; *Stout et al.*, 2014].

This study uses *in situ* $^{10}$Be ($^{10}$Be$_i$), meteoric $^{10}$Be ($^{10}$Be$_m$), $^{137}$Cs, and $^{210}$Pb$_{ex}$ to understand better how, where, and when regolith is formed and then eroded over decades to millennia. National land-use policies in China resulted in widespread deforestation from the 1950's to the end of the century followed by recent conservation policies that were enacted in an effort to combat destructive land use [*Trac et al.*, 2007; 2013].

Extensive sediment yield data for the region, however, do not show a significant increase in sediment delivered by rivers in the region as a result of land-use change and development [*Schmidt et al.*, 2011]. By measuring the activity of each isotope in every sample, we seek to determine if the pace and spatial distribution of erosion has changed due to land-use practices in three tributary basins of the Mekong River, Yunnan, China (Figure 1). We interpret cosmogenic and radiogenic nuclide data in the context of over 20 years of daily sediment yield data at the outlet of each of the three study basins [*Henck et al.*, 2010; *Schmidt et al.*, 2011], 30-m resolution contemporary land-use data [*Chen et al.*, 2015], 56 years of 0.25° resolution mean annual rainfall records [*Yatagai et al.*, 2012], and topographic derivatives of 30-m resolution ASTER GDEM digital elevation models [*NASA LP-DAAC*, 2012].

## 2 Isotopic systems

A variety of isotopes useful for tracing surface processes have been measured in detrital sediments, including $^{10}Be_i$ [e.g., *Portenga and Bierman*, 2011], $^{10}Be_m$ [e.g., *Willenbring and von Blanckenburg*, 2010], $^{137}Cs$ [e.g., *Koiter et al.*, 2013], and $^{210}Pb_{ex}$ [e.g., *Mabit et al.*, 2014]. These isotopes accumulate in sediment either by *in situ* production within mineral grains ($^{10}Be_i$) or by fallout of atmospherically produced isotopes that strongly adsorb to the exterior of sediment grains ($^{10}Be_m$, $^{137}Cs$, $^{210}Pb_{ex}$). Each of these four isotope systems has a characteristic relationship with depth below the ground surface [*Lal and Peters*, 1967; *Walling and Woodward*, 1992; *Graly et al.*, 2010]; their differing half-lives and delivery times have the potential to record surface processes

acting over different timescales (Figure 2) [*Brown et al.*, 1995b; *Bierman and Steig*, 1996; *Granger et al.*, 1996; *Mabit et al.*, 2008; *Willenbring and von Blanckenburg*, 2010].

### *2.1* In situ *produced 10-beryllium (*$^{10}Be_i$*)*

$^{10}Be_i$ ($t_{1/2}$ = 1.39 My) [*Chmeleff et al.*, 2009], measured in detrital quartz sand, is widely used [*Portenga and Bierman*, 2011] to estimate basin-wide background erosion rates integrated over $10^3 – 10^5$ years [*Brown et al.*, 1995b; *Bierman and Steig*, 1996; *Granger et al.*, 1996]. Production of $^{10}Be_i$ in quartz occurs primarily through neutron spallation in the upper several meters of Earth's surface [*Lal and Peters*, 1967; *Lal*, 1988, 1991]. Below ~2 m of rock, neutron-induced nuclide production is negligible and production from muons dominates [*Brown et al.*, 1995a; *Heisinger et al.*, 2002a; 2002b].

$^{10}Be_i$ is used to estimate long-term rates of sediment generation and erosion in areas disturbed by human activities [*Brown et al.*, 1995b; *Bierman and Steig*, 1996; *Granger et al.*, 1996; *Brown et al.*, 1998; *Hewawasam et al.*, 2003; *Vanacker et al.*, 2007; *Reusser et al.*, 2015]. This method assumes that the depth of sediment disturbed by humans does not exceed the depth of biologically stirred soil, which in most environments is restricted to the upper half to one meter [e.g., *Pavich et al.*, 1985; *Perg et al.*, 2001; *Jungers et al.*, 2009]. If human disturbance is severe enough that sediment is sourced from below the mixed layer, the concentration of $^{10}Be_i$ overestimates the long-term average erosion rate [*Brown et al.*, 1995b; *Bierman and Steig*, 1996; *Granger et al.*, 1996; *Niemi et al.*, 2005; *Yanites et al.*, 2009].

$^{10}Be_i$-derived erosion rates are used to investigate differences between contemporary sediment yield integrated over years to decades and sediment generation rates integrated over $10^3 – 10^5$ year time-scales [*Brown et al.*, 1998; *Clapp et al.*, 2000; *Bierman et al.*, 2001; *Kirchner et al.*, 2001; *Schaller et al.*, 2001; *Hewawasam et al.*, 2003; *Matmon et al.*, 2003a; *Bierman et al.*, 2005; *Nichols et al.*, 2005b; *Vanacker et al.*, 2007; *Cyr and Granger*, 2008; *Nichols et al.*, 2014; *Reusser et al.*, 2015]. Previous studies have identified areas where $^{10}Be_i$-based erosion rates exceed modern sediment generation rates [*Bierman et al.*, 2001; *Kirchner et al.*, 2001; *Schaller et al.*, 2001], regions where contemporary sediment yield outpaces cosmogenically-determined erosion rates [*Brown et al.*, 1998; *Clapp et al.*, 2000; *Hewawasam et al.*, 2003; *Bierman et al.*, 2005; *Reusser et al.*, 2015], and regions where cosmogenic and contemporary erosion rates appear to be in balance [*Matmon et al.*, 2003a; *Nichols et al.*, 2005b; *Cyr and Granger*, 2008; *Nichols et al.*, 2014].

Long-term erosion rates that exceed modern rates are thought to reflect the absence of large, long-recurrence-interval sediment transport events in short sediment-gauging records [*Kirchner et al.*, 2001; *Schaller et al.*, 2001]. Consistent erosion rates across varying times scales are used as evidence supporting long-term landscape steady state [*Matmon et al.*, 2003a; *Cyr and Granger*, 2008] and sediment storage buffering against short-term increases in sediment yield from human influence [*Nichols et al.*, 2014]. Instances of modern sediment yield outpacing cosmogenically-determined erosion rates are usually attributed either to evacuation of stored sediment [*Clapp et al.*, 2000;

*Bierman et al.*, 2005] or human disturbance of the landscape [*Hewawasam et al.*, 2003; *Vanacker et al.*, 2007; *Reusser et al.*, 2015].

### *2.2 Fallout radionuclides ($^{10}Be_m$, $^{210}Pb_{ex}$, and $^{137}Cs$)*

Landscape-scale accumulation patterns of atmospherically delivered nuclides are determined by half-life, chemical properties, erosion and sedimentation rates and patterns, delivery rate, and delivery timing [*Quine et al.*, 1992; *Walling and Woodward*, 1992; *Barg et al.*, 1997; *He and Walling*, 1997; *Lu and Higgitt*, 2000; *Kaste et al.*, 2007; *Graly et al.*, 2010]. Delivery of fallout nuclides occurs primarily through precipitation scavenging of atmospheric aerosols to which nuclides are adhered; however, dry-fall and aeolian transport of dust derived from soils are also important [*Brown*, 1987; *Preiss et al.*, 1996; *He and Walling*, 1997; *Mabit et al.*, 2008]. Once delivered to Earth's surface at a site, fallout radionuclides sorb to regolith grains, and subsequent changes in nuclide inventory are generally assumed to be the result of regolith movement and radioactive decay [*Willenbring and von Blanckenburg*, 2010; *Parsons and Foster*, 2011; *Mabit et al.*, 2014]. In contrast to the nuclear physics and bioturbation that control the depth distribution of $^{10}Be_i$, the depth distribution and concentration of fallout isotopes in regolith, and thus sediment, is the result of a complex suite of pedogenic, chemical, and physical processes [e.g., *Willenbring and von Blanckenburg*, 2010; *Parsons and Foster*, 2011; *Mabit et al.*, 2014].

### 2.2.1 Meteoric 10-beryllium ($^{10}Be_m$)

$^{10}Be_m$ is formed through spallation of N and O in the atmosphere [*Lal and Peters*, 1962, 1967]. $^{10}Be_m$ is subsequently delivered to the Earth's surface by precipitation and dry deposition, and fallout is typically modeled as a function of precipitation and latitude, [*Graly et al.*, 2011] or through a combination of atmospheric production [*Masarik and Beer*, 1999] and climate models [*Field et al.*, 2006; *Heikkila et al.*, 2008]. In areas where significant material is introduced by the fallout of airborne dust, the total $^{10}Be_m$ delivery rate can be challenging to determine [*Monaghan et al.*, 1986; *Willenbring and von Blanckenburg*, 2010; *Graly et al.*, 2011; *Ouimet et al.*, 2015]. Once at Earth's surface, $^{10}Be_m$ adheres to the exterior of grains and is incorporated in grain coatings with soil-water partition coefficients on the order of $10^5$ to $10^6$ [*Nyffeler et al.*, 1984; *You et al.*, 1989]. Significant leaching and loss from the soil column only occur at soil pH <3.9 [*Graly et al.*, 2010], although pedogenic processes redistribute $^{10}Be_m$ [*Jungers et al.*, 2009; *Wyshnytzky et al.*, 2015]. $^{10}Be_m$ moves across the landscape in association with sediment, and its concentration and spatial distribution integrate surface processes occurring over the past $10^0 – 10^5$ years [*Pavich et al.*, 1986; *McKean et al.*, 1993; *Jungers et al.*, 2009; *Reusser and Bierman*, 2010; *West et al.*, 2013; 2014].

$^{10}Be_m$ accumulates in the top several meters of Earth's surface, and its concentration as a function of depth in soil can provide insight into dominant erosion processes [*Graly et al.*, 2010]. Younger or more quickly eroding soils typically have peak $^{10}Be_m$ concentrations in the top ~20 cm; older or more slowly eroding soils have peak concentrations at depths between 50 and 200 cm [*Graly et al.*, 2010]. The pattern of

$^{10}Be_m$ concentration with depth determines the $^{10}Be_m$ concentration of sediment eroded from different depths (e.g., sheetwash vs. landsliding). For example, sediment from a large mass movement could be traced through New Zealand's Waipaoa drainage network because it was sourced from tens of meters below the surface and had a very low $^{10}Be_m$ concentration [*Reusser and Bierman*, 2010].

### *2.2.2 Excess 210-lead ($^{210}Pb_{ex}$)*

$^{210}Pb$ ($t_{1/2}$ = 22.2 yr) is a naturally occurring isotope that is part of the $^{238}U$ decay series. $^{226}Ra$ occurs naturally in most soils and decays to the gas $^{222}Rn$. Much of the $^{222}Rn$ gas decays to $^{210}Pb$ in soil; however, some of it escapes the soil and decays to $^{210}Pb$ in the atmosphere. It is then returned to the surface as $^{210}Pb_{ex}$, also referred to as "unsupported" $^{210}Pb$, to distinguish it from supported $^{210}Pb$, the product of $^{222}Rn$ decay in soil.

$^{210}Pb_{ex}$ is useful for assessing erosion of the upper ~20 cm of soil occurring over the past ~100 years [*Bierman et al.*, 1998; *Mabit et al.*, 2008; 2014]. Undisturbed soils typically exhibit an exponential decline in $^{210}Pb_{ex}$ activity with depth; tilled soils exhibit lower relative surface activity and less dramatic decline in activity with depth because of recent mixing [*Walling and Woodward*, 1992; *Matisoff and Whiting*, 2012]. In areas of slow to moderate erosion, half-life is a primary control on the geomorphically useful timeframe of $^{210}Pb_{ex}$. In rapidly eroding areas, erosion rate controls the activity of $^{210}Pb_{ex}$ [*Mabit et al.*, 2014].

### *2.2.3 137-cesium ($^{137}Cs$)*

$^{137}Cs$ is a radionuclide released by atmospheric nuclear weapons testing and nuclear power plant accidents [*Matisoff and Whiting*, 2012; *Fan et al.*, 2014]. It was primarily deposited globally from the mid 1950's to the early 1970's [*He and Walling*, 1997]. Due to the timing of deposition, $^{137}Cs$ activity in soil and sediment shed from the landscape reflects erosion and sedimentation that occurred in the time since weapons testing took place, providing an effective means of measuring landscape change over the past ~60 years. Peak $^{137}Cs$ activities are typically several centimeters below the surface in un-tilled soil and roughly uniform throughout the disturbed layer in tilled soil; in most soils, little to no $^{137}Cs$ is present below ~20 cm depth [*Walling and Woodward*, 1992; *He and Walling*, 1997; *Kaste et al.*, 2007; *Mabit et al.*, 2008; *Matisoff and Whiting*, 2012].

### *2.2.4 Grain size dependence of fallout radionuclides*

Sediment-associated fallout nuclide concentrations depend on grain-size, preferentially adsorbing to finer particles [*Willenbring and von Blanckenburg*, 2010; *Matisoff and Whiting*, 2012]. Whether and to what degree specific surface area, mineralogy, and grain size availability affects partitioning between grains is still not well understood [*Brown et al.*, 1988; *Walling and Woodward*, 1992; *He and Walling*, 1996; *Shen et al.*, 2004; *Wittmann et al.*, 2012; *Fan et al.*, 2014]. As such, most studies investigating drainage basin erosion with $^{137}Cs$ and $^{210}Pb_{ex}$ utilize bulk samples of suspended, therefore fine grained, sediment for analysis [*Walling and Woodward*, 1992; *Mabit et al.*, 2008; *Matisoff and Whiting*, 2012; *Mabit et al.*, 2014]. Studies investigating

erosion with $^{10}Be_m$ typically select a single grain size fraction to measure [e.g., *Reusser and Bierman*, 2010], perform analysis on bulk suspended sediment [e.g., *Belmont et al.*, 2014; *Stout et al.*, 2014], or normalize for grain size dependency using the concentration of a chosen metal [e.g., *Willenbring and von Blanckenburg*, 2010].

### *2.3 Source discrimination and sediment mixing*

Characteristic short- and long-lived nuclide concentrations from specific geomorphic settings are used to identify the source of river-borne sediment [e.g., *Walling and Woodward*, 1992; *Whiting et al.*, 2001; *Clapp et al.*, 2002; *Reusser and Bierman*, 2010; *Belmont et al.*, 2014; *Smith and Blake*, 2014]. Deeply penetrating mass movements source sediment with low concentrations of $^{10}Be_i$ and $^{10}Be_m$, a characteristic that can be used to identify portions of the landscape dominated by landslides and deep gullies [*Niemi et al.*, 2005; *Reusser and Bierman*, 2010; *Savi et al.*, 2014]. Other process-specific relationships provide insight into sediment provenance. For example, different $^{10}Be_i$ concentration in sediment above and below propagating knickzones can be used to determine the relative sediment contribution of adjusted and unadjusted portions of the landscape [*Miller et al.*, 2013; *Willenbring et al.*, 2013]. Site-specific variations in $^{10}Be_i$ concentration can allow discrimination between sediment "recycled" from lowland storage and that newly generated from uplands [*Clapp et al.*, 2002; *Nichols et al.*, 2005a].

Multiple isotope systems can discriminate between sediment sources at the reach to small catchment scale, often referred to as "sediment fingerprinting" [*Walling and Woodward*, 1992; *Belmont et al.*, 2014; *Smith and Blake*, 2014; *Stout et al.*, 2014], but

this approach is rarely applied to larger basins (>100 $km^2$). Combined isotopic systems are used to determine relative sediment contribution from areas under different land use [*Collins et al.*, 1997; *Smith and Blake*, 2014], surficial and channel sources [*Walling and Woodward*, 1992], sheet and rill erosion [*Whiting et al.*, 2001], and bank, bluff, and upland erosion [*Belmont et al.*, 2014; *Stout et al.*, 2014]. In spite of the broad and successful application of sediment fingerprinting in small catchments, increasing complexity of channel-floodplain interaction can result in $^{137}Cs$ and $^{210}Pb_{ex}$ decaying over long sediment routing times, changing the isotopic character of the sediment and making isotopic sediment fingerprinting techniques less certain in large basins [*Belmont et al.*, 2014].

Temporal variation in erosion can also be resolved by combining isotopes that record erosion over different time periods [*O'Farrell et al.*, 2007; *Belmont et al.*, 2014; *Mabit et al.*, 2014; *Stout et al.*, 2014]. Comparisons of erosion rates derived from $^{210}Pb_{ex}$ and $^{137}Cs$ have shown that erosion is often relatively steady over the past ~100 years; however, recent land-use change has resulted in discrepancies between $^{137}Cs$ and $^{210}Pb_{ex}$ in some studies [*Mabit et al.*, 2014]. Few studies have combined long-term $^{10}Be_i$-derived or $^{10}Be_m$ measures of erosion with erosion estimates derived from short-lived isotopes; of those that have, observed temporal variations are attributed to human influence [*O'Farrell et al.*, 2007; *Fifield et al.*, 2010; *Stout et al.*, 2014].

$^{10}Be_i$ in fluvial sand is used to determine how well rivers mix sediment at the reach and basin scale. $^{10}Be_i$ erosion rates will not represent an average of the entire contributing area if the sediment flux from contributing sub-basins is not proportional to

the long-term rate at which sediment is shed from the landscape [*Brown et al.*, 1995b; *Bierman and Steig*, 1996; *Granger et al.*, 1996]. *Clapp et al.* [2002], *Matmon et al.* [2003b], and *Bierman et al.* [2005] assessed downstream sediment mixing using $^{10}Be_i$ in $10^0 – 10^3$ km$^2$ basins and found sediment to be well mixed. Conversely, poorly mixed sediment was identified at junctions in smaller (<1 – 30 km$^2$) basins and generally attributed to insufficient sample distance downstream of the junction, stochastic sediment supply (e.g., localized differences in precipitation or mass-wasting), and small catchment size [*Binnie et al.*, 2006; *Savi et al.*, 2014].

## 3 Context for the use of multiple isotopic systems in this study

In this paper, we use four different isotopic systems to better understand temporal changes in erosion rates of three watersheds that are tributaries to the Mekong River. We use $^{10}Be_i$ to quantify long-term erosion rates [*Brown et al.*, 1995b; *Bierman and Steig*, 1996; *Granger et al.*, 1996] and to test the efficacy of sediment mixing below stream junctions [*Binnie et al.*, 2006; *Savi et al.*, 2014]. In combination with long-term sediment yield estimates derived from $^{10}Be_i$, we use $^{10}Be_m$ to calculate erosion indices, the ratio of $^{10}Be_m$ atoms exported from a basin to the total number of atoms delivered [*Brown et al.*, 1988]. Erosion indices provide a means of comparing the flux of $^{10}Be_m$-bearing regolith among basins.

We use short-lived isotopes to understand recent rates and depths of erosion [*O'Farrell et al.*, 2007; *Fifield et al.*, 2010; *Stout et al.*, 2014]. The presence of $^{210}Pb_{ex}$ in sediment is a clear indication that sediment is primarily sourced from the uppermost

decimeters of regolith [*Walling and Woodward*, 1992; *Matisoff and Whiting*, 2012]. The presence of $^{137}$Cs indicates that sediment was sourced from the shallow regolith and that erosion, whether constant or changing over the past 50 years, has not yet removed the $^{137}$Cs-bearing portion of regolith from the sediment transport system [*Walling and Woodward*, 1992; *He and Walling*, 1997]. The absence of both isotopes indicates either high rates of contemporary surface erosion, or sediment sourced primarily from deeper erosional features (Figure 2).

Using the chemical and physical properties of each isotopic system along with data about land use, topographic derivatives, and contemporary sediment yield, we attempt to decipher the dominant short- and long-term erosional processes in each river basin in greater detail than would be possible with only one or two isotopic methods.

## 4 Field sites

We chose the Yongchun, Weiyuan, and Nankai Rivers based on the range in basin area (200 – 2500 km$^2$), relative position in the regional N-S gradient in rainfall (Figure 1c) [*Fan et al.*, 2013], and the availability of long-term records of contemporary sediment yield [*Schmidt et al.*, 2011]. We refer to the basins by the station number assigned by *Schmidt et al.* [2011]; the Yongchun River is referred to as basin 35, the Weiyuan River as basin 49, and the Nankai River as basin 11.

The entire study region was subject to wide spread deforestation during the Three Great Cuttings [*Trac et al.*, 2007]. The first two cuttings were the result of national

policies promoting development through widespread small-scale steel production (~1958 – 1960's) and increased agricultural production (1966 – 1976). The third cutting was the result of economic changes in the 1980's that allowed individuals to profit from timber harvesting [*Hyde et al.*, 2003]. Since the late 1990's, however, China has implemented several top-down conservation and restoration policies aimed at combating erosion that resulted from deforestation, and though considered extremely comprehensive, their success is widely debated [*Bao*, 2006; *Trac et al.*, 2007; *Trac et al.*, 2013].

Basin 35, situated on the southeastern margin of the Tibetan plateau, is a small (198 $km^2$) high-elevation watershed, with the lowest mean annual precipitation (MAP = 869 mm/yr) of the study sites (Figure 1b). Based on field observations of river-borne clasts and the available geologic map, the basin is underlain by Triassic granite, shale, sandstone, and limestone, Neogene sandstone, mudstone and conglomerate, and significant portions of the basin are mantled by Quaternary alluvium [*Geology of Sanjiang Ministry of Geology and Mineral Resources*, 1986]. Basin 35 bifurcates into northern and southern arms, with the steeper sub-basins in the southern arm and high-elevation, low-slope surfaces in the northern arm (Figure 3). In 2012, a large (~30 m tall) dam was completed in the southern arm of basin 35 and we observed numerous small diversion and check dams as well as out-of- and in-channel gravel mining operations. Land use in basin 35 consists primarily of forest, cultivated land, shrubland, and grassland.

The topography of basin 35 is unique among the basins we sampled, with incision along the main-stem of the Mekong overprinting the influence of normal faulting in the

basin. Basin 35 was part of a regional high-elevation, low-relief surface formed during the Oligocene to early Pliocene [*Clark et al.*, 2006; *Liu-Zeng et al.*, 2008]. A mapped NW-SE trending fault offsets formations mapped as Neogene [*Geology of Sanjiang Ministry of Geology and Mineral Resources*, 1986], with normal motion, inferred from field observations, occurring after the formation of the low-relief surface. The main- and southern-arms of the Yongchun River currently flow along the fault trace (Figure 3). Faulting increased relief in the southwestern footwall portion of basin 35, and fault scarp knickpoints migrated up the southwestern drainages forming the steep, high-elevation topography currently observed. Headward migrating knickpoints from the Mekong entered basin 35 after ~9 – 13 Ma [*Clark et al.*, 2005] and began the ongoing process of eroding the remaining low-relief landscape on the hanging wall. Knickpoint propagation was likely faster along the main- and southern-arms of the river, where incision was facilitated by the fault, resulting in less low-relief area on the hanging wall in the southern arm.

Basin 49 is the largest of the three basins (2508 $km^2$), further south in the regional rainfall gradient (MAP = 1050 mm/yr), and lower in elevation than basin 35 (Figure 1). Basin 49 consists of a main-stem river that is joined by the western arm near the outlet and the eastern arm ~20 km upstream of the outlet. Steep slopes generally prevail throughout the basin with gentle slopes limited to valley floors (Figure 3). Field observations and geologic mapping indicate that the majority of the basin is underlain by Paleogene mudstone, sandstone, and conglomerate, with Cretaceous sandstone and siltstone in the western arm and northern-most portion of the basin [*Geology of Sanjiang*

*Ministry of Geology and Mineral Resources*, 1986]. The western arm of basin 49 holds the largest of the dams in the basin (>30 m tall), which was completed in 1990. We also observed many mid-sized and smaller dams and diversions throughout the watershed, as well as numerous active-channel gravel mining operations. Land use in basin 49 is generally either forested or cultivated, with agriculture comprising ~ 22% of the total basin area, primarily in valley bottoms (Figure 3).

Basin 11 (1006 $km^2$) is the lowest elevation, furthest south, and wettest of the three basins (MAP = 1299 mm/yr; Figure 1b). Late Paleozoic-Mesozoic quartz monzonite and Proterozoic low- to mid-grade metamorphic rocks primarily underlie the basin; however, the northernmost portion of the basin is underlain by Jurassic sandstone and siltstone, and valley bottoms are covered by Quaternary fill [*Geology of Sanjiang Ministry of Geology and Mineral Resources*, 1986]. Steeper upland sub-basins and expansive low slope valley floors characterize basin 11 (Figure 3). The majority of streams are diverted near the mountain-front to irrigate sugar and rice paddies that cover the valley floor; the natural river channel in much of the northern arm is completely obscured by agriculture and irrigation structures. At least four dams were constructed in the upland sub-basins of the watershed, and mining of active channel gravel was common where the natural river channel was present. The landscape is primarily cultivated, with some forest (including rubber plantations) and grassland (Figure 3).

# 5 Methods

## *5.1 Sampling*

Using GIS and remotely sensed data, we selected 54 in-channel sample sites in three different drainage basins (Figure 4). Sampled upland sub-basins (n = 25) include the full range in mean slopes across all sub-basins over ~5 $km^2$ and include basins with end-member land uses (i.e., primarily cultivated or forested). We also collected a series of samples along major trunk-streams between the uplands and outlet in each basin (n = 29). We sampled 13 stream junctions including both incoming tributaries above the junction and the channel below the junction.

We collected samples of fluvial sediment from point bars, mid-channel islands, depositional pools, and channel beds in 2013 immediately prior to the start of the summer monsoon. Sample sites were re-evaluated in the field to account for intensive human alteration of the channel nearby, including sediment mining. If human alteration was present, we moved sampling sites to a more suitable location (usually upstream). We field sieved sediment to 250 – 850 μm, the grain-size typically used for $^{10}Be_i$ analysis. All analyses were performed on 250 – 850 μm sediment to ensure that each isotopic analysis uses the same grain-size fraction, and thus limiting the possibility for grain-size specific processes to complicate comparisons among isotopic systems.

## *5.2 Laboratory procedures*

### *5.2.1 $^{10}Be_i$*

Bulk aliquots of each sample were purified to isolate quartz using chemical etching [*Kohl and Nishiizumi*, 1992] at the University of Vermont. Prior to Be extraction, the purity of isolated quartz was tested using inductively coupled plasma – optical emission spectroscopy. Be was extracted from ~5 – 25 g of purified quartz spiked with ~250 μg of beryl carrier following established procedures [*Corbett et al.*, 2011]. Each batch included one process blank and one CRONUS N standard [*Jull et al.*, 2015]. $^{10}Be/^{9}Be$ ratios were measured by Accelerator Mass Spectrometry at the Scottish Universities Environmental Research Centre [*Xu et al.*, 2010; 2015], normalized to the NIST standard with an assumed $^{10}Be/^{9}Be$ ratio of $2.79 \times 10^{-11}$ [*Nishiizumi et al.*, 2007], and background corrected by the average process blank ratio of $2.64 \pm 0.98 \times 10^{-15}$ (n = 7, 1 SD). The single replicated field sample agreed to < 1% (Text S1). Erosion rates were calculated based on the $^{10}Be_i$ abundance in each sample, effective elevation [*Portenga and Bierman*, 2011], mean latitude, and mean longitude using the CRONUS-Earth online calculator (Accessed March 2014; main code v2.2, constants file v2.2.1, global production rate) [*Balco et al.*, 2008]. So that we could compare $^{10}Be_i$ concentrations directly, we scaled each measured concentration to its sea level and high-latitude equivalent using basin-specific production rates (muons and neutrons) provided by the CRONUS calculator to get normalized $^{10}Be_i$ concentrations [*Balco et al.*, 2008].

### 5.2.2 $^{10}Be_m$

At the University of Vermont, we dried and powdered samples, then extracted Be from ~0.5 g of sample adding ~300 – 400 μg of $^{9}$Be carrier using a modification of the fusion method presented by *Stone* [1998]. $^{10}$Be/$^{9}$Be ratios were measured and blank-corrected following the same method as used for $^{10}Be_i$, except that one process blank was run with each batch of 15 unknowns (Text S1).

$^{10}Be_m$ concentration was used to calculate the erosion index of each sampled basin [*Brown et al.*, 1988]. The erosion index, $I$, is the ratio of $^{10}Be_m$ leaving the basin on sediment to the total $^{10}Be_m$ incident upon the landscape (eq. 1).

$$I = N_s Q_s / A Q_n \quad (1)$$

Total nuclide export is the product of the measured concentration of $^{10}Be_m$ in sediment, $N_s$, and sediment yield from the basin, $Q_s$. The total $^{10}Be_m$ incident on the landscape is the product of basin area, $A$, and delivery rate, $Q_n$, estimated using the model described by *Graly et al.* [2011], which assumes delivery is a function of precipitation and latitude. In the absence of modern sediment yield at most sampling sites, we calculated long-term sediment yield for each basin using $^{10}Be_i$-derived erosion rates and basin area. At the outlet of each basin, we used the contemporary sediment yield record to calculate contemporary erosion indices, which we compare with those calculated using long-term erosion rates.

Varying $^{10}Be_m$ delivery rates ($Q_n$) in the study area, which are a function of latitude and precipitation [*Graly et al.*, 2011], complicate the direct comparison of measured $^{10}Be_m$ concentrations. Thus, we scale $^{10}Be_m$ concentrations by the ratio of the

basin delivery rate to the lowest estimated delivery rate of all the sampled basins (8.79 x $10^5$ atoms $cm^{-2}$ $yr^{-1}$) to calculate normalized $^{10}Be_m$ concentrations, thereby allowing us to compare trends in the $^{10}Be_m$ concentrations of samples.

### *5.2.3 $^{137}Cs$ and $^{210}Pb_{ex}$*

Dried samples (250 – 850 μm grain size) were placed in sealed containers for 21 days to allow radon to reach secular equilibrium with radium [*Mabit et al.*, 2014] and then counted for 24 – 96 hours using a Canberra broad energy germanium detector (Model BE3830) at Oberlin College. $^{210}Pb_{ex}$ was determined after correcting for supported $^{210}Pb$ estimates based on the activity of $^{214}Pb$ at 295.2 and 351.9 keV and $^{214}Bi$ at 609.3 and 1120.3 keV, both daughters of $^{226}Ra$. $^{137}Cs$ was determined directly. Total counts were determined by subtracting instrument background measurements for the same peak area used to quantify the nuclides. We used Angle 3.0 software to determine detector efficiency, including corrections for differences in sample geometry and composition [*Jovanovic et al.*, 2010]. Composition was determined by whole sample XRF analysis of sediment collected at the outlet of each basin at the College of Wooster's X-Ray Lab; variation in composition had an inconsequential effect on results. Any measurement of $^{137}Cs$ where the error in peak area is ≥50% at 1 SD is considered below the operational detection limit of the instrument. Our approach for determining the $^{210}Pb_{ex}$ detection limit is the same as for $^{137}Cs$; however, estimating supported $^{210}Pb$ and $^{210}Pb_{ex}$ compounds the error, resulting in higher $^{210}Pb_{ex}$ error overall, particularly in samples with a low ratio of $^{210}Pb_{ex}$ to supported $^{210}Pb$ [*Mabit et al.*, 2008].

The affinity of $^{10}Be_m$, $^{210}Pb_{ex}$, and $^{137}Cs$ for finer grained sediment means that the activity we measure on 250 – 850 μm sized sediment is likely an under-estimate of total activity in sediment leaving the watershed [*Brown et al.*, 1988; *He and Walling*, 1996; *Matisoff and Whiting*, 2012; *Wittmann et al.*, 2012]. Thus, samples that fall below the detection limit of our methods indicate only the absence of detectable nuclides in the sand fraction.

### *5.3 Digital data*

We use 30 m resolution digital elevation models generated by NASA and METI's ASTER GDEM program [*NASA LP-DAAC*, 2012] as the basis for calculating total basin relief, slope, and normalized channel steepness ($k_{sn}$). We use precipitation data provided by the APHRODITE program, a collaboration between the Research Institute for Humanity and Nature Japan and the Meteorological Research Institute of Japan Meteorological Agency. We use version APHRO_MA_V1101, which consists of daily 0.25° gridded precipitation data from 1951 to 2007 [*Yatagai et al.*, 2012]. Although it does not have the highest spatial resolution, APRHODITE provides the most accurate rainfall estimates of available datasets for this region [*Andermann et al.*, 2011]. Land-use data is from the GLC30 land cover dataset and represents 30 m resolution land cover from 2010 derived from Landsat TM, ETM+, and Chinese HJ-1 multispectral satellite images and a suite of auxiliary data sources [*Chen et al.*, 2015].

We calculate channel steepness using longitudinal river channel profiles derived from the DEM. The channel slope (S) and drainage area (A) of a fluvial channel are typically related through the power-law [*Flint*, 1974] (eq. 2):

$$S = k_s A^{-\theta} \tag{2}$$

where $k_s$ is the steepness index and θ is concavity. Channel steepness index, $k_s$, is highly sensitive to variation in θ, a complication we correct for by using a reference concavity for all basins of θ = 0.45, allowing us to derive normalized channel steepness ($k_{sn}$) in place of $k_s$ [*Wobus et al.*, 2006]. We average $k_{sn}$ in all channel segments (1 km long) where A > 1 km$^2$, and present basin-wide mean and median $k_{sn}$.

### *5.4 Sediment mixing*

We assess sediment mixing at 13 stream junctions in basins 35 (n = 5), 49 (n = 6), and 11 (n = 2) by measuring each isotope in sediment from the contributing streams above the junction as well as in sediment collected 100 – 1650 m downstream of the junction. For each isotope, the upstream concentrations are used to model the concentration downstream of the junction, $\overline{N}$, using the area weighted average (eq. 3):

$$\overline{N} = \frac{\sum N_j E_j A_j}{\sum E_j A_j} \tag{3}$$

where $N_j$ is the nuclide concentration of upstream sample $j$, $E_j$ is the $^{10}Be_i$–derived erosion rate, and $A_j$ is the area [*Granger et al.*, 1996]. The modeled concentration is then compared to the concentration measured downstream of the junction; if the modeled

concentration falls within error (2 SD) of the measured concentration, we consider the sediment below the junction to be adequately mixed.

### *5.5 Contemporary sediment yield*

We use previously reported contemporary sediment yield values [*Henck et al.*, 2010; *Schmidt et al.*, 2011] (Table 1), and compare them to long-term sediment yield results from $^{10}Be_i$ erosion rates. To convert from rate of landscape lowering to sediment yield we assume a rock density of 2.7 g/cm$^3$. The most recent contemporary sediment yield measurements date from 1987, prior to the construction of the majority of the large dams in the study area [*Magee*, 2006].

## 6 Results

### *6.1 $^{10}Be_i$*

We measured a wide range of $^{10}Be_i$ concentrations in basin sediment. Normalized to sea level and high latitude by considering basin hypsometry [*Portenga and Bierman*, 2011], $^{10}Be_i$ concentration ranges from 1.66 – 26.8 x $10^4$ atoms/g, and the distribution has significant positive skew (Figure 5a). Basin 49 has the lowest normalized $^{10}Be_i$ concentrations (mean = 3.55 ± 1.23 x $10^4$ atoms/g, all errors given as 1 SD except where otherwise noted), followed by basin 11 (mean = 8.63 ± 3.16 x $10^4$ atoms/g). Basin 35 has the greatest range of normalized $^{10}Be_i$ concentrations, over an order of magnitude, and a

significantly higher mean normalized concentration (mean = 10.5 ± 8.31 x $10^4$ atoms/g) than the basins 11 and 49 (Figures 5a; S1).

Within basin 35, the highest concentrations of $^{10}Be_i$ are found in sub-basins that primarily drain high-elevation, low slope surfaces (Figures 3 and 6) found in the northern and eastern portions of the basin. The lowest concentrations are found in sub-basins in the southern arm of the basin. Basin 49 has generally low concentrations throughout the main-stem and eastern arm of the basin, and higher concentrations in the western arm and its sub-basins (Figure 6). Basin 11 is characterized by relatively uniform concentrations in sub-basins draining valley floors and the northern upland sub-basins, with notably lower concentrations in upland sub-basins in the southern arm (Figure 6).

### *6.2 $^{10}Be_m$*

$^{10}Be_m$ concentrations, normalized for delivery rate, span two orders of magnitude, from 0.56 – 64.6 x $10^7$ atoms/g, and have significant positive skew (Figure 5b). Similar to the normalized $^{10}Be_i$ results, basin 49 has the lowest average normalized $^{10}Be_m$ concentration, followed by basin 11 (means of 1.12 ± 0.43 and 2.65 ± 1.53 x $10^7$ atoms/g respectively, 1 SD; Figure 5b). Basin 35 not only has a higher mean concentration than basins 11 and 49 (mean = 14.1 ± 16.0 x $10^7$ atoms/g), but a broader range of concentrations as well (Figure 5b).

Within basin 35, $^{10}Be_m$ concentration is generally higher in the northern high-elevation, low slope basins than in the southern arm; however, sample CH-010 in the southern arm has an extremely high $^{10}Be_m$ concentration (over 3 fold higher than the

basin mean). In basin 49, samples along the main-stem and at the confluence of the main-stem and western arm are generally low in concentration, while upland basins and the eastern arm exhibit higher concentrations of $^{10}Be_m$ (Figure 6). Basin 11 shows uniform, relatively high $^{10}Be_m$ concentrations in samples draining the valley floors, while most upland basins have somewhat lower concentrations (Figure 6).

### *6.3 $^{137}Cs$ and $^{210}Pb_{ex}$*

$^{137}Cs$ was only detected in three samples, CH-013, -016, and -017, all of which are from basin 35 and drain the high-elevation, low-slope surface (Figure 6). All other samples contained no measureable $^{137}Cs$ activity. $^{210}Pb_{ex}$ was detected in 40 of the 54 samples analyzed. Activities above the detection limit ranged from 2.33 – 15.6 Bq/kg (Figure 5c). Basins 35 and 49 have a similar range of $^{210}Pb_{ex}$ activity and number of samples in which $^{210}Pb_{ex}$ is not detectable; basin 11 has fewer samples where $^{210}Pb_{ex}$ is below detection and a higher mean activity than basins 35 and 49 (Figure 5c).

Measured $^{210}Pb_{ex}$ activity in basin 35 is highest in the lowest slope sub-basin of the northern arm (CH-013), and decreases downstream until the junction with the southern arm. No samples in the southern arm contain measureable $^{210}Pb_{ex}$ except for CH-011 and -009 (Figure 6). Sediment in basin 49 has generally low or un-detectable $^{210}Pb_{ex}$ activity along the upper main-stem, and activity is higher in most of the upland sub-basins in the eastern and western arms and near the outlet on the main-stem than elsewhere in the watershed (Figure 6). $^{210}Pb_{ex}$ activity is lower in upland sub-basins of the southern arm of basin 11 than the valley floor; however, $^{210}Pb_{ex}$ activities in the upland

sub-basins of the northern arm do not vary systematically (Figure 6). The outlet of basin 11 does not have measureable $^{210}Pb_{ex}$.

### *6.4 Relationship between nuclides*

A significant positive correlation exists between the concentration of normalized $^{10}Be_i$ and normalized $^{10}Be_m$; however, neither $^{10}Be_m$ nor $^{10}Be_i$ correlate well with $^{210}Pb_{ex}$ activity (Figure 7). A linear bivariate regression indicates 69% of the variation in normalized $^{10}Be_m$ is explained by the concentration of normalized $^{10}Be_i$ ($p < 0.0001$), after excluding an anomalously high $^{10}Be_m$ value. Bivariate plots of normalized $^{10}Be_i$ and $^{10}Be_m$ with $^{210}Pb_{ex}$ do not show any significant patterns, regardless of the inclusion of samples below the detection limit.

### *6.5 Sediment mixing*

Using $^{10}Be_i$, we find that sediment is well mixed at 5 of 13 junctions, and is close (within 6% at 2 SD) at 3 other junctions (Figure 8). All of the junctions measured in basin 49 mix well, while only one junction in each of basins 35 and 11 are well mixed. Sediment mixing considering $^{10}Be_m$ displays similar trends to $^{10}Be_i$, though with differing magnitudes (Figure 8). Four junctions mix adequately using $^{10}Be_m$, and one junction is within 3% of mixing adequately at 2 SD. Of the 5 junctions that mix well using $^{10}Be_m$, 4 of those are junctions that also mix well using $^{10}Be_i$. Large uncertainties and the absence of measureable $^{210}Pb_{ex}$ in some mixing samples limit the utility of $^{210}Pb_{ex}$ as a tracer of sediment mixing (Figure S2).

# 7 Discussion and conclusions

We interpret and discuss data in a step-wise fashion. First, we show that sampling location is the most important factor in how well sediment mixes at junctions. Then, using available isotopic, sediment yield, topographic, and climatic metrics, we determine that landscape transience, hillslope and channel steepness, and extent of agriculture employed control erosion in the study basins. Finally, we conclude by considering erosion in the context of Chinese land-use policy and the benefits and limitations of measuring four different isotopic systems in the same samples.

## *7.1 Sediment mixing*

Considering each of the three basins as a whole, sediment in the study area appears well mixed (Figure 9). In each of the three basins, the concentration of $^{10}Be_i$ converges on the mean basin concentration as sub-basin size increases, indicating that sediment mixing is sufficient for estimating $^{10}Be_i$ erosion rates [*Matmon et al.*, 2003a; *Bierman et al.*, 2005; *Wittmann et al.*, 2007]. When mixing is considered at stream junctions, however, not all junctions mix well (Figure 8).

We consider three primary controls on the efficacy of sediment mixing below stream junctions: stochastic events, human influence, and sample site location. Because no evidence of significant landslides in the field was observed, and because precipitation is primarily delivered by monsoons [*Henck et al.*, 2010] that uniformly affect all field

sites, we consider stochastic events [e.g., *Binnie et al.*, 2006; *Godard et al.*, 2012; *Savi et al.*, 2014] an unlikely explanation of poor mixing in our field area.

Anthropogenic activity can take the form of either land use or channel alterations. Because no robust relationship between sediment mixing efficacy at junctions and land-use metrics is found (Figure S3), it appears that land use has little influence on mixing. In contrast, a large dam directly above a tributary junction (Junction ID 35.1) reduced sediment supplied by that tributary to sample site CH-021 from ~80% to ~20% of the total flux (Figures 8; 10). Thus, we disregard samples collected below this junction (CH-001, -023) in further interpretation of erosion rates and erosion indices.

The best explanation for incomplete sediment mixing below tributary junctions appears to be sample location (Figure 10). We find that the greater the difference in basin area between the downstream sample site and the total area of upstream samples (hereafter termed residual area), the greater the disagreement between modeled and measured $^{10}Be_i$ concentrations. Residual area accounts for sediment mixing with distance below the junction [*Binnie et al.*, 2006; *Savi et al.*, 2014] while also quantifying the area from which sediment not included in the upstream samples can be sourced.

There is no clear explanation for why $^{10}Be_i$ and $^{10}Be_m$ mix differently (Figure 8); however, difference in sediment grain stability is one possibility. $^{10}Be_i$ is measured in quartz sand, an abundant and stable component of most river sediment. $^{10}Be_m$ (and other fallout radionuclides) is measured on all grains in the 250 – 850 μm grain size fraction. Many of the samples we collected contain aggregate grains, which likely contain proportionately more of the total $^{10}Be_m$ than single grains [*Wittmann et al.*, 2012], and are

less stable than quartz sand. Disaggregation of sediment grains over short distances (i.e. between upstream and downstream samples) [*Dyer and Olley*, 1999] would cause non-conservative behavior of $^{10}Be_m$ and other fallout radionuclides, resulting in less accurate mixing models.

Furthermore, mixing results for $^{210}Pb_{ex}$ are hindered by the timescale over which we are measuring sediment fluxes (Figure S2). Mixing analyses rely on sediment flux information, which in our case is taken from $^{10}Be_i$ data. However, the short timescale over which $^{210}Pb_{ex}$ integrates likely requires sediment flux data over the same period of time.

### *7.2 Interpreted erosion rates and indices*

Across the study basins, $^{10}Be_i$-derived erosion rates range from 12 – 209 mm/kyr with an area-weighted mean of 117 ± 49 mm/kyr and median of 74 mm/kyr. Compared to the highly skewed global dataset, these ranges fall between the mean of 218 mm/kyr and median of 54 mm/kyr [*Portenga and Bierman*, 2011] and below the mean and median erosion rates reported for the mainstem Mekong between ~25 – 30° N (152 and 131 mm/kyr, respectively, as calculated using CRONUS) [*Henck et al.*, 2011].

In basin 35, erosion rates vary from 12 – 209 mm/kyr, with an area-weighted mean of 51 ± 57 mm/kyr and median of 38 mm/kyr. Erosion rates in basin 49 are generally higher, from 55 – 193 mm/kyr with an area-weighted mean of 128 ± 34 mm/kyr and similar median value (122 mm/kyr). Basin 11 has the lowest rates of erosion, 21 – 83

mm/kyr, with an area-weighted mean of 50 ± 15 mm/kyr and median of 48 mm/kyr (Figure 11).

Erosion indices, the ratio of the long-term average $^{10}Be_m$ exported from a basin to the estimated flux of $^{10}Be_m$ into the basin (eq. 1), range from 0.09 – 7.55 over the three basins, however 7.55 represents an anomalously high value (Figure 11). Basin 35 has the highest erosion indices, from 0.68 – 7.55 with a mean of 1.65 ± 1.80 and median of 1.05. Basins 49 and 11 differ from basin 35 and have similar ranges and central tendencies, with means of 0.39 ± 0.14 and 0.39 ± 0.23 and medians of 0.37 and 0.35, respectively (Figure 11).

The low erosion indices for basins 49 and 11 suggest that over the timescale of the $^{10}Be_i$-derived erosion rates, $^{10}Be_m$ is accumulating on these landscapes, likely through sediment storage or soil formation. In contrast, on average, basin 35 is exporting more $^{10}Be_m$ than is entering the system, possibly as a result of the tectonic activity and subsequent acceleration of erosion due to knickpoint propagation and/or mining of stored sediment in the watershed.

### *7.3 Discussion of the dominant erosional processes in basins 35, 11, and 49*

#### *7.3.1 Basin 35*

In basin 35, landscape evolution is the primary control of $^{10}Be_i$ erosion rates, $^{10}Be_m$ concentrations, erosion indices, and short-lived isotope activities. Faulting and baselevel fall from Mekong River incision created a transient landscape with streams draining three different sub-landscapes: high-elevation low-relief, actively-adjusting, and

the footwall of the fault (Figure 12a). Mixing of sediment from the low-erosion rate, high-elevation low-slope landscape with sediment from the more rapidly eroding, actively-adjusting and footwall landscapes has resulted in erosion rates that scale non-linearly with elevation, a proxy for proportion of low-slope area (Figure 12b). Basins with mean elevations >3000 m have lower erosion rates, 12 – 38 mm/kyr, than basins draining proportionally less relict landscape (mean elevations <3000 m), 50 – 209 mm/kyr, confirmed by a Wilcoxon rank-sum test ($p = 0.003$). Similar results have been found using $^{10}Be_i$ elsewhere in landscapes adjusting to baselevel fall [*Willenbring et al.*, 2013], and in measured $^{10}Be_i$ erosion rates above and below knickpoints [*Miller et al.*, 2013].

In contrast to other studies comparing $k_{sn}$ and erosion rate [*Ouimet et al.*, 2009; *DiBiase et al.*, 2010; *Vanacker et al.*, 2015], we observe a non-linear decrease in erosion rates as mean basin $k_{sn}$ increases (Figure 12c). However, as found in other studies [e.g., *Granger et al.*, 1996; *Montgomery and Brandon*, 2002; *Binnie et al.*, 2007; *Ouimet et al.*, 2009; *DiBiase et al.*, 2010; *Vanacker et al.*, 2015], erosion rates increase non-linearly with increasing mean basin slope (Figure 12c). This implies that erosion rates lag behind channel steepening and only increase after channel incision has lowered hillslope baselevel and steepened slopes.

Normalized $^{10}Be_m$ concentrations are highest in low-erosion-rate basins primarily draining the low relief area, and lowest in high-erosion-rate basins draining the footwall (Figure 12d). Sample CH-010, which has an anomalously high $^{10}Be_m$ concentration, is a notable exception. With erosion indices, we again observe higher indices in steeper sub-

basins as well as non-linear scaling with slope, similar to erosion rate; however, the trend is not as well defined (Figure 12e). This may be the result of a slightly faster response of erosion index to steepening slopes than erosion rate due to higher $^{10}Be_m$ concentrations in near-surface regolith. The mean erosion index of 1.65 ± 1.80 for basin 35 is higher than those observed in basins 49 and 11, and indicates that basin 35 is exporting more $^{10}Be_m$ than is delivered [*Brown et al.*, 1988]. This is most likely due to the ongoing erosion, through knickpoint propagation, of the more stable low relief surface that contains a large inventory of $^{10}Be_m$.

The short-lived nuclides, $^{210}Pb_{ex}$ and $^{137}Cs$, have concentrations that reflect long-term erosion rates. We measured little $^{210}Pb_{ex}$ in the rapidly eroding southern arm; in contrast all samples in the northern arm contain measureable $^{210}Pb_{ex}$ (Figure 6). Likewise, the three samples draining primarily low-relief landscape each contain measureable $^{137}Cs$. This implies that not only have these low relief surfaces remained stable over the integration time of $^{10}Be_i$, but they have remained stable over the past 50 – 100 years as well.

While broad patterns in $^{10}Be_m$ concentration and short-lived isotope activity are explained by long-term erosion, these isotopes exhibit variability that is not explained by long-term processes driving landscape evolution. Examples include the anomalously high $^{10}Be_m$ concentration of CH-010, and the presence of $^{210}Pb_{ex}$ in the most rapidly eroding basin (CH-011) whereas it is absent in some basins eroding at more modest rates (Figures 6; 11). It is unlikely that land use is the primary driver of unexplained short-lived variability because only ~15% of basin 35 is cultivated land (Figure 3). More likely,

stochastic erosion of the actively adjusting landscape has elevated long-term sediment yield to twice the contemporary sediment yield [e.g., *Kirchner et al.*, 2001], which is also reflected in the contemporary erosion index and suggests that modern $^{10}Be_m$ export does not exceed the rate of deposition (Table 1). Comparison of modern sediment export to "background" export is complicated by the large dam at the junction of the north and south arms, which has likely caused an underestimate of the long-term sediment yield derived from $^{10}Be_i$-erosion rates. This suggests that the recurrence interval and/or magnitude of stochastic events are greater than the data imply.

### *7.3.2 Basin 49*

In basin 49, there is a strong signal of human impact. Cultivation (23% of total basin area) appears to be altering erosion rates and sediment sources on both short and long timescales and introducing low-nuclide-activity sediment into stream channels. We detected no $^{137}Cs$ and little $^{210}Pb_{ex}$ in fluvial sediment from basin 49, suggesting that erosion was rapid over the past 50 – 100 years, most likely due to deforestation for agriculture. This inference is supported by a modest negative relationship between cultivated area and samples with detectable $^{210}Pb_{ex}$ ($R^2 = 0.36$, $p = 0.007$; Figure 13). The weak positive relationship of cultivated area to erosion index and erosion rate ($R^2 = 0.27$ and 0.21, $p = 0.01$ and 0.02, respectively) suggests that erosion is deep enough in some cultivated areas that regolith from ≥ ~0.5 m below the surface is now being supplied to channels [*Pavich et al.*; *Brown et al.*, 1995b; *Bierman and Steig*, 1996; *Granger et al.*, 1996; *Perg et al.*, 2001; *Jungers et al.*, 2009].

Considered together, relationships between cultivation and short- and long-term measures of erosion imply that much of the sediment carried by rivers is sourced from cultivated portions of the landscape, which are eroding more quickly than uncultivated areas. However, contemporary sediment yield and erosion index agree well with long-term sediment yield (Table 1), suggesting either that rates of sediment transport have not increased and the isotopic signature we observe is due only to a change in sediment source, or that much of the sediment shed from agricultural fields is stored and/or was exported after the gauging period, ending in 1987 [*Walling*, 1983; *Parsons and Foster*, 2011; *Nichols et al.*, 2014].

In basin 49, no single topographic or climate metric (i.e., mean slope, mean $k_{sn}$, median $k_{sn,}$ basin relief, MAP) is well correlated with erosion rate, erosion index, or $^{10}Be_m$ concentration. Instead, we observe modest and statistically significant relationships ($R^2$ = 0.18 – 0.55, $p < 0.05$) between each isotopic indicator of long-term erosion and the topographic and climate metrics considered (Figure 13); combining parameters does not improve regressions. Bivariate relationships may be altered by the recent introduction of agriculturally derived sediments to the channel network.

### *7.3.3 Basin 11*

Basin 11 is heavily cultivated (48% of land use) and the original river channel is mostly obscured by these land-use changes; specifically, many terraces that are flooded to grow rice cover the floor of the basin. Upland hillslopes in basin 11 are impacted by land uses shown to result in elevated surficial erosion [*Sidle et al.*, 2006], including forest

conversion to agriculture, pasture and shrubland, and tea and rubber plantations (Figure 14). Agricultural terraces cause sediment deposition on the tread, while sediment is exported from the terrace by eroding walls [*Foster and Highfill*, 1983; *Inbar and Llerena*, 2000]. The few remaining valley floor channels are incised well below the elevation of surrounding terraces (Figure 14c). Contemporary sediment yield is 50% lower than the long-term mean (Table 1), strongly suggesting terraces are a net sediment sink in basin 11, as is observed with mill-ponds in the eastern US [*Walter and Merritts*, 2008].

The results of $^{10}Be_i$ analyses likely reflect this human impact on the landscape. In contrast to basins 35 and 49, in basin 11, few topographic or climate metrics are correlated to isotopic measures of erosion. Erosion rate does have a modest negative relationship with MAP ($R^2 = 0.43$, $p = 0.008$), while both erosion index and $^{10}Be_m$ concentration have a weak positive relationship with basin relief ($R^2 = 0.33$, $p = 0.025$ for both; Figure S3). We do not observe any difference in topographic and precipitation relationships with long-term erosion when upland samples are considered separately from valley floor samples. The contemporary erosion index for basin 11 is significantly lower than the long-term erosion index, indicating current $^{10}Be_m$ export is below the long-term average (Table 1). Overall, long-term erosion in basin 11 is lower than in basins 35 and 49 (area-weighted mean = 50 mm/kyr), and is consistent with its relatively lower slopes [*Portenga and Bierman*, 2011].

The distribution of short-lived nuclides in basin 11 reflects human impacts in both the uplands and lowlands. Since the end of $^{137}Cs$ deposition, land-use driven surficial erosion likely reduced the activity of $^{137}Cs$ (and $^{210}Pb_{ex}$) in hillslope soils (as we observed

in basin 49). When sediment shed from disturbed upland slopes is deposited on a terrace, it contains little to no $^{137}Cs$ or $^{210}Pb_{ex}$. However, fluvial sediment sampled in basin 11 has high $^{210}Pb_{ex}$ activity (Figure 5) and no measureable $^{137}Cs$. To explain this, we suggest a conceptual model that describes the transport path of sediment through the basin: sediment shed from hillslopes is deposited on a terrace tread via river diversion, where it is stored until the terrace wall fails and the surficial sediment from the tread of the terrace is used to repair the wall. Sediment continues to move downslope through the terrace network in this fashion, with $^{210}Pb_{ex}$ accumulating as long as grains are in the upper few cm of soil. When sediment is finally returned to the river channel, it contains significantly more $^{210}Pb_{ex}$ accumulated during transport through the terrace network. Higher concentrations of $^{10}Be_m$ and $^{210}Pb_{ex}$ further downstream (with the dredged outlet area as an exception) are consistent with this interpretation (Figure 15). This interpretation treats agricultural terraces similarly to a large floodplain where proportionally little sediment is exported from the basin directly without storage [*Lauer and Willenbring*, 2010; *Belmont et al.*, 2014]. The result is a net sediment sink that captures coarse and fine grains equally and periodically exports sediment enriched in fallout radionuclides from the upper few cm of the terrace.

### *7.4 Implications and conclusions*

Substantial work has been done using a variety of isotopes measured in fluvial sediment in order to deduce long-term erosion rates resulting from natural processes [e.g., *Bierman and Nichols*, 2004], contemporary erosion from human disturbance [e.g.,

*Matisoff and Whiting*, 2012], and to isolate contemporary sources of sediment [e.g., *Belmont et al.*, 2014]. Each approach captures a critical component of the global transition from natural to human-dominated landscapes [*Hooke*, 2012]. By combining the ability of $^{210}Pb_{ex}$ and $^{137}Cs$ to detect short-term and human induced erosion with the ability to assess long-term natural erosion from $^{10}Be_i$ and $^{10}Be_m$, we increase the temporal resolution of erosion to include timescales that are often considered by separate studies. While the potential power of each isotope is significant, it is not realized in all situations, resulting in complex interpretations but with broader applicability in less well-constrained study areas than a single isotope system.

In this study, two isotopes provide the majority of the interpretive power for comparing long-term vs. short-term behavior: $^{10}Be_i$ and $^{210}Pb_{ex}$. $^{10}Be_i$ provides long-term erosion rates that are a critical reference for contextualizing contemporary changes [*Hewawasam et al.*, 2003; *Reusser et al.*, 2015], while $^{210}Pb_{ex}$ is most useful for assessing contemporary erosion due to its relative ubiquity in our samples compared to $^{137}Cs$. The absence of $^{137}Cs$ still provides meaningful information regarding contemporary erosion, however, and is of particular utility due to its well-constrained deposition time, which can provide insight into short-term changes in erosion when combined with $^{210}Pb_{ex}$ [*Mabit et al.*, 2014]. Overall, $^{10}Be_m$ provided the least critical information for interpreting erosion. $^{10}Be_m$, and the erosion indices calculated from it, clearly relate to topographic, climate, and land-use factors dominating erosion in the lower Chinese Mekong River basin; however, the link between $^{10}Be_m$ and erosion rate/process is more complex than with $^{10}Be_i$, making its interpretation less straightforward. Without a better understanding of the

relationship between $^{10}Be_m$ concentration in stream sediment and erosion rate and/or process [cf. *von Blanckenburg et al.*, 2012] similar future applications of multiple isotopes in detrital sediment may not see a significant benefit in including $^{10}Be_m$.

Considering all the data and what we know about the four different isotopic systems together, we propose a scenario consistent with our data and what is known about Chinese land-use policy over the past century. The absence of measurable $^{137}Cs$ in almost all of our samples suggests rapid agricultural erosion over the past 60 years, sufficient to remove up to 20 cm of soil (the average penetration depth of $^{137}Cs$), but not deep enough to alter the concentration of $^{10}Be_i$ in all but the most extreme cases. In contrast, the presence of $^{210}Pb_{ex}$ in many samples that have no detectable $^{137}Cs$ suggests that erosion slowed enough, after the peak of $^{137}Cs$ deposition in the 1950s and 1960s, to allow $^{210}Pb_{ex}$ accumulation. This peak in erosion corresponds well with national programs (the Three Great Cuttings) that promoted extensive forest clearance in China during the 1950s through the 1980s [*Schmidt et al.*, 2011]. Reduced erosion rates since that time corresponds with national programs promoting reforestation and restricting agriculture on steep slopes [*Trac et al.*, 2007; *Urgenson et al.*, 2010; *Trac et al.*, 2013]. It appears that national land-use policies play an important role in managing shallow (<20 cm) surficial erosion in China [*Yang et al.*, 2002] and that the effect of these policies can be detected by measuring a variety of isotopes in detrital sediments.

Erosion need not be and is likely not spatially uniform. In landscapes altered by humans, contemporary erosion is generally focused in agricultural areas [*Sidle et al.*, 2006; *Wilkinson and McElroy*, 2007; *Hooke*, 2012]. Focused erosion to depths of a few

tens of cm provides sediment with only low activities of short-lived nuclides. Such shallow erosion minimally effects $^{10}Be_i$ concentration because soils are usually stirred (and the $^{10}Be_i$ concentration is homogeneous) far deeper than the penetration depth of short-lived nuclides (Figure 2) [*Jungers et al.*, 2009]. Thus, measurement of multiple nuclides in detrital sediments can both fully realize the potential of $^{10}Be_i$ to provide long-term, background erosion rates and use short-lived nuclides to interpret changes in erosion over human timescales and in response to changing land-use policy.

## 8 Acknowledgements

The data presented in figures 3, 4, 5, 6, 7, 9, 11, 12, 13, and 15 can be found in table S2 in the supporting information. The data presented in figures 8 and 10 can be found in table S4 in the supporting information. Additional information on isotopic extraction and measurement methods is also available in text S1.

This research was supported by NSF awards EAR-1114166 (to Schmidt), EAR-1114159 (to Bierman), and EAR-1114436 (to Rood). We thank the staff of the AMS Laboratory at the Scottish Universities Environmental Research Centre (SUERC) for $^{10}Be$ measurements.

References

Andermann, C., S. Bonnet, and R. Gloaguen (2011), Evaluation of precipitation data sets along the Himalayan front, *Geochemistry, Geophysics, Geosystems: G3*, *12*(7).

Balco, G., J. O. Stone, N. A. Lifton, and T. J. Dunai (2008), A complete and easily accessible means of calculating surface exposure ages or erosion rates from $^{10}$Be and $^{26}$Al measurements, *Quaternary Geochronology*, *3*, 174-195.

Bao, M. (2006), The Evolution of environmental policy and its impact in the People's Republic of China, *Conservation and Society*, *4*(1), 36-54.

Barg, E., D. Lal, M. J. Pavich, M. W. Caffee, and J. R. Southon (1997), Beryllium geochemistry in soils: Evaluation of $^{10}$Be/ $^{9}$Be ratios in authigenic minerals as a basis for age models, *Chemical Geology*, *140*(3-4), 237-258.

Belmont, P., J. Willenbring, S. Schottler, J. Marquard, K. Kumarasamy, and J. Hemmis (2014), Toward generalizable sediment fingerprinting with tracers that are conservative and nonconservative over sediment routing timescales, *J Soils Sediments*, *14*(8), 1479-1492.

Bierman, P. R., and E. Steig (1996), Estimating rates of denudation and sediment transport using cosmogenic isotope abundances in sediment, *Earth Surface Processes and Landforms*, *21*, 125-139.

Bierman, P. R., A. Albrecht, M. Bothner, E. Brown, T. Bullen, L. Gray, and L. Turpin (1998), Weathering, erosion and sedimentation, in *Isotope Tracers in Catchment Hydrology*, edited by C. Kendall and J. J. McDonnell, pp. 647-678, Elsevier.

Bierman, P. R., E. M. Clapp, K. K. Nichols, A. R. Gillespie, and M. Caffee (2001), Using cosmogenic nuclide measurements in sediments to understand background rates of erosion and sediment transport, in *Landscape Erosion and Evolution Modeling*, edited by R. S. Harmon and W. M. Doe, pp. 89-116, Kluwer, New York.

Bierman, P. R., and K. K. Nichols (2004), Rock to sediment - Slope to sea with $^{10}$Be - Rates of landscape change, *Annual review of Earth and Planetary Sciences*, *32*, 215-255.

Bierman, P. R., J. M. Reuter, M. Pavich, A. C. Gellis, M. W. Caffee, and J. Larsen (2005), Using cosmogenic nuclides to contrast rates of erosion and sediment yield in a semi-arid, arroyo-dominated landscape, Rio Puerco Basin, New Mexico, *Earth Surface Processes and Landforms*, *30*(8), 935-953.

Binnie, S. A., W. M. Phillips, M. A. Summerfield, and L. K. Fifield (2006), Sediment mixing and basin-wide cosmogenic nuclide analysis in rapidly eroding mountainous environments, *Quaternary Geochronology 1*, 4-14.

Binnie, S. A., W. M. Phillips, M. A. Summerfield, and L. K. Fifield (2007), Tectonic uplift, threshold hillslopes, and denudation rates in a developing mountain range, *Geology*, *35*(8), 743.

Brown, E. T., D. L. Bourles, F. Colin, G. M. Raisbeck, F. Yiou, and S. Desgarceaux (1995a), Evidence for muon-induced production of $^{10}$Be in near surface rocks from the Congo, *Geophysical Research Letters*, *22*(6), 703-706.

Brown, E. T., R. F. Stallard, M. C. Larsen, G. M. Raisbeck, and F. Yiou (1995b), Denudation rates determined from the accumulation of *in situ*-produced $^{10}$Be in the Luquillo experimental forest, Puerto Rico, *Earth and Planetary Science Letters*, *129*, 193-202.

Brown, E. T., R. F. Stallard, M. C. Larsen, D. L. Bourles, G. M. Raisbeck, and F. Yiou (1998), Determination of predevelopment denudation rates of an agricultural watershed (Cayaguas River, Puerto Rico) using *in-situ*-produced $^{10}$Be in river-borne quartz, *Earth and Planetary Science Letters*, *160*(3-4), 723-728.

Brown, L. (1987), $^{10}$Be: Recent applications in Earth sciences, *Philosophical Transactions of the Royal Society of London*, *A 323*, 75-86.

Brown, L., M. Pavich, R. E. Hickman, J. Klein, and R. Middleton (1988), Erosion of the eastern United States observed with $^{10}$Be, *Earth Surface Processes and Landforms*, *13*, 441-457.

Chen, J., J. Chen, A. Liao, X. Cao, L. Chen, X. Chen, C. He, G. Han, S. Peng, M. Lu, W. Zhang, X. Tong, and J. Mills (2015), Global land cover mapping at 30m resolution: A POK-based operational approach, *ISPRS Journal of Photogrammetry and Remote Sensing*, *103*(0), 7-27.

Chmeleff, J., F. v. Blanckenburg, K. Kossert, and D. Jakob (2009), Determination of the $^{10}$Be half-life by multicollector ICP-MS and liquid scintillation counting, *Nuclear Instruments and Methods in Physics Research Section B: Beam Interactions with Materials and Atoms*, *268*(2), 192-199.

Clapp, E., P. R. Bierman, and M. Caffee (2002), Using $^{10}$Be and $^{26}$Al to determine sediment generation rates and identify sediment source areas in an arid region drainage basin, *Geomorphology*, *45*, 89-104.

Clapp, E. M., P. R. Bierman, A. P. Schick, J. Lekach, Y. Enzel, and M. Caffee (2000), Sediment yield exceeds sediment production in arid region drainage basins, *Geology*, *28*(11), 995-998.

Clark, M. K., M. A. House, L. H. Royden, K. X. Whipple, B. C. Burchfiel, X. Zhang, and W. Tang (2005), Late Cenozoic uplift of southeastern Tibet, *Geology*, *33*(6), 525-528.

Clark, M. K., L. H. Royden, K. X. Whipple, B. C. Burchfiel, X. Zhang, and W. Tang (2006), Use of a regional, relict landscape to measure vertical deformation of the eastern Tibetan Plateau, *Journal of Geophysical Research: Earth Surface*, *111*(F3), F03002.

Collins, A. L., D. E. Walling, and G. J. L. Leeks (1997), Source type ascription for fluvial suspended sediment based on a quantitative composite fingerprinting technique, *CATENA*, *29*(1), 1-27.

Corbett, L. B., N. E. Young, P. R. Bierman, J. P. Briner, T. A. Neumann, D. H. Rood, and J. A. Graly (2011), Paired bedrock and boulder $^{10}$Be concentrations resulting from early Holocene ice retreat near Jakobshavn Isfjord, western Greenland, *Quaternary Science Reviews*, *30*(13–14), 1739-1749.

Cyr, A. J., and D. E. Granger (2008), Dynamic equilibrium among erosion, river incision, and coastal uplift in the northern and central Apennines, Italy, *Geology*, *36*(2), 103-106.

DiBiase, R. A., K. X. Whipple, A. M. Heimsath, and W. B. Ouimet (2010), Landscape form and millennial erosion rates in the San Gabriel Mountains, CA, *Earth and Planetary Science Letters*, *289*, 134-144.

Dyer, F. J., and J. M. Olley (1999), The effects of grain abrasion and disaggregation on $^{137}$Cs concentrations in different size fractions of soils developed on three different rock types, *Catena*, *36*, 143-151.

Fan, H., J. Hu, and D. He (2013), Trends in precipitation over the low latitude highlands of Yunnan, China, *J. Geogr. Sci.*, *23*(6), 1107-1122.

Fan, Q., K. Tanaka, A. Sakaguchi, H. Kondo, N. Watanabe, and Y. Takahashi (2014), Factors controlling radiocesium distribution in river sediments: Field and laboratory studies after the Fukushima Dai-ichi Nuclear Power Plant accident, *Applied Geochemistry*, *48*, 93-103.

Field, C. V., G. A. Schmidt, D. Koch, and C. Salyk (2006), Modeling production and climate-related impacts on $^{10}$Be concentration in ice cores, *Journal of Geophysical Research 111*, 13.

Fifield, L. K., R. J. Wasson, B. Pillans, and J. O. H. Stone (2010), The longevity of hillslope soil in SE and NW Australia, *Catena*, *81*, 32-42.

Flint, J. J. (1974), Stream gradient as a function of order, magnitude, and discharge, *Water Resources Research*, *10*(5), 969-973.

Foster, G. R., and R. E. Highfill (1983), Effect of terraces on soil loss: USLE P factor values for terraces, *Journal of Soil and Water Conservation*, *38*(1), 48-51.

Geology of Sanjiang Ministry of Geology and Mineral Resources (1986), Geological Map of Nujiang, Lancang, and Jinsha Rivers Area, Geological Publishing House, China Geological Map Printing House.

Godard, V., D. W. Burbank, D. L. Bourlès, B. Bookhagen, R. Braucher, and G. B. Fisher (2012), Impact of glacial erosion on $^{10}$Be concentrations in fluvial sediments of the Marsyandi catchment, central Nepal, *Journal of Geophysical Research: Earth Surface*, *117*(F3), F03013.

Graly, J. A., P. R. Bierman, L. J. Reusser, and M. J. Pavich (2010), Meteoric $^{10}$Be in soil profiles – a global meta-analysis, *Geochimica et Cosmochimica Acta*, *74*, 6814-6829.

Graly, J. A., L. J. Reusser, and P. R. Bierman (2011), Short and long-term delivery rates of meteoric $^{10}$Be to terrestrial soils, *Earth and Planetary Science Letters*, *302*(3–4), 329-336.

Granger, D. E., J. W. Kirchner, and R. Finkel (1996), Spatially averaged long-term erosion rates measured from *in situ*-produced cosmogenic nuclides in alluvial sediments, *Journal of Geology*, *104*(3), 249-257.

Granger, D. E., N. A. Lifton, and J. K. Willenbring (2013), A cosmic trip: 25 years of cosmogenic nuclides in geology, *Geological Society of America Bulletin*, *125*(9-10), 1379-1402.

He, Q., and D. E. Walling (1996), Interpreting particle size effects in the adsorption of $^{137}$Cs and unsupported $^{210}$Pb by mineral soils and sediments, *Journal of Environmental Radioactivity*, *30*(2), 117-137.

He, Q., and D. Walling (1997), The distribution of fallout $^{137}$Cs and $^{210}$Pb in undisturbed and cultivated soils, *Applied Radiation and Isotopes*, *48*(5), 677-690.

Heikkila, U., J. Beer, J. Jouzel, J. Feichter, and P. Kubik (2008), $^{10}$Be measured in a GRIP snow pit and modeled using the ECHAM5-HAM general circulation model, *Geophysical Research Letters*, *35*(L05817), 1-4.

Heisinger, B., D. Lal, A. J. T. Jull, P. Kubik, S. Ivy-Ochs, K. Knie, and E. Nolte (2002a), Production of selected cosmogenic radionuclides by muons: 2. Capture of negative muons, *Earth and Planetary Science Letters*, *200*(3-4), 357-369.

Heisinger, B., D. Lal, A. J. T. Jull, P. Kubik, S. Ivy-Ochs, S. Neumaier, K. Knie, V. Lazarev, and E. Nolte (2002b), Production of selected cosmogenic radionuclides by muons - 1. Fast muons, *Earth and Planetary Science Letters*, *200*, 345-355.

Henck, A. C., D. R. Montgomery, K. W. Huntington, and C. Liang (2010), Monsoon control of effective discharge, Yunnan and Tibet, *Geology*, *38*(11), 975-978.

Henck, A. C., K. W. Huntington, J. O. Stone, D. R. Montgomery, and B. Hallet (2011), Spatial controls on erosion in the Three Rivers Region, southeastern Tibet and southwestern China, *Earth and Planetary Science Letters*, *303*(1-2), 71-83.

Hewawasam, T., F. von Blackenburg, M. Schaller, and P. Kubik (2003), Increase of human over natural erosion rates in tropical highlands constrained by cosmogenic nuclides, *Geology*, *31*(7), 597-600.

Hooke, R. L. M.-D., Jose F. (2012), Land transformation by humans: A review, *GSA Today*, *22*(12), 4-10.

Hyde, W. F., B. Belcher, and J. Xu (2003), *China's forests: global lessons from market reforms*, Resources for the Future and CIFOR, Washington, DC.

Inbar, M., and C. A. Llerena (2000), Erosion processes in high mountain agricultural terraces in Peru, *Mountain Research and Development*, *20*(1), 72-79.

Jovanovic, S., A. Dlabac, and N. Mihaljevic (2010), ANGLE v2.1—New version of the computer code for semiconductor detector gamma-efficiency calculations, *Nuclear Instruments and Methods in Physics Research Section A: Accelerators, Spectrometers, Detectors and Associated Equipment*, *622*(2), 385-391.

Judson, S. (1968), Erosion of the land, or What's happening to our continents, *American Scientist*, *56*, 356-374.

Jull, A. J. T., E. M. Scott, and P. Bierman (2015), The CRONUS-Earth inter-comparison for cosmogenic isotope analysis, *Quaternary Geochronology*(0).

Jungers, M. C., P. R. Bierman, A. Matmon, K. Nichols, J. Larsen, and R. Finkel (2009), Tracing hillslope sediment production and transport with *in situ* and meteoric $^{10}$Be, *Journal of Geophysical Research*, *114*(F04020), 1-16.

Kaste, J. M., A. M. Heimsath, and B. C. Bostick (2007), Short-term soil mixing quantified with fallout radionuclides, *Geology*, *35*(3), 243-246.

Kirchner, J. W., R. C. Finkel, C. S. Riebe, D. E. Granger, J. L. Clayton, J. G. King, and W. F. Megahan (2001), Mountain erosion over 10 yr, 10 k.y., and 10 m.y. time scales, *Geology*, *29*(7), 591-594.

Kohl, C. P., and K. Nishiizumi (1992), Chemical isolation of quartz for measurement of *in-situ* -produced cosmogenic nuclides, *Geochimica et Cosmochimica Acta*, *56*, 3583-3587.

Koiter, A. J., P. N. Owens, E. L. Petticrew, and D. A. Lobb (2013), The behavioural characteristics of sediment properties and their implications for sediment fingerprinting as an approach for identifying sediment sources in river basins, *Earth-Science Reviews*, *125*(0), 24-42.

Lal, D., and B. Peters (1962), Cosmic-ray produced isotopes and their application to problems in geophysics, in *Progress in elementary particle and cosmic ray physics*, edited by J. G. Wilson and S. A. Wouthysen, pp. 1-74, Wiley, New York.

Lal, D., and B. Peters (1967), Cosmic ray produced radioactivity on the earth, in *Handbuch der Physik*, edited by K. Sitte, pp. 551-612, Springer-Verlag, New York.

Lal, D. (1988), *In situ*-produced cosmogenic isotopes in terrestrial rocks, *Annual Reviews of Earth and Planetary Science*, *16*, 355-388.

Lal, D. (1991), Cosmic ray labeling of erosion surfaces: *In situ* nuclide production rates and erosion models, *Earth and Planetary Science Letters*, *104*(2-4), 424-439.

Lauer, J. W., and J. Willenbring (2010), Steady state reach-scale theory for radioactive tracer concentration in a simple channel/floodplain system, *Journal of Geophysical Research: Earth Surface*, *115*(F4), F04018.

Liu-Zeng, J., P. Tapponnier, Y. Gaudemer, and L. Ding (2008), Quantifying landscape differences across the Tibetan plateau: Implications for topographic relief evolution, *Journal of Geophysical Research: Earth Surface*, *113*(F4), F04018.

Lu, X., and D. Higgitt (2000), Estimating erosion rates on sloping agricultural land in the Yangtze Three Gorges, China, from caesium-137 measurements, *Catena*, *39*(1), 33-51.

Mabit, L., M. Benmansour, and D. E. Walling (2008), Comparative advantages and limitations of the fallout radionuclides $^{137}Cs$, $^{210}Pb_{ex}$ and $^{7}Be$ for assessing soil erosion and sedimentation, *Journal of Environmental Radioactivity*, *99*, 1799-1807.

Mabit, L., M. Benmansour, J. Abril, D. Walling, K. Meusburger, A. Iurian, C. Bernard, S. Tarján, P. Owens, and W. Blake (2014), Fallout $^{210}Pb$ as a soil and sediment tracer in catchment sediment budget investigations: A review, *Earth-Science Reviews*, *138*, 335-351.

Magee, D. (2006), Powershed Politics: Yunnan Hydropower under Great Western Development, *The China Quarterly*, *185*, 23-41.

Masarik, J., and J. Beer (1999), Simulation of particle fluxes and cosmogenic nuclide production in the Earth's atmosphere, *Journal of Geophysical Research*, *104*(D10), 12099-12111.

Matisoff, G., and P. Whiting (2012), Measuring Soil Erosion Rates Using Natural ($^{7}$Be, $^{210}$Pb) and Anthropogenic ($^{137}$Cs, $^{239,240}$Pu) Radionuclides, in *Handbook of Environmental Isotope Geochemistry*, edited by M. Baskaran, pp. 487-519, Springer Berlin Heidelberg.

Matmon, A., P. R. Bierman, J. Larsen, S. Southworth, M. Pavich, and M. Caffee (2003a), Temporally and spatially uniform rates of erosion in the southern Appalachian Great Smoky Mountains, *Geology*, *31*(2), 155–158.

Matmon, A. S., P. Bierman, J. Larsen, S. Southworth, M. Pavich, R. Finkel, and M. Caffee (2003b), Erosion of an ancient mountain range, the Great Smoky Mountains, North Carolina and Tennessee, *American Journal of Science*, *303*, 817-855.

McKean, J. A., W. E. Dietrich, R. C. Finkel, J. R. Southon, and M. W. Caffee (1993), Quantification of soil production and downslope creep rates from cosmogenic $^{10}$Be accumulations on a hillslope profile, *Geology*, *21*(4), 343-346.

Miller, S. R., P. B. Sak, E. Kirby, and P. R. Bierman (2013), Neogene rejuvenation of central Appalachian topography: Evidence for differential rock uplift from stream profiles and erosion rates, *Earth and Planetary Science Letters*, *369–370*(0), 1-12.

Monaghan, M. C., S. Krishnaswami, and K. K. Turekian (1986), The global-average production rate of $^{10}$Be, *Earth and Planetary Science Letters*, *76*, 279-287.

Montgomery, D. R., and M. T. Brandon (2002), Topographic controls on erosion rates in tectonically active mountain ranges, *Earth and Planetary Science Letters*, *201*(3-4), 481-489.

NASA LP-DAAC (2012), ASTER GDEM, edited by NASA Land Processes Distributed Active Archive Center (LP DAAC), LP DAAC.

Nichols, K. K., P. R. Bierman, M. Caffee, R. Finkel, and J. Larsen (2005a), Cosmogenically enabled sediment budgeting, *Geology*, *33*(2), 133-136.

Nichols, K. k., P. r. Bierman, R. Finkel, and J. Larsen (2005b), Long-Term (10 to 20 kyr) Sediment Generation Rates for the Upper Rio Chagres Basin Based on Cosmogenic $^{10}$Be, in *The Rio Chagres: A Multidisciplinary Profile of a Tropical Watershed*, edited by R. S. Harmon, Kluwer Academic Publishers.

Nichols, K. K., P. R. Bierman, and D. H. Rood (2014), $^{10}$Be constrains the sediment sources and sediment yields to the Great Barrier Reef from the tropical Barron River catchment, Queensland, Australia, *Geomorphology*, *224*(0), 102-110.

Niemi, N. A., M. Oskin, D. W. Burbank, A. J. M. Heimsath, and E. J. Gabet (2005), Effects of bedrock landslides on cosmogenically determined erosion rates, *Earth and Planetary Science Letters*, *237*(3), 480-498.

Nishiizumi, K., M. Imamura, M. W. Caffee, J. R. Southon, R. C. Finkel, and J. McAninch (2007), Absolute calibration of $^{10}$Be AMS standards, *Nuclear Inst. and Methods in Physics Research, B*, *258*(2), 403-413.

NRC (2012), New Research Opportunities in the Earth Sciences, edited, National Academy Press, Washington, DC.

Nyffeler, U. P., Y.-H. Li, and P. H. Santschi (1984), A kinetic approach to describe trace-element distribution between particles and solution in natural aquatic systems, *Geochimica et Cosmochimica Acta*, *48*(7), 1513-1522.

O'Farrell, C. R., A. M. Heimsath, and J. M. Kaste (2007), Quantifying hillslope erosion rates and processes for a coastal California landscape over varying timescales, *Earth Surface Processes and Landforms*, *32*(4), 544-560.

Ouimet, W., D. Dethier, P. Bierman, C. Wyshnytzky, N. Shea, and D. H. Rood (2015), Spatial and temporal variations in meteoric $^{10}$Be inventories and long-term deposition rates, Colorado Front Range, *Quaternary Science Reviews*, *109*(0), 1-12.

Ouimet, W. B., K. X. Whipple, and D. E. Granger (2009), Beyond threshold hillslopes: Channel adjustment to base-level fall in tectonically active mountain ranges, *Geology*, *37*(7), 579-582.

Parsons, A. J., and I. D. L. Foster (2011), What can we learn about soil erosion from the use of $^{137}$Cs?, *Earth-Science Reviews*, *108*(1), 101-113.

Pavich, M., L. Brown, J. N. Valette-Silver, J. Klein, and R. Middleton (1985), $^{10}$Be analysis of a Quaternary weathering profile in the Virginia Piedmont, *Geology*, *13*, 39-41.

Pavich, M. J., L. Brown, J. W. Harden, J. Klein, and R. Middleton (1986), $^{10}$Be distribution in soils from Merced River terraces, California, *Geochimica et Cosmochimica Acta*, *50*(8), 1727-1735.

Perg, L. A., R. S. Anderson, and R. C. Finkel (2001), Use of a new $^{10}$Be and $^{26}$Al inventory method to date marine terraces, Santa Cruz, California, USA, *Geology*, *29*(10), 879-882.

Portenga, E. W., and P. R. Bierman (2011), Understanding Earth's eroding surface with $^{10}$Be, *GSA Today*, *21*(8), 4-10.

Preiss, N., M.-A. Mélières, and M. Pourchet (1996), A compilation of data on lead-210 concentration in surface air and fluxes at the air-surface and water-sediment interfaces, *Journal of Geophysical Research: Atmospheres*, *101*(D22), 28847-28862.

Quine, T., D. Walling, X. Zhang, and Y. Wang (1992), Investigation of soil erosion on terraced fields near Yanting, Sichuan Province, China, using caesium-137, *International Association of Hydrological Sciences Publication*(209), 155-168.

Reusser, L., P. Bierman, and D. Rood (2015), Quantifying human impacts on rates of erosion and sediment transport at a landscape scale, *Geology*.

Reusser, L. J., and P. R. Bierman (2010), Using meteoric $^{10}$Be to track fluvial sand through the Waipaoa River basin, New Zealand, *Geology*, *38*(1), 47-50.

Ritchie, J. C., and J. R. McHenry (1990), Application of Radioactive Fallout Cesium-137 for Measuring Soil Erosion and Sediment Accumulation Rates and Patterns: A Review, *Journal of Environmental Quality*(2), 215-233.

Savi, S., K. Norton, V. Picotti, F. Brardinoni, N. Akçar, P. W. Kubik, R. Delunel, and F. Schlunegger (2014), Effects of sediment mixing on $^{10}$Be concentrations in the Zielbach catchment, central-eastern Italian Alps, *Quaternary Geochronology*, *19*(0), 148-162.

Schaller, M., F. von Blanckenburg, N. Hovius, and P. W. Kubik (2001), Large-scale erosion rates from *in situ*-produced cosmogenic nuclides in European river sediments, *Earth and Planetary Science Letters*, *v. 188*, 441-458.

Schmidt, A. H., D. R. Montgomery, K. W. Huntington, and C. Liang (2011), The question of communist land degradation: new evidence from local erosion and basin-wide sediment yield in Southwest China and Southeast Tibet, *Annals of the Association of American Geographers*, *101*(3), 477-496.

Shen, C., J. Beer, P. W. Kubik, M. Suter, M. Borkovec, and T. S. Liu (2004), Grain size distribution, $^{10}$Be content and magnetic susceptibility of micrometer–nanometer loess materials, *Nuclear Instruments and Methods in Physics Research Section B: Beam Interactions with Materials and Atoms*, *223–224*(0), 613-617.

Sidle, R. C., A. D. Ziegler, J. N. Negishi, A. R. Nik, R. Siew, and F. Turkelboom (2006), Erosion processes in steep terrain—Truths, myths, and uncertainties related to forest management in Southeast Asia, *Forest Ecology and Management*, *224*(1–2), 199-225.

Smith, H. G., and W. H. Blake (2014), Sediment fingerprinting in agricultural catchments: A critical re-examination of source discrimination and data corrections, *Geomorphology*, *204*(0), 177-191.

Stone, J. (1998), A rapid fusion method for separation of beryllium-10 from soils and silicates, *Geochimica et Cosmochimica Acta*, *62*(3), 555-561.

Stout, J. C., P. Belmont, S. P. Schottler, and J. K. Willenbring (2014), Identifying sediment sources and sinks in the Root River, Southeastern Minnesota, *Annals of the Association of American Geographers*, *104*(1), 20-39.

Trac, C., S. Harrell, T. Hinckley, and A. Henck (2007), Reforestation programs in Southwest China: Reported success, observed failure, and the reasons why, *J. Mt. Sci.*, *4*(4), 275-292.

Trac, C. J., A. C. H. Schmidt, S. Harrell, and T. M. Hinckley (2013), Is the Returning Farmland to Forest Program a Success? Three case studies from Sichuan, *Environmental Practice*, *15*(3), 350-366.

Trimble, S. W. (1977), The fallacy of stream equilibrium in contemporary denudation studies, *American Journal of Science*, *277*, 876-887.

Urgenson, L. S., R. K. Hagmann, A. C. Henck, S. Harrell, T. M. Hinckley, S. J. Shepler, B. L. Grub, and P. M. Chi (2010), Social-ecological dynamics of a forested watershed in SW China, *Society And Ecology [online]*, *15*(5), 2.

Vanacker, V., F. von Blanckenburg, G. Govers, A. Molina, J. Poesen, J. Deckers, and P. Kubik (2007), Restoring dense vegetation can slow mountain erosion to near natural benchmark levels, *Geology*, *35*(4), 303-306.

Vanacker, V., F. von Blanckenburg, G. Govers, A. Molina, B. Campforts, and P. W. Kubik (2015), Transient river response, captured by channel steepness and its concavity, *Geomorphology*, *228*(0), 234-243.

von Blanckenburg, F. (2005), The control mechanisms of erosion and weathering at basin scale from cosmogenic nuclides in river sediment, *Earth and Planetary Science Letters*, *237*(3-4), 462-479.

von Blanckenburg, F., J. Bouchez, and H. Wittmann (2012), Earth surface erosion and weathering from the $^{10}$Be (meteoric)/$^{9}$Be ratio, *Earth and Planetary Science Letters*, *351–352*(0), 295-305.

Wallbrink, P. J., and A. S. Murray (1993), Use of fallout radionuclides as indicators of erosion processes, *Hydrological Processes*, *7*, 297-304.

Walling, D. E. (1983), The sediment delivery problem, *Journal of Hydrology*, *65*(1-3), 209-237.

Walling, D. E., and J. C. Woodward (1992), Use of radiometric fingerprints to derive information on suspended sediment sources, *Erosion and Sediment Transport Monitoring Programmes in River Basins*(210), 153-163.

Walling, D. E. (1999), Linking land use, erosion and sediment yields in river basins, *Hydrobiologia*, *410*, 223-240.

Walter, R. C., and D. J. Merritts (2008), Natural Streams and the Legacy of Water-Powered Mills, *Science*, *319*, 299-304.

West, N., E. Kirby, P. Bierman, R. Slingerland, L. Ma, D. Rood, and S. Brantley (2013), Regolith production and transport at the Susquehanna Shale Hills Critical Zone Observatory, Part 2: Insights from meteoric $^{10}$Be, *Journal of Geophysical Research: Earth Surface*, *118*(3), 1877-1896.

West, N., E. Kirby, P. Bierman, and B. A. Clarke (2014), Aspect-dependent variations in regolith creep revealed by meteoric $^{10}$Be, *Geology*, *42*(6), 507-510.

Whiting, P. J., E. C. Bonniwell, and G. Matisoff (2001), Depth and areal extent of sheet and rill erosion based on radionuclides in soils and suspended sediment, *Geology*, *29*(12), 1131-1134.

Wilkinson, B. H., and B. J. McElroy (2007), The impact of humans on continental erosion and sedimentation, *Geological Society of America Bulletin*, *119*(1), 140-156.

Willenbring, J. K., and F. von Blanckenburg (2010), Meteoric cosmogenic Beryllium-10 adsorbed to river sediment and soil: Applications for Earth-surface dynamics, *Earth-Science Reviews*, *98*, 105-122.

Willenbring, J. K., N. M. Gasparini, B. T. Crosby, and G. Brocard (2013), What does a mean mean? The temporal evolution of detrital cosmogenic denudation rates in a transient landscape, *Geology*, *41*(12), 1215-1218.

Wittmann, H., F. von Blanckenburg, T. Kruesmann, K. P. Norton, and P. W. Kubik (2007), Relation between rock uplift and denudation from cosmogenic nuclides in river sediment in the Central Alps of Switzerland, *Journal of Geophysical Research*, *112*(F04010).

Wittmann, H., F. von Blanckenburg, J. Bouchez, N. Dannhaus, R. Naumann, M. Christl, and J. Gaillardet (2012), The dependence of meteoric $^{10}$Be concentrations on particle size in Amazon River bed sediment and the extraction of reactive $^{10}$Be/$^{9}$Be ratios, *Chemical Geology*, *318–319*(0), 126-138.

Wobus, C., K. X. Whipple, E. Kirby, N. Snyder, J. Johnson, K. Spyropolou, B. Crosby, and D. Sheehan (2006), Tectonics from topography: Procedures, promise and pitfalls, *Tectonics, climate, and landscape evolution: Geological Society of America Special Paper*, *398*, 55–74.

Wyshnytzky, C. E., W. B. Ouimet, J. McCarthy, D. P. Dethier, R. R. Shroba, P. R. Bierman, and D. H. Rood (2015), Meteoric $^{10}$Be, clay, and extractable iron depth profiles in the Colorado Front Range: Implications for understanding soil mixing and erosion, *CATENA*, *127*, 32-45.

Xu, S., A. B. Dougans, S. P. H. T. Freeman, C. Schnabel, and K. M. Wilcken (2010), Improved $^{10B}$e and $^{26}$Al-AMS with a 5MV spectrometer, *Nuclear Instruments and Methods in Physics Research Section B: Beam Interactions with Materials and Atoms*, *268*(7–8), 736-738.

Xu, S., S. P. H. T. Freeman, D. H. Rood, and R. P. Shanks (2015), Decadal $^{10}$Be, $^{26}$Al and $^{36}$Cl QA measurements on the SUERC 5 MV accelerator mass spectrometer, *Nuclear Instruments and Methods in Physics Research Section B: Beam Interactions with Materials and Atoms*(0).

Yang, S.-l., Q.-y. Zhao, and I. M. Belkin (2002), Temporal variation in the sediment load of the Yangtze river and the influences of human activities, *Journal of Hydrology*, *263*(1–4), 56-71.

Yanites, B. J., G. E. Tucker, and R. S. Anderson (2009), Numerical and analytical models of cosmogenic radionuclide dynamics in landslide‐dominated drainage basins, *Journal of Geophysical Research: Earth Surface (2003–2012)*, *114*(F1).

Yatagai, A., K. Kamiguchi, O. Arakawa, A. Hamada, N. Yasutomi, and A. Kitoh (2012), APHRODITE: Constructing a Long-Term Daily Gridded Precipitation Dataset for Asia Based on a Dense Network of Rain Gauges, *Bulletin of the American Meteorological Society*, *93*(9), 1401-1415.

You, C.-F., T. Lee, and Y.-H. Li (1989), The partition of Be between soil and water, *Chemical Geology*, *77*(2), 105-118.

## Tables and Figures

**Table 1.** Contemporary and long-term sediment yields

| Basin ID | Years of Record | Area ($km^2$) | Contemporary Sediment Yield (t/yr $km^2$) | Long-term Sediment Yield (t/yr $km^2$) | Contemporary/ Long-term Sediment Yield | Contemporary Erosion Indices | Long-term Erosion Indices |
|---|---|---|---|---|---|---|---|
| 35 | 24 | 198 | 124 | 250 | 0.50 | 0.63 | 1.27 |
| 49 | 22 | 2508 | 303 | 285 | 1.06 | 0.27 | 0.25 |
| 11 | 23 | 1006 | 64 | 128 | 0.50 | 0.40 | 0.80 |

[1] Calculated from data presented by *Henck et al.* [2010] and *Schmidt et al.* [2011]

[2] A large dam completed in 2012 at the junction of the north and south arms of basin 35 has reduced sediment yield from the south arm, resulting in an assumed underestimate of long-term sediment flux.

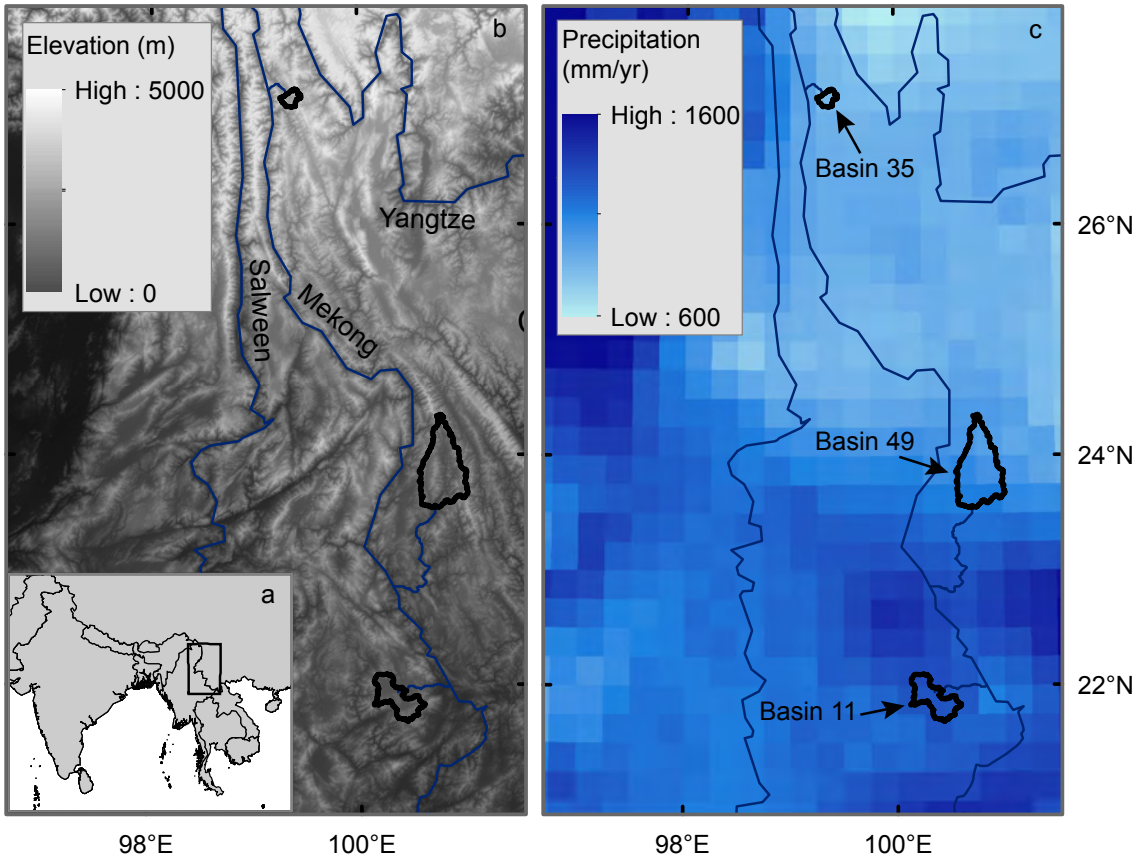
Elevation (m)
High : 5000
Low : 0
b
Yangtze
Salween
Mekong
a
Precipitation
(mm/yr)
High : 1600
Low : 600
c
Basin 35
Basin 49
Basin 11
26°N
24°N
22°N
98°E
100°E
98°E
100°E

**Figure 1**

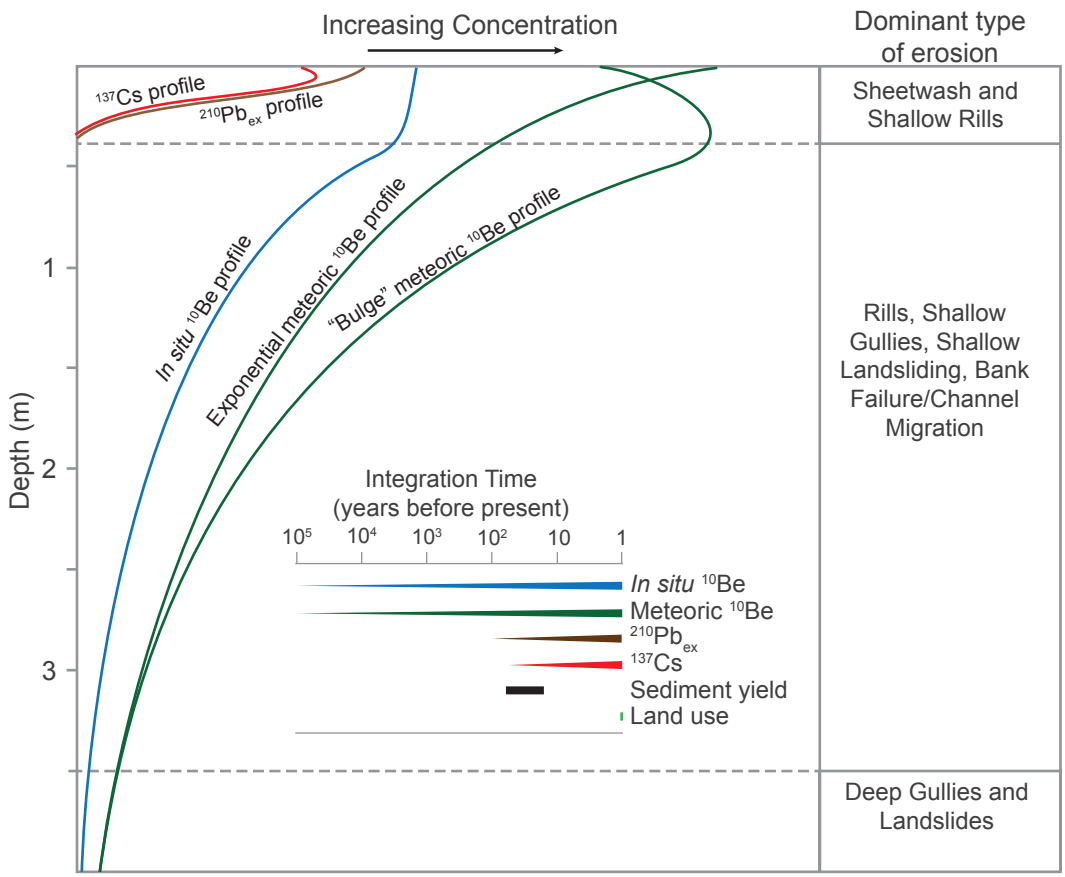
Increasing Concentration
Dominant type of erosion
$^{137}$Cs profile
$^{210}$Pb$_{ex}$ profile
Sheetwash and Shallow Rills
In situ $^{10}$Be profile
Exponential meteoric $^{10}$Be profile
"Bulge" meteoric $^{10}$Be profile
Depth (m)
1
2
3
Rills, Shallow Gullies, Shallow Landsliding, Bank Failure/Channel Migration
Integration Time
(years before present)
$10^5$ $10^4$ $10^3$ $10^2$ 10 1
In situ $^{10}$Be
Meteoric $^{10}$Be
$^{210}$Pb$_{ex}$
$^{137}$Cs
Sediment yield
Land use
Deep Gullies and Landslides

**Figure 2**

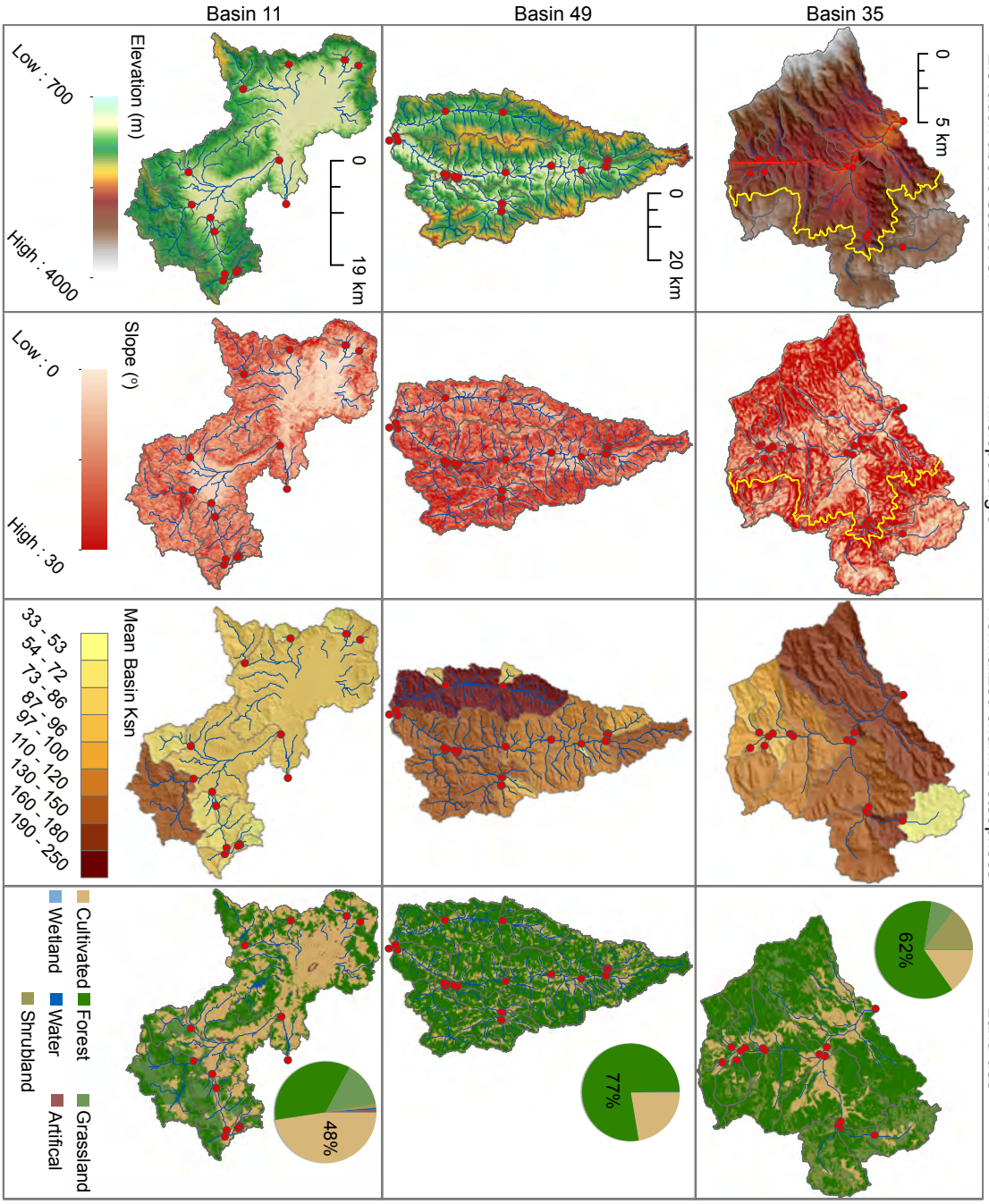
Basin 35
Basin 49
Basin 11
Elevation above sea level
Hillslope angle
Normalized channel steepness
Land-use
0
5 km
0
20 km
0
19 km
Elevation (m)
Low : 700
High : 4000
Slope (°)
Low : 0
High : 30
Mean Basin Ksn
33 - 53
54 - 72
73 - 86
87 - 97
97 - 110
110 - 130
130 - 160
160 - 190
190 - 250
62%
77%
48%
Cultivated
Forest
Grassland
Wetland
Water
Artifical
Shrubland

**Figure 3**

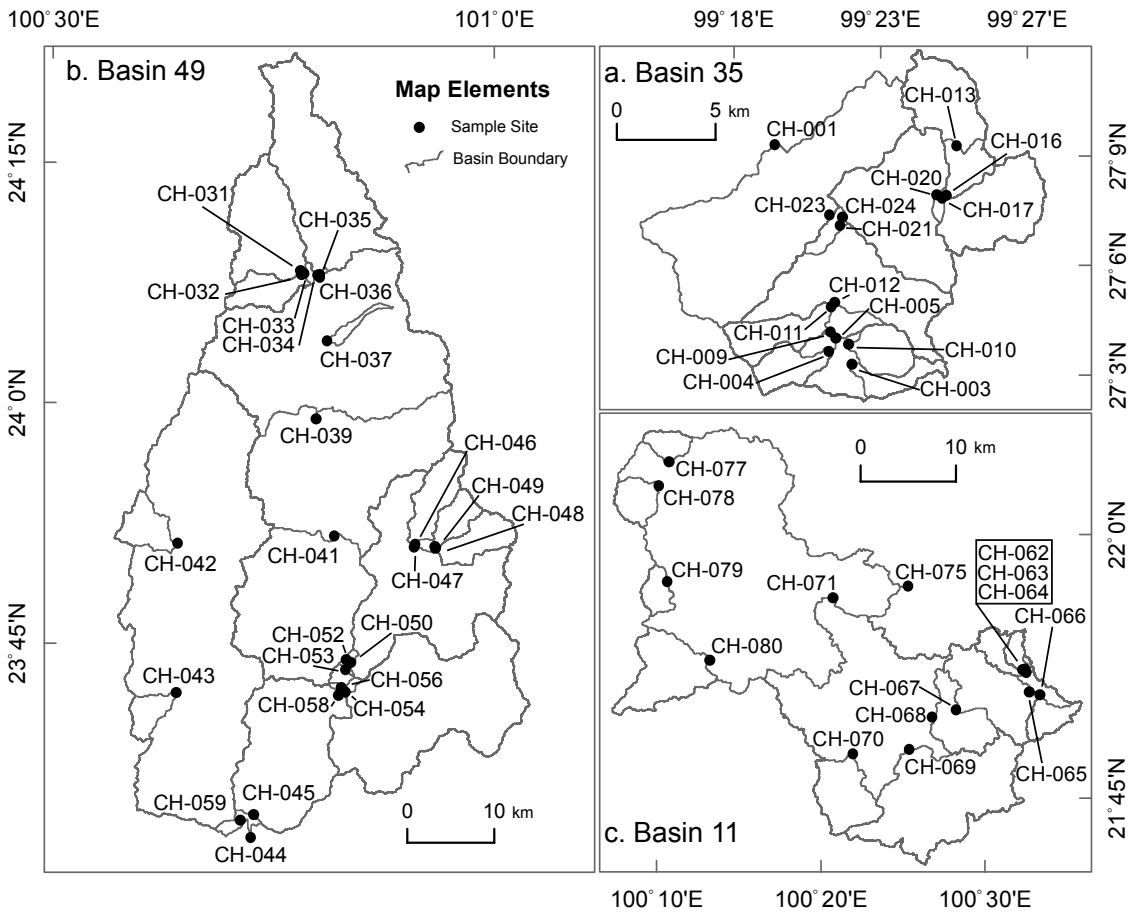
100° 30'E
101° 0'E
99° 18'E
99° 23'E
99° 27'E
24° 15'N
24° 0'N
23° 45'N
27° 9'N
27° 6'N
27° 3'N
22° 0'N
21° 45'N
b. Basin 49
Map Elements
Sample Site
Basin Boundary
CH-031
CH-035
CH-032
CH-036
CH-033
CH-034
CH-037
CH-039
CH-046
CH-049
CH-048
CH-042
CH-041
CH-047
CH-052
CH-050
CH-053
CH-043
CH-056
CH-058
CH-054
CH-059
CH-045
CH-044
0
10 km
a. Basin 35
0
5 km
CH-013
CH-001
CH-016
CH-020
CH-023
CH-024
CH-017
CH-021
CH-012
CH-005
CH-011
CH-010
CH-009
CH-004
CH-003
0
10 km
CH-077
CH-078
CH-079
CH-071
CH-075
CH-062
CH-063
CH-064
CH-066
CH-080
CH-067
CH-068
CH-070
CH-069
CH-065
c. Basin 11
100° 10'E
100° 20'E
100° 30'E

**Figure 4**

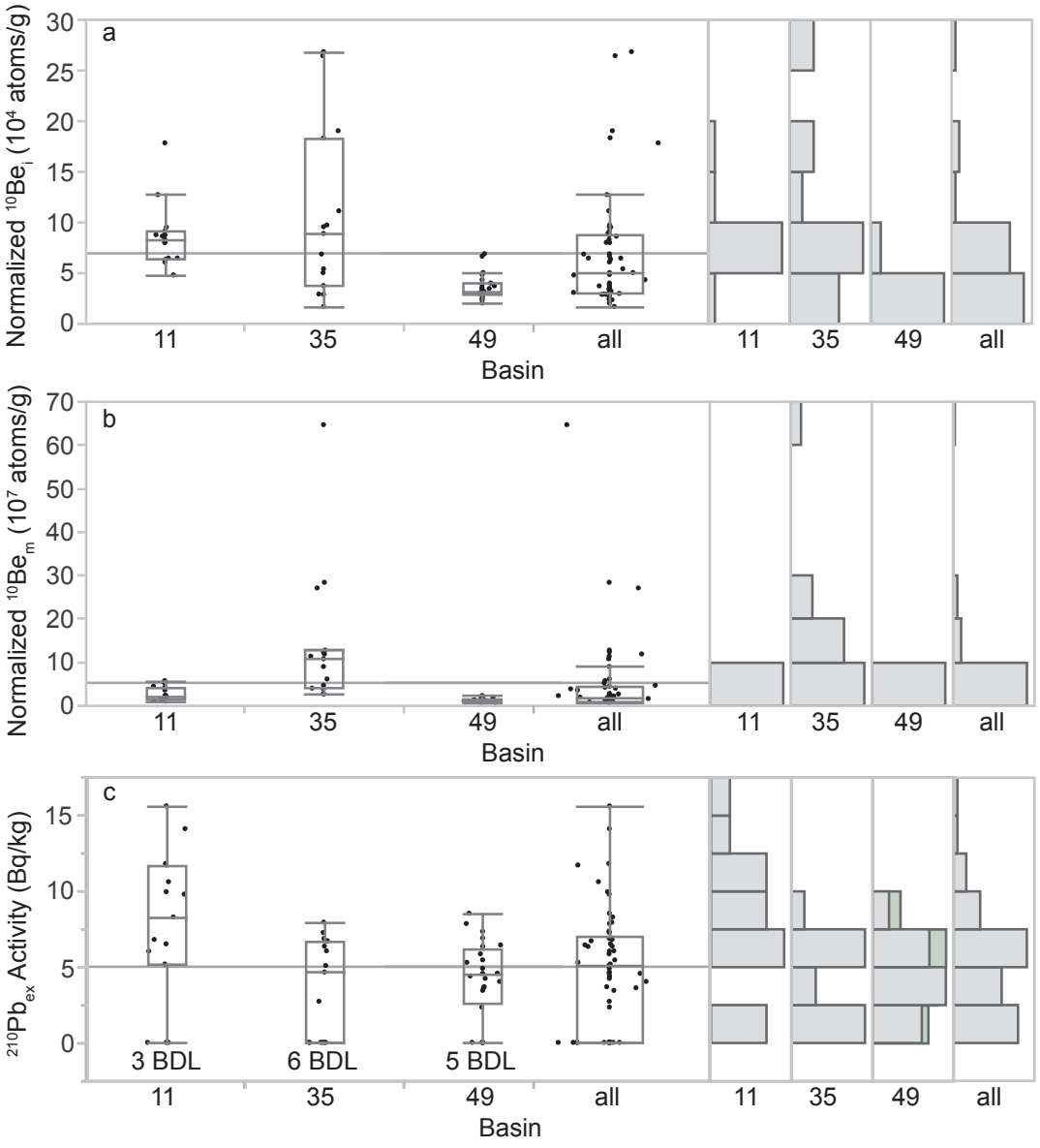
a
Normalized $^{10}Be_i$ ($10^4$ atoms/g)
30
25
20
15
10
5
0
11
35
49
all
Basin
b
Normalized $^{10}Be_m$ ($10^7$ atoms/g)
70
60
50
40
30
20
10
0
c
$^{210}Pb_{ex}$ Activity (Bq/kg)
15
10
5
0
3 BDL
6 BDL
5 BDL

**Figure 5**

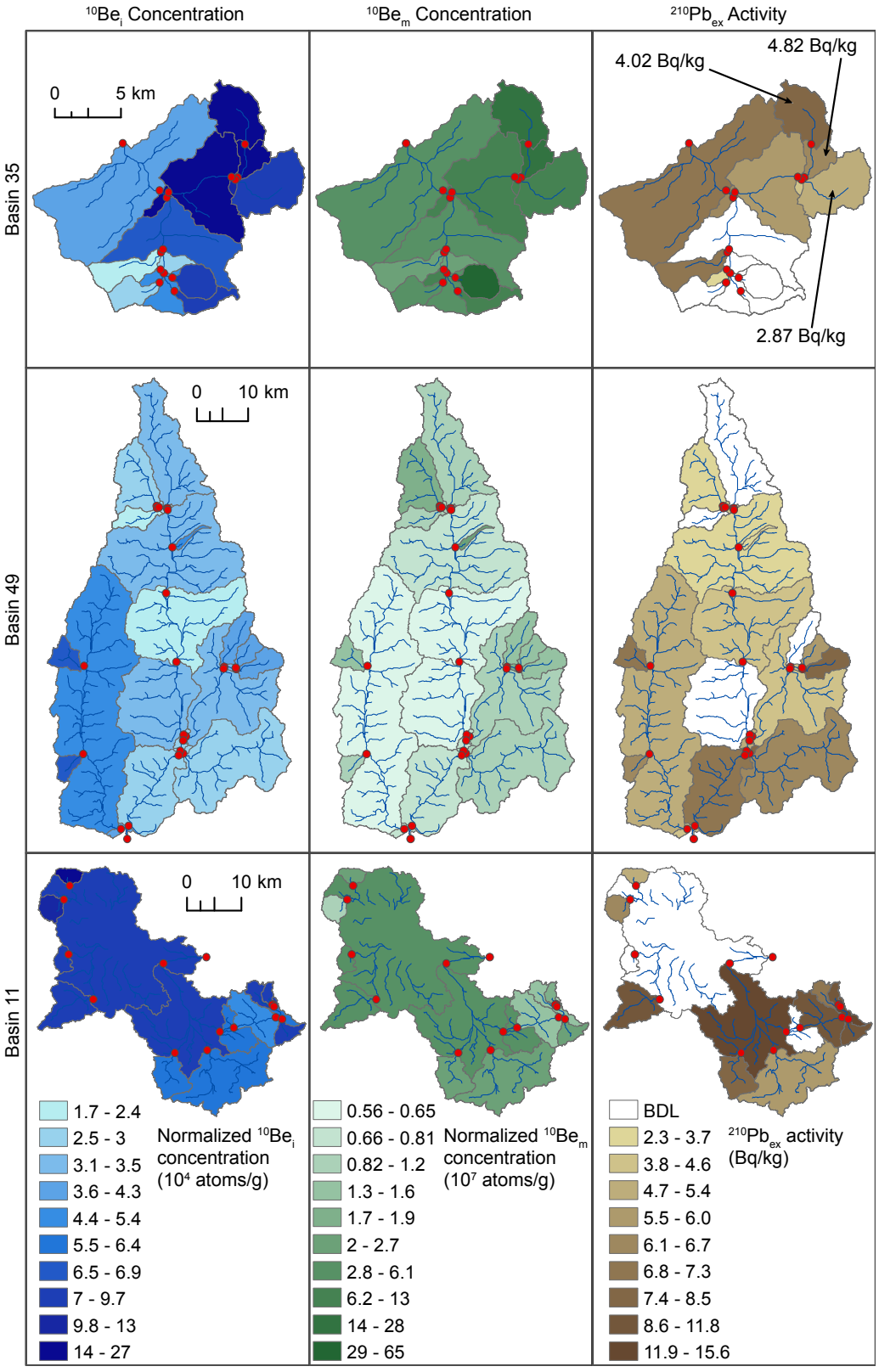
$^{10}Be_i$ Concentration
$^{10}Be_m$ Concentration
$^{210}Pb_{ex}$ Activity
Basin 35
Basin 49
Basin 11
0 5 km
0 10 km
0 10 km
4.02 Bq/kg
4.82 Bq/kg
2.87 Bq/kg
1.7 - 2.4
2.5 - 3
3.1 - 3.5
3.6 - 4.3
4.4 - 5.4
5.5 - 6.4
6.5 - 6.9
7 - 9.7
9.8 - 13
14 - 27
Normalized $^{10}Be_i$ concentration ($10^4$ atoms/g)
0.56 - 0.65
0.66 - 0.81
0.82 - 1.2
1.3 - 1.6
1.7 - 1.9
2 - 2.7
2.8 - 6.1
6.2 - 13
14 - 28
29 - 65
Normalized $^{10}Be_m$ concentration ($10^7$ atoms/g)
BDL
2.3 - 3.7
3.8 - 4.6
4.7 - 5.4
5.5 - 6.0
6.1 - 6.7
6.8 - 7.3
7.4 - 8.5
8.6 - 11.8
11.9 - 15.6
$^{210}Pb_{ex}$ activity (Bq/kg)

**Figure 6**

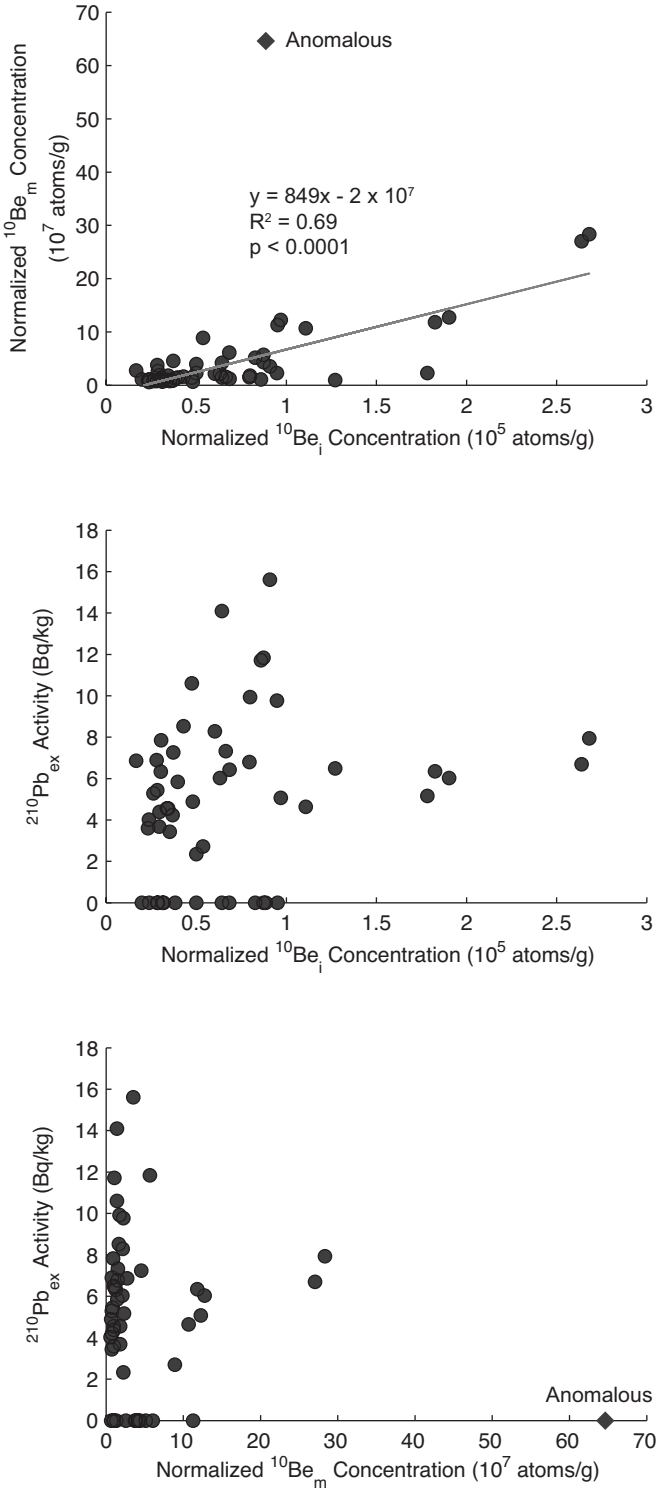
Anomalous
y = 849x - 2 x 10^7
R² = 0.69
p < 0.0001
Normalized ¹⁰Be_m Concentration (10⁷ atoms/g)
Normalized ¹⁰Be_i Concentration (10⁵ atoms/g)
²¹⁰Pb_ex Activity (Bq/kg)
Normalized ¹⁰Be_i Concentration (10⁵ atoms/g)
²¹⁰Pb_ex Activity (Bq/kg)
Anomalous
Normalized ¹⁰Be_m Concentration (10⁷ atoms/g)

**Figure 7**

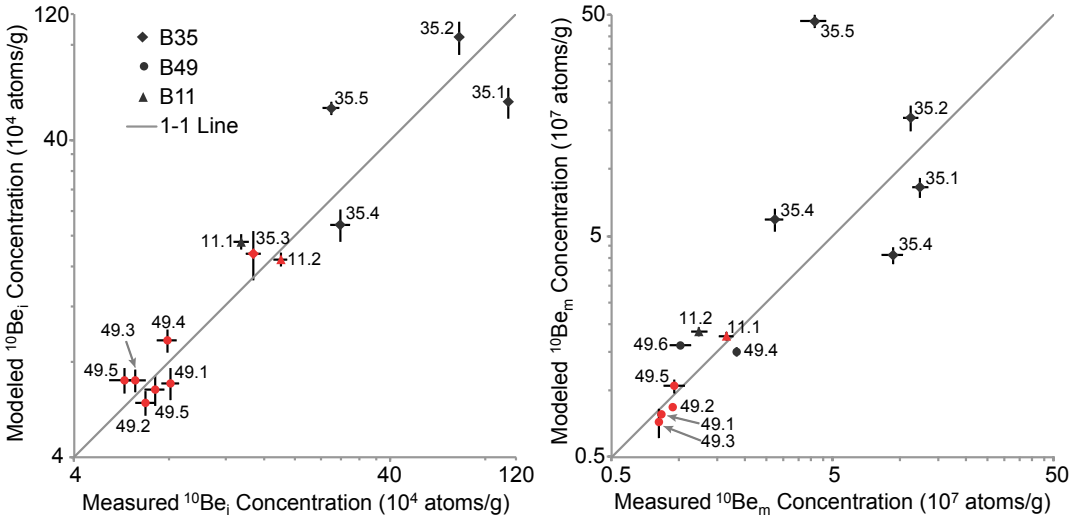
B35
B49
B11
1-1 Line
Modeled $^{10}Be_i$ Concentration ($10^4$ atoms/g)
Measured $^{10}Be_i$ Concentration ($10^4$ atoms/g)
Modeled $^{10}Be_m$ Concentration ($10^7$ atoms/g)
Measured $^{10}Be_m$ Concentration ($10^7$ atoms/g)
35.2
35.5
35.1
35.4
11.1
35.3
11.2
49.3
49.4
49.5
49.1
49.5
49.2
49.6
49.4
49.2
49.1
49.3

**Figure 8**

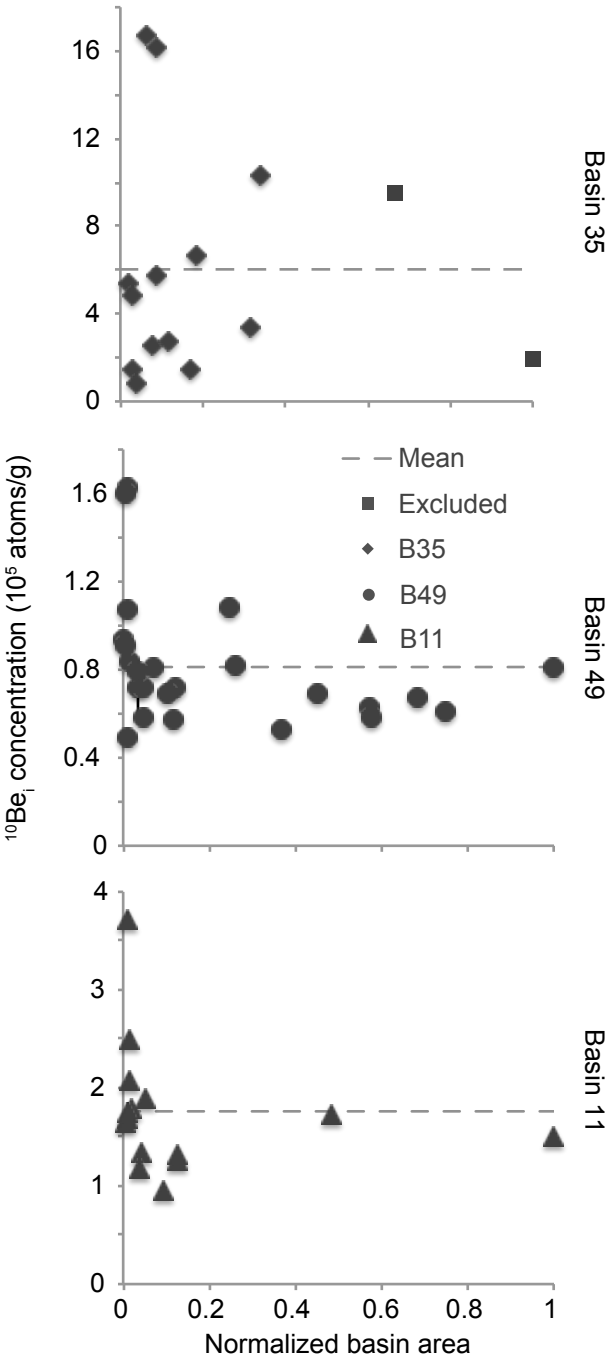
Basin 35
Basin 49
Basin 11
Mean
Excluded
B35
B49
B11
$^{10}Be_i$ concentration ($10^5$ atoms/g)
Normalized basin area
0
4
8
12
16
0.4
0.8
1.2
1.6
1
2
3
0.2
0.6

**Figure 9**

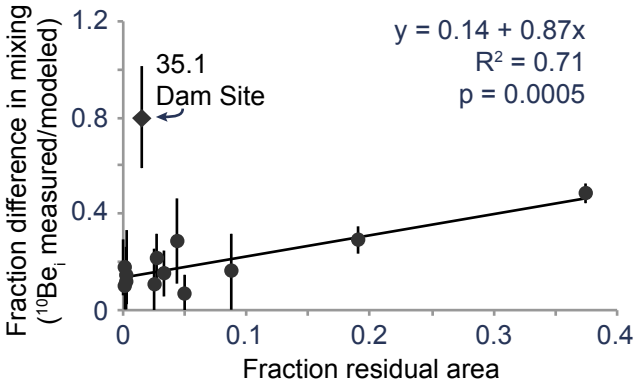
Fraction difference in mixing
($^{10}Be_i$ measured/modeled)
1.2
0.8
0.4
0
35.1
Dam Site
y = 0.14 + 0.87x
$R^2$ = 0.71
p = 0.0005
0
0.1
0.2
0.3
0.4
Fraction residual area

**Figure 10**

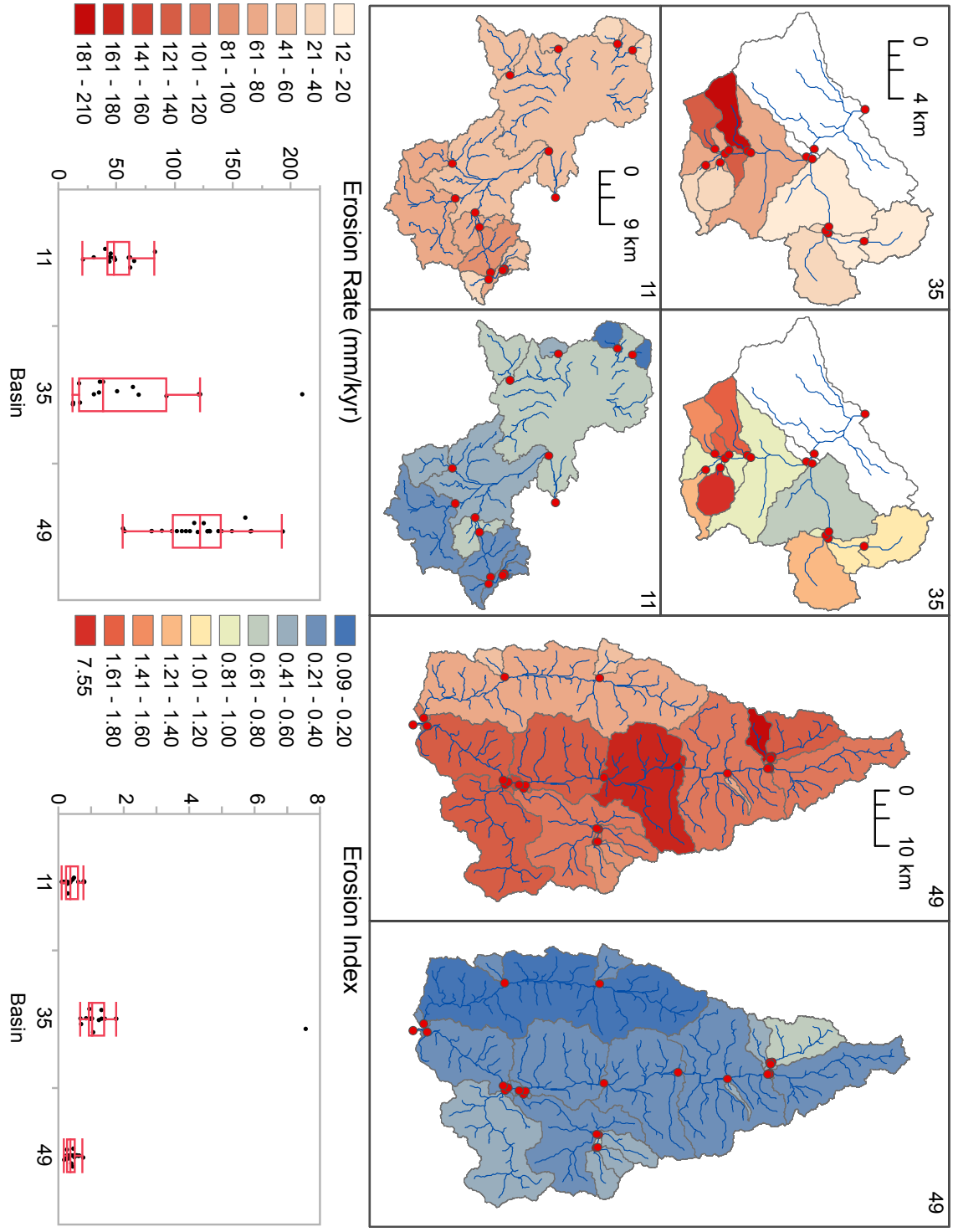
0
4 km
35
11
0
9 km
11
35
49
0
10 km
49
12 - 20
21 - 40
41 - 60
61 - 80
81 - 100
101 - 120
121 - 140
141 - 160
161 - 180
181 - 210
Erosion Rate (mm/kyr)
0
50
100
150
200
11
35
49
Basin
0.09 - 0.20
0.21 - 0.40
0.41 - 0.60
0.61 - 0.80
0.81 - 1.00
1.01 - 1.20
1.21 - 1.40
1.41 - 1.60
1.61 - 1.80
7.55
Erosion Index
0
2
4
6
8
11
35
49
Basin

**Figure 11**

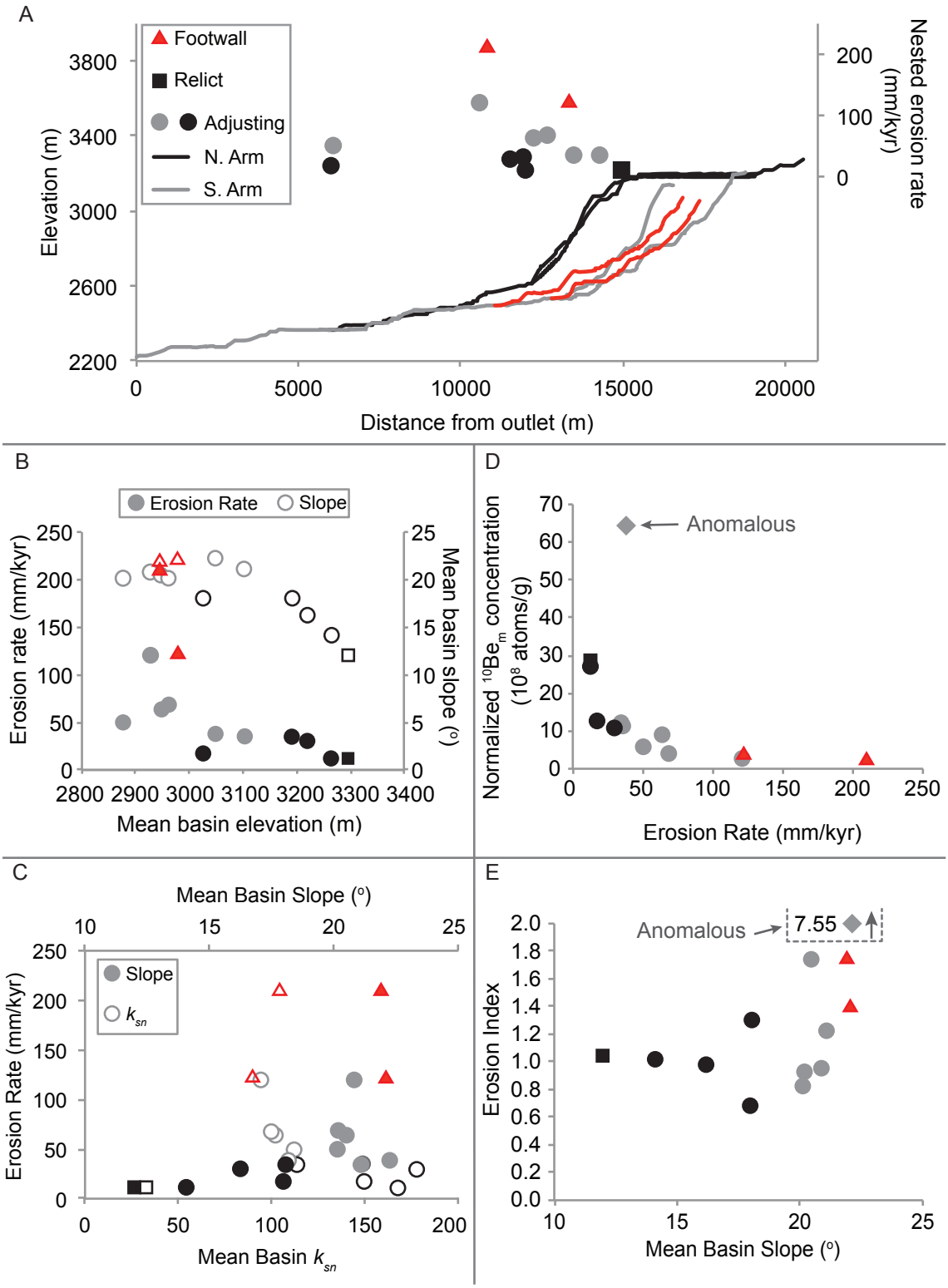
A
Footwall
Relict
Adjusting
N. Arm
S. Arm
Elevation (m)
3800
3400
3000
2600
2200
0
5000
10000
15000
20000
Distance from outlet (m)
200
100
0
Nested erosion rate (mm/kyr)
B
Erosion Rate
Slope
Erosion rate (mm/kyr)
250
200
150
100
50
0
25
20
15
10
5
0
Mean basin slope (°)
2800 2900 3000 3100 3200 3300 3400
Mean basin elevation (m)
D
Anomalous
Normalized $^{10}Be_m$ concentration ($10^8$ atoms/g)
70
60
50
40
30
20
10
0
0
50
100
150
200
250
Erosion Rate (mm/kyr)
C
Mean Basin Slope (°)
10
15
20
25
Slope
$k_{sn}$
Erosion Rate (mm/kyr)
250
200
150
100
50
0
0
50
100
150
200
Mean Basin $k_{sn}$
E
Anomalous
7.55
Erosion Index
2.0
1.8
1.6
1.4
1.2
1.0
0.8
0.6
0.4
0.2
0.0
10
15
20
25
Mean Basin Slope (°)

**Figure 12**

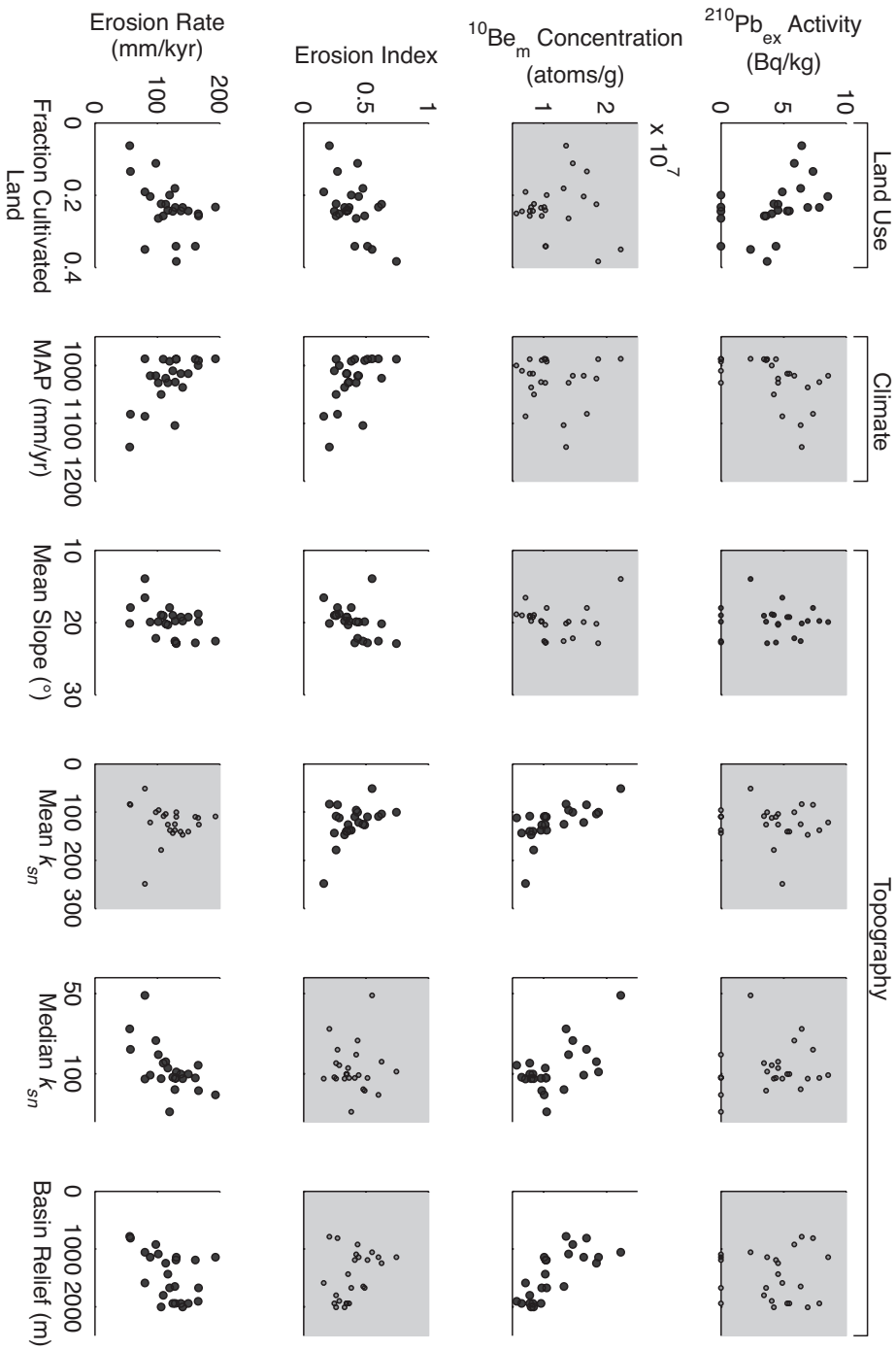
Land Use
Climate
Topography
$^{210}Pb_{ex}$ Activity (Bq/kg)
$^{10}Be_m$ Concentration (atoms/g)
x $10^7$
Erosion Index
Erosion Rate (mm/kyr)
Fraction Cultivated Land
MAP (mm/yr)
Mean Slope (°)
Mean $k_{sn}$
Median $k_{sn}$
Basin Relief (m)

**Figure 13**


**Figure 14**

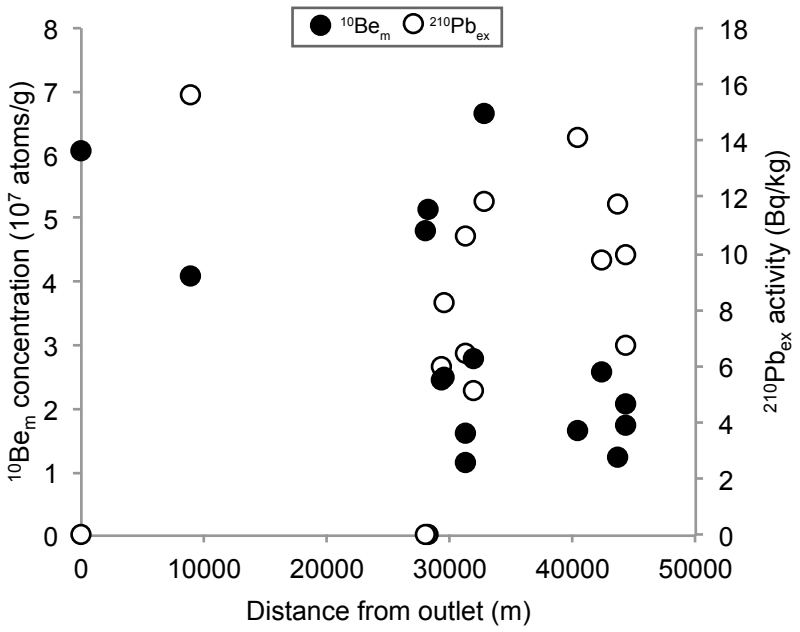
$^{10}Be_m$
$^{210}Pb_{ex}$
$^{10}Be_m$ concentration ($10^7$ atoms/g)
$^{210}Pb_{ex}$ activity (Bq/kg)
Distance from outlet (m)
0
10000
20000
30000
40000
50000
0
1
2
3
4
5
6
7
8
0
2
4
6
8
10
12
14
16
18

**Figure 15**

Figure Captions

Figure 1. Inset shows the region of interest within Southeast Asia (a), and primary panels show the locations of the basins sampled, topography (b) [*NASA,* 2012], and mean annual precipitation (c) [*Yatagai et al.,* 2012].

Figure 2. Idealized diagram of typical isotopic activity with depth below the surface for $^{10}Be_i$, $^{10}Be_m$, $^{137}Cs$, and $^{210}Pb_{ex}$. Two profiles are given for $^{10}Be_m$: one shows a sub-surface maximum common in well developed, slowly eroding soils, and the other an exponential decline typical of poorly-developed, quickly eroding soils [*Graly et al.,* 2010]. The column on right lists erosional processes and their expected erosional depths. Accumulation depths modeled from *Walling and Woodward* [1992], *Perg et al.* [2001], and *Graly et al.* [2010]. The inset shows the time over which each isotope integrates erosion, as well as the time frame covered by sediment yield and land-use data included in this study.

Figure 3. The topography, hillslope angle, mean basin $k_{sn}$ of the contributing area for each sample, and land use of basins 35, 49, and 11. Pie charts show the percentage of each land-use category in the basin, with the percentage of the most prevalent land-use noted on the chart. Topography, $k_{sn}$, and slope angle are derivatives of 30 m ASTER DEM's

(NASA, 2012), and land use is provided by GLC30 [*Chen et al.,* 2015]. In basin 35, the yellow line denotes the boundary between adjusting and relict landscape, and the red line denotes an east-down normal fault (dotted where inferred from field observations, solid where mapped [*Geology of Sanjiang Ministry of Geology and Mineral Resources*, 1986]).

Figure 4. Map shows the location, basin boundary, and sample ID for each sample in basin 35 (a), 49 (b), and 11 (c).

Figure 5. Bar-and-whisker plots and histograms of normalized $^{10}Be_i$ (a) and $^{10}Be_m$ (b) concentrations and activity of $^{210}Pb_{ex}$ (c) for each basin as well as combined. The number of samples for which $^{210}Pb_{ex}$ is below the detection limit in each basin are listed below the data (c). The lower and upper limits of the central boxes indicate the 1$^{st}$ and 3$^{rd}$ quartiles, respectively, the central line indicates the median, and the whiskers extend to 1.5 times the inter-quartile range. The grey line indicates the grand mean of all samples.

Figure 6. Maps show the normalized concentration of $^{10}Be_i$ and $^{10}Be_m$, and activity of $^{210}Pb_{ex}$ in basins 35, 49, and 11. The three samples containing $^{137}Cs$ are indicated by arrows and activity. Concentration and activity are reported and mapped as the value for the entire area contributing to the sample location.

Figure 7. Bivariate plots of normalized $^{10}Be_i$ and normalized $^{10}Be_m$ (a), normalized $^{10}Be_i$ and $^{210}Pb_{ex}$ (b), and normalized $^{10}Be_m$ and $^{210}Pb_{ex}$ (c). Plots include all samples, and an anomalously high $^{10}Be_m$ concentration is shown as a diamond and excluded from the regression in 7a. For dsiplay purposes, samples below the $^{210}Pb_{ex}$ detection limit are shown as zero.

Figure 8. Plots showing the measured and modeled concentrations of $^{10}Be_i$ and $^{10}Be_m$ at each junction in log-log space. The 1-1 line on each plot represents complete mixing, and samples which intersect the line within error (shown as 2 SD) are considered adequately mixed, and a red data point indicate the sample is well mixed or within 6% of well mixed.

Figure 9. Plots showing the normalized sub-basin area and $^{10}Be_i$ concentration of all samples in each basin and the mean $^{10}Be_i$ concentration of each basin shown as a dashed line. Samples collected below junction 35.1, shown as sqaures, are excluded from the calculation of mean concentration in basin 35, and are shown for reference only.

Figure 10. A plot of the fraction residual area and the absolute fraction difference in

mixing between the measured and modeled $^{10}Be_i$ concetrations. Junction 35.1, which is affected by a dam, is not included in the regression. Error bars show convolved mixing and measurement error at 2 SD.

Figure 11. Maps showing erosion rate and erosion index for the entire contributing area at each sample site. Samples below junction 35.1 are not shown due to a dam immediately above the junction. Bar-and-whisker plots show the distribution of erosion rates and erosion indices by basin. The lower and upper limits of the central boxes indicate the 1st and 3rd quartiles, respectively, the central line indicates the median, and the whiskers extend to 1.5 times the inter-quartile range.

Figure 12. Channel profiles for sampled sub-basins within basin 35 and erosion rates by distance from the outlet (A). Channel profiles end where the upstream area falls below ~0.54 $km^2$. Scatter plots show relationships between elevation, slope, and erosion rate (B), mean $k_{sn}$ and erosion rate (C), erosion rate and normalized $^{10}Be_m$ concentration (D), and erosion rate and erosion index (E). The anomalously high sample in plots D and E is CH-010.

Figure 13. A scatter plot matrix showing the relationships between land use, climate, and topographic metrics and isotopic erosion metrics. Plots with grey backgrounds do not

yeild statistically signficant linear regressions, and plots with white backgrounds yield linear regressions significant to $p<0.05$. For display purposes, samples with $^{210}Pb_{ex}$ below the detection limit are shown as zero, and are excluded from regression analysis. For full correlation matrix see table S3.

Figure 14. Photographs taken from basin 11 in 2013 during sampling. Phtographs show typical upland land use near samples CH-062, -063, and -064 (A), mid-elevation and lowland land use near sample CH-077, looking S-SW (B), and a heavily incised channel, with person in foreground for scale, at sample CH-068 (C).

Figure 15. Scatter plot shows the concentration of $^{10}Be_m$ (filled circles), and the activity of $^{210}Pb_{ex}$ (hollow circles) by the sample distance upstream of the basin outlet. For display purposes, $^{210}Pb_{ex}$ samples below the detection limit are plotted as zero.

# Chapter 3: Conclusions

## 1 Conclusions

Analysis of $^{10}Be_i$, $^{10}Be_m$, $^{210}Pb_{ex}$, and $^{137}Cs$ measured on fluvial sand provides significant insight into long- and short-term controls on erosion in the lower Chinese Mekong River and highlights the utility of using multiple isotopic methods for tracking erosion.

In the Yongchun River (Basin 35), tectonic uplift has resulted in a transient landscape where headward migrating knickpoints are eroding a low-slope, high-elevation landscape. This landscape erodes at an order of magnitude slower rate over the long-term than the actively adjusting landscape. The proportion relict landscape, and thus slope steepnees, in a sub-basin is the primary control of long-term erosion, and hillslope steepness is the best topographic indicator of erosion. Channel steepness is greatest in sub-basins containing a significant portion of relict landscape, and the data show a lag between channel incision from knickpoint migration and hillslope steepening, which drives overall erosion of the watershed. Knickpoint migration exerts a broad control over short-lived isotope activity; however, the parameters considered do not completely explain the high variability of fallout radionuclides in the Yongchun River.

Hillslope and channel steepness, mean annual precipitation, and cultivated land area are all related to long-term measures of erosion in the Weiyuan River (Basin 49); however, cultivation appears to drive short-term erosion. Land use is either forested or cultivated in the basin, and the most heavily cultivated sub-basins may have begun to erode through the mixed portion of the $^{10}Be_i$ soil profile, approximately 0.5 m. Modern

erosion in the Weiyuan River is focused in the cultivated areas; however, this has not increased contemporary sediment yield, likely the result of sediment storage within the basin.

Cultivation is most influential in the Nankai River basin (Basin 11), where upland deforestation is suspected to generate significant amounts of sediment slowly transported through the basin due to river diversion for irrigation of rice and sugarcane paddies. Contemporary sediment yield is depressed from the long-term average due to net sediment storage in agricultural terraces. As a result, fallout radionuclide activities are enriched closer to the basin outlet, and their concentrations are better related to sediment storage than erosion. The lack of correlation between any topographic property and long-term erosion rates suggests that land-use has also altered the concentration of $^{10}Be_i$ in sediment.

Overall, the lack of $^{137}Cs$ in nearly all samples and wide range of $^{210}Pb_{ex}$ concentrations provides compelling evidence of relatively high erosion rates during and after the time of $^{137}Cs$ deposition, followed by slower erosion from the end of the century to present day. In the context of the land-use, field observations, and long-term erosion indicators, this shift in erosion is likely the result of Chinese policies that resulted in documented widespread deforestation from the 1950's to the late 1980's and the implementation of policies aimed at forest conservation and restoration in the late 1990's. This is a significant finding, as it corroborates, at least to a certain degree, the government reported success of the Natural Forest Protection Program and "Returning Farmland to Forest," both top-down conservation policies introduced in the late 1990's

and early 2000's – policies whose implementation and effectiveness has largely been called into question by other research conducted in the region.

## 2 Future work

The greatest shortcoming of the multiple isotope method used in this study is the inability to make quantitative comparisons between independently derived erosion rates applicable over varying timescales. In order to calculate erosion rates from the concentration of $^{10}Be_m$, $^{210}Pb_{ex}$, and $^{137}Cs$ while still retaining the ability to compare the activity of each isotope in the same sample, two complicating factors must be understood: how nuclide concentration in affected by sediment grain size, and how nuclide activity changes over time due to erosion.

Due to the grain size requirements of $^{10}Be_i$ analysis, all isotopes must be measured on the medium sand fraction of fluvial sediment. The relative dearth of field-based research detailing the behavior of fallout radionuclides across sediment grains of varying size and mineralogy presents a challenge in correcting grain size bias in nuclide concentration. Laboratory and limited field evidence clearly indicates that fallout radionuclides preferentially adsorb to smaller grains, and equations have been suggested to correct for grain size [*He and* Walling, 1996; Willenbring *and von Blanckenburg*, 2010], however, these would likely benefit from additional field testing and information regarding dependence on mineralogy.

A model describing the change expected in isotope activity over time due to erosion is prerequisite to calculating erosion rates from isotopic activity in fluvial sand.

Many models exist for calculating erosion rates from short-lived radionuclides using bulk sediment samples [e.g., *Matisoff and Whiting*, 2012], however, these must be adapted using grain size data to be applicable in this setting. As of yet, no studies have successfully calculated and independently verified erosion rates from $^{10}Be_m$, which, due to its long half-life, has a more complex soil depth profile than short-lived nuclides. *Willenbring and von Blanckenburg* [2010] present a set of equations and assumptions that would allow erosion rates to be derived from $^{10}Be_m$ concentration in a similar fashion to $^{10}Be_i$ derived erosion rates that, if independently verified, would greatly increase the utility of $^{10}Be_m$. While multiple isotopes measured on the same samples have shown to provide useful geomorphic information beyond what each isotope would provide alone, the ability to directly compare four independently derived erosion rates integrated over different time periods would more fully realize the potential of multiple isotopic systems.

# Comprehensive Bibliography


Akciz, S., B. C. Burchfiel, J. L. Crowley, Y. Jiyun, and C. Liangzhong (2008), Geometry, kinematics, and regional significance of the Chong Shan shear zone, Eastern Himalayan Syntaxis, Yunnan, China, *Geosphere*, *4*(1), 292.

Andermann, C., S. Bonnet, and R. Gloaguen (2011), Evaluation of precipitation data sets along the Himalayan front, *Geochemistry, Geophysics, Geosystems: G3*, *12*(7).

Balco, G., J. O. Stone, N. A. Lifton, and T. J. Dunai (2008), A complete and easily accessible means of calculating surface exposure ages or erosion rates from $^{10}$Be and $^{26}$Al measurements, *Quaternary Geochronology*, *3*, 174-195.

Bao, M. (2006), The Evolution of environmental policy and its impact in the People's Republic of China, *Conservation and Society*, *4*(1), 36-54.

Barg, E., D. Lal, M. J. Pavich, M. W. Caffee, and J. R. Southon (1997), Beryllium geochemistry in soils: Evaluation of $^{10}$Be/ $^{9}$Be ratios in authigenic minerals as a basis for age models, *Chemical Geology*, *140*(3-4), 237-258.

Belmont, P., J. Willenbring, S. Schottler, J. Marquard, K. Kumarasamy, and J. Hemmis (2014), Toward generalizable sediment fingerprinting with tracers that are conservative and nonconservative over sediment routing timescales, *J Soils Sediments*, *14*(8), 1479-1492.

Bierman, P. R., and E. Steig (1996), Estimating rates of denudation and sediment transport using cosmogenic isotope abundances in sediment, *Earth Surface Processes and Landforms*, *21*, 125-139.

Bierman, P. R., A. Albrecht, M. Bothner, E. Brown, T. Bullen, L. Gray, and L. Turpin (1998), Weathering, erosion and sedimentation, in *Isotope Tracers in Catchment Hydrology*, edited by C. Kendall and J. J. McDonnell, pp. 647-678, Elsevier.

Bierman, P. R., E. M. Clapp, K. K. Nichols, A. R. Gillespie, and M. Caffee (2001), Using cosmogenic nuclide measurements in sediments to understand background rates of erosion and sediment transport, in *Landscape Erosion and Evolution Modeling*, edited by R. S. Harmon and W. M. Doe, pp. 89-116, Kluwer, New York.

Bierman, P. R., and K. K. Nichols (2004), Rock to sediment - Slope to sea with $^{10}$Be - Rates of landscape change, *Annual review of Earth and Planetary Sciences*, *32*, 215-255.

Bierman, P. R., J. M. Reuter, M. Pavich, A. C. Gellis, M. W. Caffee, and J. Larsen (2005), Using cosmogenic nuclides to contrast rates of erosion and sediment yield

in a semi-arid, arroyo-dominated landscape, Rio Puerco Basin, New Mexico, *Earth Surface Processes and Landforms*, *30*(8), 935-953.

Binnie, S. A., W. M. Phillips, M. A. Summerfield, and L. K. Fifield (2006), Sediment mixing and basin-wide cosmogenic nuclide analysis in rapidly eroding mountainous environments, *Quaternary Geochronology 1*, 4-14.

Binnie, S. A., W. M. Phillips, M. A. Summerfield, and L. K. Fifield (2007), Tectonic uplift, threshold hillslopes, and denudation rates in a developing mountain range, *Geology*, *35*(8), 743.

Brown, E. T., D. L. Bourles, F. Colin, G. M. Raisbeck, F. Yiou, and S. Desgarceaux (1995a), Evidence for muon-induced production of $^{10}$Be in near surface rocks from the Congo, *Geophysical Research Letters*, *22*(6), 703-706.

Brown, E. T., R. F. Stallard, M. C. Larsen, G. M. Raisbeck, and F. Yiou (1995b), Denudation rates determined from the accumulation of *in situ*-produced $^{10}$Be in the Luquillo experimental forest, Puerto Rico, *Earth and Planetary Science Letters*, *129*, 193-202.

Brown, E. T., R. F. Stallard, M. C. Larsen, D. L. Bourles, G. M. Raisbeck, and F. Yiou (1998), Determination of predevelopment denudation rates of an agricultural watershed (Cayaguas River, Puerto Rico) using *in-situ*-produced $^{10}$Be in river-borne quartz, *Earth and Planetary Science Letters*, *160*(3-4), 723-728.

Brown, L. (1987), $^{10}$Be: Recent applications in Earth sciences, *Philosophical Transactions of the Royal Society of London*, *A 323*, 75-86.

Brown, L., M. Pavich, R. E. Hickman, J. Klein, and R. Middleton (1988), Erosion of the eastern United States observed with $^{10}$Be, *Earth Surface Processes and Landforms*, *13*, 441-457.

Burg, J.-P., P. Davy, P. Nievergelt, F. Oberli, D. Seward, Z. Diao, and M. Meier (1997), Exhumation during crustal folding in the Namche-Barwa syntaxis, *Terra Nova*, *9*(2), 53-56.

Chen, J., J. Chen, A. Liao, X. Cao, L. Chen, X. Chen, C. He, G. Han, S. Peng, M. Lu, W. Zhang, X. Tong, and J. Mills (2015), Global land cover mapping at 30m resolution: A POK-based operational approach, *ISPRS Journal of Photogrammetry and Remote Sensing*, *103*(0), 7-27.

Chmeleff, J., F. v. Blanckenburg, K. Kossert, and D. Jakob (2009), Determination of the $^{10}$Be half-life by multicollector ICP-MS and liquid scintillation counting, *Nuclear Instruments and Methods in Physics Research Section B: Beam Interactions with Materials and Atoms*, *268*(2), 192-199.

Clapp, E., P. R. Bierman, and M. Caffee (2002), Using $^{10}$Be and $^{26}$Al to determine sediment generation rates and identify sediment source areas in an arid region drainage basin, *Geomorphology*, *45*, 89-104.

Clapp, E. M., P. R. Bierman, A. P. Schick, J. Lekach, Y. Enzel, and M. Caffee (2000), Sediment yield exceeds sediment production in arid region drainage basins, *Geology*, *28*(11), 995-998.

Clark, M. K., M. A. House, L. H. Royden, K. X. Whipple, B. C. Burchfiel, X. Zhang, and W. Tang (2005), Late Cenozoic uplift of southeastern Tibet, *Geology*, *33*(6), 525-528.

Clark, M. K., L. H. Royden, K. X. Whipple, B. C. Burchfiel, X. Zhang, and W. Tang (2006), Use of a regional, relict landscape to measure vertical deformation of the eastern Tibetan Plateau, *Journal of Geophysical Research: Earth Surface*, *111*(F3), F03002.

Collins, A. L., D. E. Walling, and G. J. L. Leeks (1997), Source type ascription for fluvial suspended sediment based on a quantitative composite fingerprinting technique, *CATENA*, *29*(1), 1-27.

Corbett, L. B., N. E. Young, P. R. Bierman, J. P. Briner, T. A. Neumann, D. H. Rood, and J. A. Graly (2011), Paired bedrock and boulder $^{10}$Be concentrations resulting from early Holocene ice retreat near Jakobshavn Isfjord, western Greenland, *Quaternary Science Reviews*, *30*(13–14), 1739-1749.

Cyr, A. J., and D. E. Granger (2008), Dynamic equilibrium among erosion, river incision, and coastal uplift in the northern and central Apennines, Italy, *Geology*, *36*(2), 103-106.

DiBiase, R. A., K. X. Whipple, A. M. Heimsath, and W. B. Ouimet (2010), Landscape form and millennial erosion rates in the San Gabriel Mountains, CA, *Earth and Planetary Science Letters*, *289*, 134-144.

Dyer, F. J., and J. M. Olley (1999), The effects of grain abrasion and disaggregation on $^{137}$Cs concentrations in different size fractions of soils developed on three different rock types, *Catena*, *36*, 143-151.

Elvin, M. (2004), *The Retreat of the Elephants: An Environmental History of China*, Yale University Press.

Fan, H., J. Hu, and D. He (2013), Trends in precipitation over the low latitude highlands of Yunnan, China, *J. Geogr. Sci.*, *23*(6), 1107-1122.

Fan, Q., K. Tanaka, A. Sakaguchi, H. Kondo, N. Watanabe, and Y. Takahashi (2014), Factors controlling radiocesium distribution in river sediments: Field and

laboratory studies after the Fukushima Dai-ichi Nuclear Power Plant accident, *Applied Geochemistry*, *48*, 93-103.

Field, C. V., G. A. Schmidt, D. Koch, and C. Salyk (2006), Modeling production and climate-related impacts on $^{10}$Be concentration in ice cores, *Journal of Geophysical Research 111*, 13.

Fifield, L. K., R. J. Wasson, B. Pillans, and J. O. H. Stone (2010), The longevity of hillslope soil in SE and NW Australia, *Catena*, *81*, 32-42.

Flint, J. J. (1974), Stream gradient as a function of order, magnitude, and discharge, *Water Resources Research*, *10*(5), 969-973.

Foster, G. R., and R. E. Highfill (1983), Effect of terraces on soil loss: USLE P factor values for terraces, *Journal of Soil and Water Conservation*, *38*(1), 48-51.

Geology of Sanjiang Ministry of Geology and Mineral Resources (1986), Geological Map of Nujiang, Lancang, and Jinsha Rivers Area, Geological Publishing House, China Geological Map Printing House.

Godard, V., D. W. Burbank, D. L. Bourlès, B. Bookhagen, R. Braucher, and G. B. Fisher (2012), Impact of glacial erosion on $^{10}$Be concentrations in fluvial sediments of the Marsyandi catchment, central Nepal, *Journal of Geophysical Research: Earth Surface*, *117*(F3), F03013.

Graly, J. A., P. R. Bierman, L. J. Reusser, and M. J. Pavich (2010), Meteoric $^{10}$Be in soil profiles – a global meta-analysis, *Geochimica et Cosmochimica Acta*, *74*, 6814-6829.

Graly, J. A., L. J. Reusser, and P. R. Bierman (2011), Short and long-term delivery rates of meteoric $^{10}$Be to terrestrial soils, *Earth and Planetary Science Letters*, *302*(3–4), 329-336.

Granger, D. E., J. W. Kirchner, and R. Finkel (1996), Spatially averaged long-term erosion rates measured from *in situ*-produced cosmogenic nuclides in alluvial sediments, *Journal of Geology*, *104*(3), 249-257.

Granger, D. E., N. A. Lifton, and J. K. Willenbring (2013), A cosmic trip: 25 years of cosmogenic nuclides in geology, *Geological Society of America Bulletin*, *125*(9-10), 1379-1402.

He, Q., and D. E. Walling (1996), Interpreting particle size effects in the adsorption of $^{137}$Cs and unsupported $^{210}$Pb by mineral soils and sediments, *Journal of Environmental Radioactivity*, *30*(2), 117-137.

He, Q., and D. Walling (1997), The distribution of fallout $^{137}Cs$ and $^{210}Pb$ in undisturbed and cultivated soils, *Applied Radiation and Isotopes*, *48*(5), 677-690.

Heikkila, U., J. Beer, J. Jouzel, J. Feichter, and P. Kubik (2008), $^{10}Be$ measured in a GRIP snow pit and modeled using the ECHAM5-HAM general circulation model, *Geophysical Research Letters*, *35*(L05817), 1-4.

Heisinger, B., D. Lal, A. J. T. Jull, P. Kubik, S. Ivy-Ochs, K. Knie, and E. Nolte (2002a), Production of selected cosmogenic radionuclides by muons: 2. Capture of negative muons, *Earth and Planetary Science Letters*, *200*(3-4), 357-369.

Heisinger, B., D. Lal, A. J. T. Jull, P. Kubik, S. Ivy-Ochs, S. Neumaier, K. Knie, V. Lazarev, and E. Nolte (2002b), Production of selected cosmogenic radionuclides by muons - 1. Fast muons, *Earth and Planetary Science Letters*, *200*, 345-355.

Henck, A. C., D. R. Montgomery, K. W. Huntington, and C. Liang (2010), Monsoon control of effective discharge, Yunnan and Tibet, *Geology*, *38*(11), 975-978.

Henck, A. C., K. W. Huntington, J. O. Stone, D. R. Montgomery, and B. Hallet (2011), Spatial controls on erosion in the Three Rivers Region, southeastern Tibet and southwestern China, *Earth and Planetary Science Letters*, *303*(1-2), 71-83.

Hewawasam, T., F. von Blackenburg, M. Schaller, and P. Kubik (2003), Increase of human over natural erosion rates in tropical highlands constrained by cosmogenic nuclides, *Geology*, *31*(7), 597-600.

Hooke, R. L. (1994), On the efficacy of humans as geomorphic agents, *GSA Today*, *4*(9), 217,224-225.

Hooke, R. L. M.-D., Jose F. (2012), Land transformation by humans: A review, *GSA Today*, *22*(12), 4-10.

Hyde, W. F., B. Belcher, and J. Xu (2003), *China's forests: global lessons from market reforms*, Resources for the Future and CIFOR, Washington, DC.

Inbar, M., and C. A. Llerena (2000), Erosion processes in high mountain agricultural terraces in Peru, *Mountain Research and Development*, *20*(1), 72-79.

Jovanovic, S., A. Dlabac, and N. Mihaljevic (2010), ANGLE v2.1—New version of the computer code for semiconductor detector gamma-efficiency calculations, *Nuclear Instruments and Methods in Physics Research Section A: Accelerators, Spectrometers, Detectors and Associated Equipment*, *622*(2), 385-391.

Judson, S. (1968), Erosion of the land, or What's happening to our continents, *American Scientist*, *56*, 356-374.

Jull, A. J. T., E. M. Scott, and P. Bierman (2015), The CRONUS-Earth inter-comparison for cosmogenic isotope analysis, *Quaternary Geochronology*(0).

Jungers, M. C., P. R. Bierman, A. Matmon, K. Nichols, J. Larsen, and R. Finkel (2009), Tracing hillslope sediment production and transport with *in situ* and meteoric $^{10}$Be, *Journal of Geophysical Research*, *114*(F04020), 1-16.

Kaste, J. M., A. M. Heimsath, and B. C. Bostick (2007), Short-term soil mixing quantified with fallout radionuclides, *Geology*, *35*(3), 243-246.

Kirchner, J. W., R. C. Finkel, C. S. Riebe, D. E. Granger, J. L. Clayton, J. G. King, and W. F. Megahan (2001), Mountain erosion over 10 yr, 10 k.y., and 10 m.y. time scales, *Geology*, *29*(7), 591-594.

Kohl, C. P., and K. Nishiizumi (1992), Chemical isolation of quartz for measurement of *in-situ* -produced cosmogenic nuclides, *Geochimica et Cosmochimica Acta*, *56*, 3583-3587.

Koiter, A. J., P. N. Owens, E. L. Petticrew, and D. A. Lobb (2013), The behavioural characteristics of sediment properties and their implications for sediment fingerprinting as an approach for identifying sediment sources in river basins, *Earth-Science Reviews*, *125*(0), 24-42.

Lal, D., and B. Peters (1962), Cosmic-ray produced isotopes and their application to problems in geophysics, in *Progress in elementary particle and cosmic ray physics*, edited by J. G. Wilson and S. A. Wouthysen, pp. 1-74, Wiley, New York.

Lal, D., and B. Peters (1967), Cosmic ray produced radioactivity on the earth, in *Handbuch der Physik*, edited by K. Sitte, pp. 551-612, Springer-Verlag, New York.

Lal, D. (1988), *In situ*-produced cosmogenic isotopes in terrestrial rocks, *Annual Reviews of Earth and Planetary Science*, *16*, 355-388.

Lal, D. (1991), Cosmic ray labeling of erosion surfaces: *In situ* nuclide production rates and erosion models, *Earth and Planetary Science Letters*, *104*(2-4), 424-439.

Lauer, J. W., and J. Willenbring (2010), Steady state reach-scale theory for radioactive tracer concentration in a simple channel/floodplain system, *Journal of Geophysical Research: Earth Surface*, *115*(F4), F04018.

Liu-Zeng, J., P. Tapponnier, Y. Gaudemer, and L. Ding (2008), Quantifying landscape differences across the Tibetan plateau: Implications for topographic relief evolution, *Journal of Geophysical Research: Earth Surface*, *113*(F4), F04018.

Lu, X., and D. Higgitt (2000), Estimating erosion rates on sloping agricultural land in the Yangtze Three Gorges, China, from caesium-137 measurements, *Catena*, *39*(1), 33-51.

Mabit, L., M. Benmansour, and D. E. Walling (2008), Comparative advantages and limitations of the fallout radionuclides $^{137}Cs$, $^{210}Pb_{ex}$ and $^{7}Be$ for assessing soil erosion and sedimentation, *Journal of Environmental Radioactivity*, *99*, 1799-1807.

Mabit, L., M. Benmansour, J. Abril, D. Walling, K. Meusburger, A. Iurian, C. Bernard, S. Tarján, P. Owens, and W. Blake (2014), Fallout $^{210}Pb$ as a soil and sediment tracer in catchment sediment budget investigations: A review, *Earth-Science Reviews*, *138*, 335-351.

Magee, D. (2006), Powershed Politics: Yunnan Hydropower under Great Western Development, *The China Quarterly*, *185*, 23-41.

Masarik, J., and J. Beer (1999), Simulation of particle fluxes and cosmogenic nuclide production in the Earth's atmosphere, *Journal of Geophysical Research*, *104*(D10), 12099-12111.

Matisoff, G., and P. Whiting (2012), Measuring Soil Erosion Rates Using Natural ($^{7}Be$, $^{210}Pb$) and Anthropogenic ($^{137}Cs$, $^{239,240}Pu$) Radionuclides, in *Handbook of Environmental Isotope Geochemistry*, edited by M. Baskaran, pp. 487-519, Springer Berlin Heidelberg.

Matmon, A., P. R. Bierman, J. Larsen, S. Southworth, M. Pavich, and M. Caffee (2003a), Temporally and spatially uniform rates of erosion in the southern Appalachian Great Smoky Mountains, *Geology*, *31*(2), 155–158.

Matmon, A. S., P. Bierman, J. Larsen, S. Southworth, M. Pavich, R. Finkel, and M. Caffee (2003b), Erosion of an ancient mountain range, the Great Smoky Mountains, North Carolina and Tennessee, *American Journal of Science*, *303*, 817-855.

McKean, J. A., W. E. Dietrich, R. C. Finkel, J. R. Southon, and M. W. Caffee (1993), Quantification of soil production and downslope creep rates from cosmogenic $^{10}Be$ accumulations on a hillslope profile, *Geology*, *21*(4), 343-346.

Miller, S. R., P. B. Sak, E. Kirby, and P. R. Bierman (2013), Neogene rejuvenation of central Appalachian topography: Evidence for differential rock uplift from stream profiles and erosion rates, *Earth and Planetary Science Letters*, *369–370*(0), 1-12.

Monaghan, M. C., S. Krishnaswami, and K. K. Turekian (1986), The global-average production rate of $^{10}Be$, *Earth and Planetary Science Letters*, *76*, 279-287.

Montgomery, D. R., and M. T. Brandon (2002), Topographic controls on erosion rates in tectonically active mountain ranges, *Earth and Planetary Science Letters*, *201*(3-4), 481-489.

NASA LP-DAAC (2012), ASTER GDEM, edited by NASA Land Processes Distributed Active Archive Center (LP DAAC), LP DAAC.

Nichols, K. K., P. R. Bierman, M. Caffee, R. Finkel, and J. Larsen (2005a), Cosmogenically enabled sediment budgeting, *Geology*, *33*(2), 133-136.

Nichols, K. k., P. r. Bierman, R. Finkel, and J. Larsen (2005b), Long-Term (10 to 20 kyr) Sediment Generation Rates for the Upper Rio Chagres Basin Based on Cosmogenic $^{10}$Be, in *The Rio Chagres: A Multidisciplinary Profile of a Tropical Watershed*, edited by R. S. Harmon, Kluwer Academic Publishers.

Nichols, K. K., P. R. Bierman, and D. H. Rood (2014), $^{10}$Be constrains the sediment sources and sediment yields to the Great Barrier Reef from the tropical Barron River catchment, Queensland, Australia, *Geomorphology*, *224*(0), 102-110.

Niemi, N. A., M. Oskin, D. W. Burbank, A. J. M. Heimsath, and E. J. Gabet (2005), Effects of bedrock landslides on cosmogenically determined erosion rates, *Earth and Planetary Science Letters*, *237*(3), 480-498.

Nishiizumi, K., M. Imamura, M. W. Caffee, J. R. Southon, R. C. Finkel, and J. McAninch (2007), Absolute calibration of $^{10}$Be AMS standards, *Nuclear Inst. and Methods in Physics Research, B*, *258*(2), 403-413.

NRC (2012), New Research Opportunities in the Earth Sciences, edited, National Academy Press, Washington, DC.

Nyffeler, U. P., Y.-H. Li, and P. H. Santschi (1984), A kinetic approach to describe trace-element distribution between particles and solution in natural aquatic systems, *Geochimica et Cosmochimica Acta*, *48*(7), 1513-1522.

O'Farrell, C. R., A. M. Heimsath, and J. M. Kaste (2007), Quantifying hillslope erosion rates and processes for a coastal California landscape over varying timescales, *Earth Surface Processes and Landforms*, *32*(4), 544-560.

Ouimet, W., D. Dethier, P. Bierman, C. Wyshnytzky, N. Shea, and D. H. Rood (2015), Spatial and temporal variations in meteoric $^{10}$Be inventories and long-term deposition rates, Colorado Front Range, *Quaternary Science Reviews*, *109*(0), 1-12.

Ouimet, W. B., K. X. Whipple, and D. E. Granger (2009), Beyond threshold hillslopes: Channel adjustment to base-level fall in tectonically active mountain ranges, *Geology*, *37*(7), 579-582.

Parsons, A. J., and I. D. L. Foster (2011), What can we learn about soil erosion from the use of $^{137}$Cs?, *Earth-Science Reviews*, *108*(1), 101-113.

Pavich, M., L. Brown, J. N. Valette-Silver, J. Klein, and R. Middleton (1985), $^{10}$Be analysis of a Quaternary weathering profile in the Virginia Piedmont, *Geology*, *13*, 39-41.

Pavich, M. J., L. Brown, J. W. Harden, J. Klein, and R. Middleton (1986), $^{10}$Be distribution in soils from Merced River terraces, California, *Geochimica et Cosmochimica Acta*, *50*(8), 1727-1735.

Perg, L. A., R. S. Anderson, and R. C. Finkel (2001), Use of a new $^{10}$Be and $^{26}$Al inventory method to date marine terraces, Santa Cruz, California, USA, *Geology*, *29*(10), 879-882.

Portenga, E. W., and P. R. Bierman (2011), Understanding Earth's eroding surface with $^{10}$Be, *GSA Today*, *21*(8), 4-10.

Preiss, N., M.-A. Mélières, and M. Pourchet (1996), A compilation of data on lead-210 concentration in surface air and fluxes at the air-surface and water-sediment interfaces, *Journal of Geophysical Research: Atmospheres*, *101*(D22), 28847-28862.

Quine, T., D. Walling, X. Zhang, and Y. Wang (1992), Investigation of soil erosion on terraced fields near Yanting, Sichuan Province, China, using caesium-137, *International Association of Hydrological Sciences Publication*(209), 155-168.

Reusser, L., P. Bierman, and D. Rood (2015), Quantifying human impacts on rates of erosion and sediment transport at a landscape scale, *Geology*.

Reusser, L. J., and P. R. Bierman (2010), Using meteoric $^{10}$Be to track fluvial sand through the Waipaoa River basin, New Zealand, *Geology*, *38*(1), 47-50.

Ritchie, J. C., and J. R. McHenry (1990), Application of Radioactive Fallout Cesium-137 for Measuring Soil Erosion and Sediment Accumulation Rates and Patterns: A Review, *Journal of Environmental Quality*(2), 215-233.

Savi, S., K. Norton, V. Picotti, F. Brardinoni, N. Akçar, P. W. Kubik, R. Delunel, and F. Schlunegger (2014), Effects of sediment mixing on $^{10}$Be concentrations in the Zielbach catchment, central-eastern Italian Alps, *Quaternary Geochronology*, *19*(0), 148-162.

Schaller, M., F. von Blanckenburg, N. Hovius, and P. W. Kubik (2001), Large-scale erosion rates from *in situ*-produced cosmogenic nuclides in European river sediments, *Earth and Planetary Science Letters*, *v. 188*, 441-458.

Schmidt, A. H., D. R. Montgomery, K. W. Huntington, and C. Liang (2011), The question of communist land degradation: new evidence from local erosion and basin-wide sediment yield in Southwest China and Southeast Tibet, *Annals of the Association of American Geographers*, *101*(3), 477-496.

Shen, C., J. Beer, P. W. Kubik, M. Suter, M. Borkovec, and T. S. Liu (2004), Grain size distribution, $^{10}$Be content and magnetic susceptibility of micrometer–nanometer loess materials, *Nuclear Instruments and Methods in Physics Research Section B: Beam Interactions with Materials and Atoms*, *223–224*(0), 613-617.

Sidle, R. C., A. D. Ziegler, J. N. Negishi, A. R. Nik, R. Siew, and F. Turkelboom (2006), Erosion processes in steep terrain—Truths, myths, and uncertainties related to forest management in Southeast Asia, *Forest Ecology and Management*, *224*(1–2), 199-225.

Smith, H. G., and W. H. Blake (2014), Sediment fingerprinting in agricultural catchments: A critical re-examination of source discrimination and data corrections, *Geomorphology*, *204*(0), 177-191.

Stone, J. (1998), A rapid fusion method for separation of beryllium-10 from soils and silicates, *Geochimica et Cosmochimica Acta*, *62*(3), 555-561.

Stout, J. C., P. Belmont, S. P. Schottler, and J. K. Willenbring (2014), Identifying sediment sources and sinks in the Root River, Southeastern Minnesota, *Annals of the Association of American Geographers*, *104*(1), 20-39.

Trac, C., S. Harrell, T. Hinckley, and A. Henck (2007), Reforestation programs in Southwest China: Reported success, observed failure, and the reasons why, *J. Mt. Sci.*, *4*(4), 275-292.

Trac, C. J., A. C. H. Schmidt, S. Harrell, and T. M. Hinckley (2013), Is the Returning Farmland to Forest Program a Success? Three case studies from Sichuan, *Environmental Practice*, *15*(3), 350-366.

Trimble, S. W. (1977), The fallacy of stream equilibrium in contemporary denudation studies, *American Journal of Science*, *277*, 876-887.

Urgenson, L. S., R. K. Hagmann, A. C. Henck, S. Harrell, T. M. Hinckley, S. J. Shepler, B. L. Grub, and P. M. Chi (2010), Social-ecological dynamics of a forested watershed in SW China, *Society And Ecology [online]*, *15*(5), 2.

Vanacker, V., F. von Blanckenburg, G. Govers, A. Molina, J. Poesen, J. Deckers, and P. Kubik (2007), Restoring dense vegetation can slow mountain erosion to near natural benchmark levels, *Geology*, *35*(4), 303-306.

Vanacker, V., F. von Blanckenburg, G. Govers, A. Molina, B. Campforts, and P. W. Kubik (2015), Transient river response, captured by channel steepness and its concavity, *Geomorphology*, *228*(0), 234-243.

von Blanckenburg, F. (2005), The control mechanisms of erosion and weathering at basin scale from cosmogenic nuclides in river sediment, *Earth and Planetary Science Letters*, *237*(3-4), 462-479.

von Blanckenburg, F., J. Bouchez, and H. Wittmann (2012), Earth surface erosion and weathering from the $^{10}$Be (meteoric)/$^{9}$Be ratio, *Earth and Planetary Science Letters*, *351–352*(0), 295-305.

Wallbrink, P. J., and A. S. Murray (1993), Use of fallout radionuclides as indicators of erosion processes, *Hydrological Processes*, *7*, 297-304.

Walling, D. E. (1983), The sediment delivery problem, *Journal of Hydrology*, *65*(1-3), 209-237.

Walling, D. E., and J. C. Woodward (1992), Use of radiometric fingerprints to derive information on suspended sediment sources, *Erosion and Sediment Transport Monitoring Programmes in River Basins*(210), 153-163.

Walling, D. E. (1999), Linking land use, erosion and sediment yields in river basins, *Hydrobiologia*, *410*, 223-240.

Walter, R. C., and D. J. Merritts (2008), Natural Streams and the Legacy of Water-Powered Mills, *Science*, *319*, 299-304.

West, N., E. Kirby, P. Bierman, R. Slingerland, L. Ma, D. Rood, and S. Brantley (2013), Regolith production and transport at the Susquehanna Shale Hills Critical Zone Observatory, Part 2: Insights from meteoric $^{10}$Be, *Journal of Geophysical Research: Earth Surface*, *118*(3), 1877-1896.

West, N., E. Kirby, P. Bierman, and B. A. Clarke (2014), Aspect-dependent variations in regolith creep revealed by meteoric $^{10}$Be, *Geology*, *42*(6), 507-510.

Whiting, P. J., E. C. Bonniwell, and G. Matisoff (2001), Depth and areal extent of sheet and rill erosion based on radionuclides in soils and suspended sediment, *Geology*, *29*(12), 1131-1134.

Wilkinson, B. H., and B. J. McElroy (2007), The impact of humans on continental erosion and sedimentation, *Geological Society of America Bulletin*, *119*(1), 140-156.

Willenbring, J. K., and F. von Blanckenburg (2010), Meteoric cosmogenic Beryllium-10 adsorbed to river sediment and soil: Applications for Earth-surface dynamics, *Earth-Science Reviews*, *98*, 105-122.

Willenbring, J. K., N. M. Gasparini, B. T. Crosby, and G. Brocard (2013), What does a mean mean? The temporal evolution of detrital cosmogenic denudation rates in a transient landscape, *Geology*, *41*(12), 1215-1218.

Wittmann, H., F. von Blanckenburg, T. Kruesmann, K. P. Norton, and P. W. Kubik (2007), Relation between rock uplift and denudation from cosmogenic nuclides in river sediment in the Central Alps of Switzerland, *Journal of Geophysical Research*, *112*(F04010).

Wittmann, H., F. von Blanckenburg, J. Bouchez, N. Dannhaus, R. Naumann, M. Christl, and J. Gaillardet (2012), The dependence of meteoric $^{10}$Be concentrations on particle size in Amazon River bed sediment and the extraction of reactive $^{10}$Be/$^{9}$Be ratios, *Chemical Geology*, *318–319*(0), 126-138.

Wobus, C., K. X. Whipple, E. Kirby, N. Snyder, J. Johnson, K. Spyropolou, B. Crosby, and D. Sheehan (2006), Tectonics from topography: Procedures, promise and pitfalls, *Tectonics, climate, and landscape evolution: Geological Society of America Special Paper*, *398*, 55–74.

Wyshnytzky, C. E., W. B. Ouimet, J. McCarthy, D. P. Dethier, R. R. Shroba, P. R. Bierman, and D. H. Rood (2015), Meteoric $^{10}$Be, clay, and extractable iron depth profiles in the Colorado Front Range: Implications for understanding soil mixing and erosion, *CATENA*, *127*, 32-45.

Xu, S., A. B. Dougans, S. P. H. T. Freeman, C. Schnabel, and K. M. Wilcken (2010), Improved $^{10B}$e and $^{26}$Al-AMS with a 5MV spectrometer, *Nuclear Instruments and Methods in Physics Research Section B: Beam Interactions with Materials and Atoms*, *268*(7–8), 736-738.

Xu, S., S. P. H. T. Freeman, D. H. Rood, and R. P. Shanks (2015), Decadal $^{10}$Be, $^{26}$Al and $^{36}$Cl QA measurements on the SUERC 5 MV accelerator mass spectrometer, *Nuclear Instruments and Methods in Physics Research Section B: Beam Interactions with Materials and Atoms*(0).

Yang, S.-l., Q.-y. Zhao, and I. M. Belkin (2002), Temporal variation in the sediment load of the Yangtze river and the influences of human activities, *Journal of Hydrology*, *263*(1–4), 56-71.

Yanites, B. J., G. E. Tucker, and R. S. Anderson (2009), Numerical and analytical models of cosmogenic radionuclide dynamics in landslide‐dominated drainage basins, *Journal of Geophysical Research: Earth Surface (2003‐2012)*, *114*(F1).

Yatagai, A., K. Kamiguchi, O. Arakawa, A. Hamada, N. Yasutomi, and A. Kitoh (2012), APHRODITE: Constructing a Long-Term Daily Gridded Precipitation Dataset for Asia Based on a Dense Network of Rain Gauges, *Bulletin of the American Meteorological Society*, *93*(9), 1401-1415.

You, C.-F., T. Lee, and Y.-H. Li (1989), The partition of Be between soil and water, *Chemical Geology*, *77*(2), 105-118.

# Appendix A: Supporting Information for the *Journal of Geophysical Research: Earth Surface* Manuscript

*Journal of Geophysical Research: Earth Surface*

Supporting Information for

**Using long- and short-lived sediment-associated isotopes to track erosion and sediment movement through rivers in Yunnan, SW China**

Thomas B. Neilson[1], Paul Bierman[1], Amanda H. Schmidt[2], Dylan Rood[3], Will Ouimet[4], Veronica Sosa Gonzalez[5]

[1]Department of Geology, University of Vermont, 180 Colchester Ave., Burlington, VT 05405, [2]Geology Department, Oberlin College, 403 Carnegie Building, 52 W. Lorain St., Oberlin, OH 44074, [3]Department of Earth Science and Engineering, Imperial College London, South Kensington Campus, London SW7 2AZ, UK, [4]Department of Geography and Center for Integrative Geosciences, University of Connecticut, Storrs, CT, 06269, [5]Rubenstein School of Environment and Natural Resources, University of Vermont, Burlington, VT 05405

**Contents of this file**



**Additional Supporting Information (Files uploaded separately)**

Captions for Tables S1, S2, and S4.

**Introduction**

Here we include supporting information regarding data reduction methods, tables of the values used to interpret erosion rates and erosion indices, a table summarizing the results for each sample, and figures and tables supporting statements made in the text. All samples presented here are included in the main text and were collected in May and June of 2013.

**Text S1.**

1. Additional Methods

1.1 $^{10}Be_i$ extraction and measurement

Prior to quartz separation, magnetic grains were separated from samples using a magnetic separator. If acid-resistant mafic grains were present during quartz separation, they were removed using heavy density liquid separation. After initial purity testing of separated quartz by ICP-OES, samples with high cation concentrations were re-etched to increase purity, following established methods [*Kohl and Nishiizumi*, 1992]. We extracted Be from purified quartz separates in 7 batches of 10 samples, with the addition of one CRONUS N process replicate *Jull et al.* [2015] and one process blank per batch. Each sample was processed with between 218.5 – 250.8 μg of $^{9}Be$ from in-house made beryl carrier. Two different carrier batches were used between the 7 batches. After measurement, all samples were corrected by the average $^{10}Be/^{9}Be$ ratio of the 7 process blanks included, $2.64 \pm 0.98 \times 10^{-15}$ (1 SD), which is ~1% of the mean sample ratio. Measured blank-corrected sample ratios range from $0.367 – 13.8 \times 10^{-13}$, and the mean AMS precision of blank-corrected ratios is 3.3%.

The CRONUS N process replicates run in each batch generally agree with results reported by [*Jull et al.*, 2015], and have a coefficient of variation of 6.3 %. The mean and median concentrations of the CRONUS N standards were 2.25 and 2.23 $\times 10^5$ atoms/g respectively, slightly above previously reported mean and median concentrations of $2.17 \times 10^5$ atoms/g (for both) [*Jull et al.*, 2015].

1.2 $^{10}Be_m$ extraction and measurement

Sieved, dried, and otherwise un-altered samples were powdered using a SPEX Shatterbox for ~60 – 120 seconds. Be was extracted using from 319.5 – 330.9 μg of $^{9}Be$ from two different in-house made beryl carriers. Samples were processed in 6 batches of 15 samples, with one process blank per batch. During measurement, several samples performed poorly during in the AMS, and those samples with currents < ~25% of the standard current were re-processed and re-measured. Sample ratios were blank-corrected using the mean blank value of $2.28 \pm 2.31 \times 10^{-14}$ (n = 6, 1 SD), which is ~2% of the mean sample ratio. Blank-correct sample ratios range from $0.126 – 15.9 \times 10^{-12}$, and mean AMS precision of blank corrected ratios is 4%.

Normalized $^{10}Be_i$

Kruskal-Wallis Test

| $\chi^2$ | DF: | p= |
|---|---|---|
| 23.5 | 2 | <0.0001 |

All Pairs Steel-Dwass Test

| | | |
|---|---|---|
| 35 | 0.0052 | 0.98 |
| 49 | <0.0001 | |
| 11 | | |

A B A

Normalized $^{10}Be_m$

Kruskal-Wallis Test

| $\chi^2$ | DF: | p= |
|---|---|---|
| 36.9 | 2 | <0.0001 |

All Pairs Steel-Dwass Test

| | | |
|---|---|---|
| 35 | <0.0001 | 0.0004 |
| 49 | 0.0004 | |
| 11 | | |

A B C

$^{210}Pb_{ex}$

Kruskal-Wallis Test

| χ2 | DF: | p= |
|---|---|---|
| 8.5 | 2 | 0.0145 |

All Pairs Steel-Dwass Test

| | | |
|---|---|---|
| 35 | 0.9666 | 0.0437 |
| 49 | 0.0227 | |
| 11 | | |

A A B

**Figure S1.** Shows the results of statistical analysis comparing the variance of samples for each studied basin. Results of the Kruskal-Wallis test are shown for each isotope above a table showing the results of a Steel-Dwass all pairs test, a post-hoc test showing the results of comparisons between each pair. The Steel-Dwass test differentiates the basins into similar and dissimilar groups, denotes by the letter assigned at bottom of each matrix (A, B, or C). Groups coming from the same distribution share a common letter, while groups from statistically separable distributions are assigned different letters.

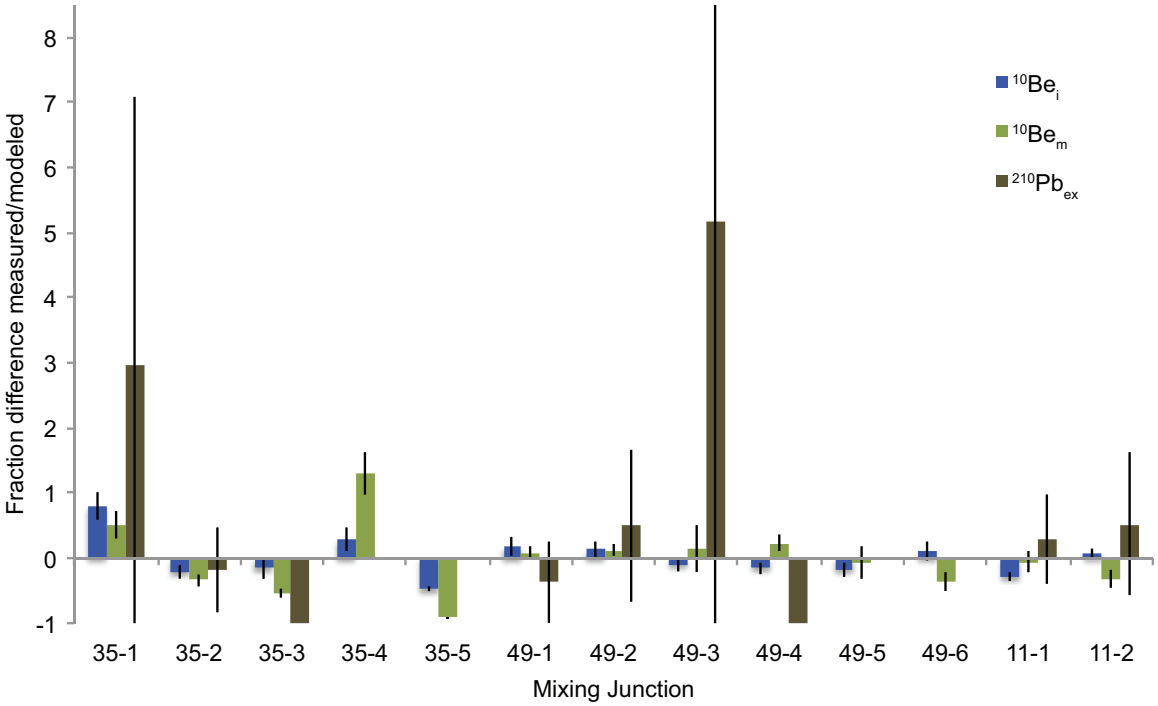


**Figure S2**. A bar chart showing the fraction of the measured to modeled concentration of $^{10}Be_i$, $^{10}Be_m$, and $^{210}Pb_{ex}$ at each junction. Error bars show 2 SD, and with the exception of $^{210}Pb_{ex}$, samples where the error bar intersects (or nearly intersects) the x-axis at zero are considered well mixed. Junctions with no $^{210}Pb_{ex}$ bar did not have measureable $^{210}Pb_{ex}$ in one of the upstream samples, and those where the $^{210}Pb_{ex}$ bar extends to -1 did not contain measurable $^{210}Pb_{ex}$ below the junction.

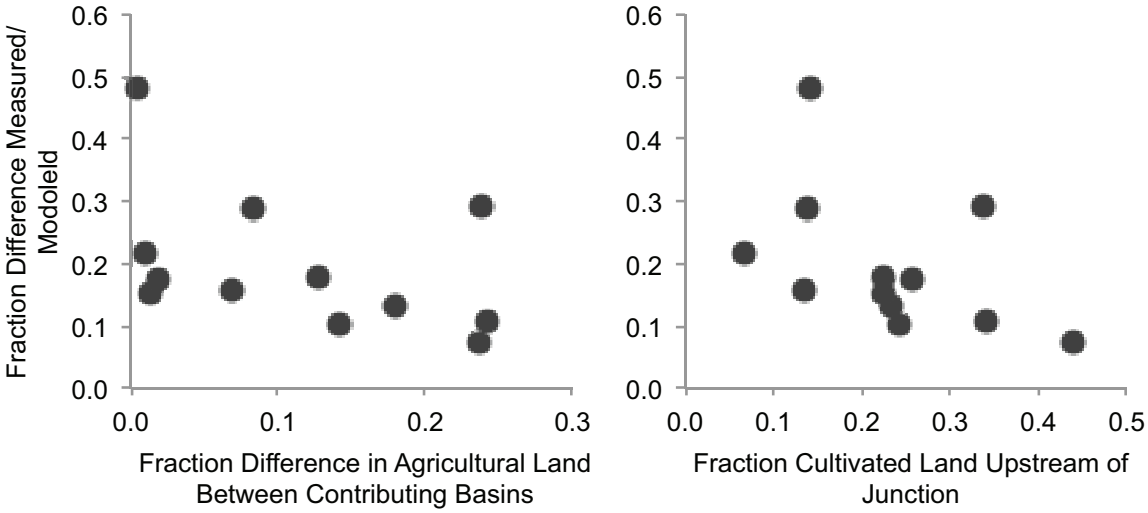


**Figure S3**. Scatter plots showing the fraction difference from measured to modeled concentrations at each junction as a function of the fraction of total agricultural land upstream of the junction and the fraction difference in agricultural land between the basins contributing to the mixing model. No obvious relationships exist in either plot. The junction influenced by the dam (35.1) is excluded from both analyses.

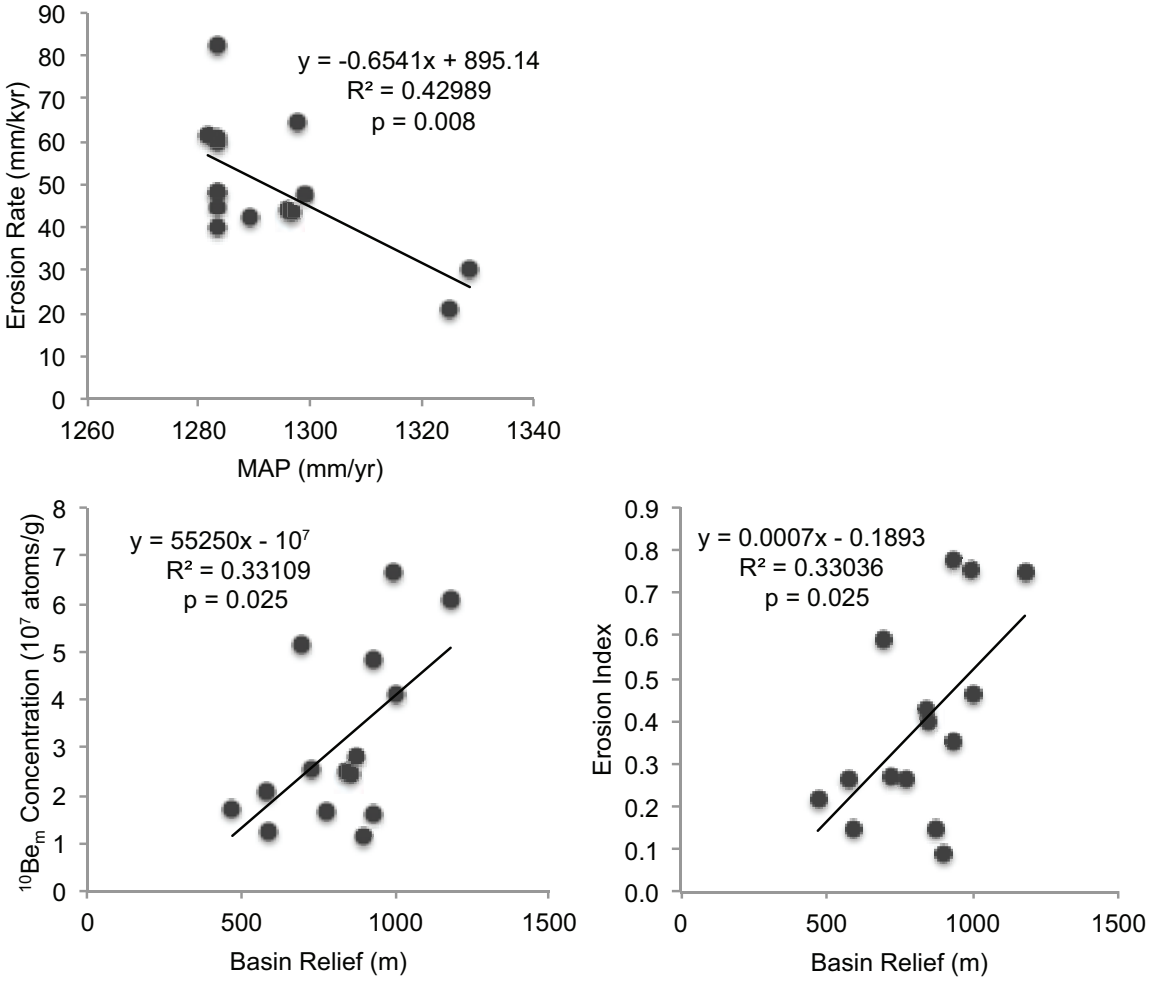


**Figure S4**. Scatter plots showing the relationship between three measures of long-term erosion (erosion rate, erosion index, and $^{10}Be_m$ concentration) plotted against basin relief and mean annual precipitation for basin 11. The results of bivariate linear regression analysis of shown.

**Table S1.** Data for all samples as entered into CRONUS-Earth online calculator[a]

| Sample name | Mean Latitude | Mean Longitude | Effective Elevation (m) | Elv/pressure flag | Thickness (cm) | Density (g cm$^{-3}$) | Shielding Correction | $^{10}$Be (atoms g$^{-1}$) | +/- (atoms g$^{-1}$) | $^{10}$Be Standard | $^{26}$Al (atoms g$^{-1}$) | +/- (atoms g$^{-1}$) | $^{26}$Al Standard |
|---|---|---|---|---|---|---|---|---|---|---|---|---|---|
| CH001 | 27.115 | 99.356 | 2956 | std | 0.1 | 2.7 | 1 | 1.92E-05 | 7.42E-07 | NIST_27900 | 0 | 0 | KNSTD |
| CH003 | 27.049 | 99.384 | 3115 | std | 0.1 | 2.7 | 1 | 5.37E-05 | 1.10E-04 | NIST_27900 | 0 | 0 | KNSTD |
| CH004 | 27.055 | 99.329 | 2988 | std | 0.1 | 2.7 | 1 | 1.49E-05 | 8.33E-07 | NIST_27900 | 0 | 0 | KNSTD |
| CH005 | 27.057 | 99.372 | 2975 | std | 0.1 | 2.7 | 1 | 2.60E-05 | 7.95E-07 | NIST_27900 | 0 | 0 | KNSTD |
| CH009 | 27.056 | 99.359 | 2962 | std | 0.1 | 2.7 | 1 | 2.78E-05 | 1.04E-04 | NIST_27900 | 0 | 0 | KNSTD |
| CH010 | 27.061 | 99.375 | 3059 | std | 0.1 | 2.7 | 1 | 4.84E-05 | 9.32E-07 | NIST_27900 | 0 | 0 | KNSTD |
| CH011 | 27.069 | 99.322 | 2961 | std | 0.1 | 2.7 | 1 | 8.58E-04 | 4.86E-06 | NIST_27900 | 0 | 0 | KNSTD |
| CH012 | 27.062 | 99.351 | 2942 | std | 0.1 | 2.7 | 1 | 1.47E-05 | 4.24E-07 | NIST_27900 | 0 | 0 | KNSTD |
| CH013 | 27.175 | 99.407 | 3297 | std | 0.1 | 2.7 | 1 | 1.67E-06 | 2.15E-04 | NIST_27900 | 0 | 0 | KNSTD |
| CH016 | 27.163 | 99.409 | 3268 | std | 0.1 | 2.7 | 1 | 1.62E-06 | 2.10E-04 | NIST_27900 | 0 | 0 | KNSTD |
| CH017 | 27.127 | 99.431 | 3195 | std | 0.1 | 2.7 | 1 | 5.72E-05 | 1.75E-04 | NIST_27900 | 0 | 0 | KNSTD |
| CH020 | 27.153 | 99.422 | 3224 | std | 0.1 | 2.7 | 1 | 6.63E-05 | 1.05E-04 | NIST_27900 | 0 | 0 | KNSTD |
| CH021 | 27.077 | 99.353 | 2895 | std | 0.1 | 2.7 | 1 | 3.40E-05 | 7.36E-07 | NIST_27900 | 0 | 0 | KNSTD |
| CH023 | 27.115 | 99.377 | 2968 | std | 0.1 | 2.7 | 1 | 9.47E-05 | 1.16E-04 | NIST_27900 | 0 | 0 | KNSTD |
| CH024 | 27.141 | 99.401 | 3045 | std | 0.1 | 2.7 | 1 | 1.03E-06 | 1.24E-04 | NIST_27900 | 0 | 0 | KNSTD |
| CH031 | 24.192 | 100.74 | 1818 | std | 0.1 | 2.7 | 1 | 7.21E-04 | 2.95E-03 | NIST_27900 | 0 | 0 | KNSTD |
| CH032 | 24.115 | 100.74 | 1841 | std | 0.1 | 2.7 | 1 | 4.95E-04 | 2.41E-03 | NIST_27900 | 0 | 0 | KNSTD |
| CH033 | 24.184 | 100.75 | 1814 | std | 0.1 | 2.7 | 1 | 7.22E-04 | 2.66E-03 | NIST_27900 | 0 | 0 | KNSTD |
| CH034 | 24.184 | 100.75 | 1814 | std | 0.1 | 2.7 | 1 | 5.85E-04 | 2.35E-03 | NIST_27900 | 0 | 0 | KNSTD |
| CH035 | 24.261 | 100.81 | 1867 | std | 0.1 | 2.7 | 1 | 8.05E-04 | 2.53E-03 | NIST_27900 | 0 | 0 | KNSTD |
| CH036 | 24.247 | 100.79 | 1845 | std | 0.1 | 2.7 | 1 | 5.77E-04 | 3.11E-03 | NIST_27900 | 0 | 0 | KNSTD |
| CH037 | 24.082 | 100.84 | 1415 | std | 0.1 | 2.7 | 1 | 9.33E-04 | 3.75E-03 | NIST_27900 | 0 | 0 | KNSTD |
| CH039 | 24.177 | 100.81 | 1729 | std | 0.1 | 2.7 | 1 | 8.14E-04 | 3.01E-03 | NIST_27900 | 0 | 0 | KNSTD |
| CH041 | 24.106 | 100.81 | 1682 | std | 0.1 | 2.7 | 1 | 5.30E-04 | 2.26E-03 | NIST_27900 | 0 | 0 | KNSTD |
| CH042 | 23.875 | 100.6 | 1836 | std | 0.1 | 2.7 | 1 | 1.63E-05 | 3.99E-03 | NIST_27900 | 0 | 0 | KNSTD |
| CH043 | 23.676 | 100.6 | 1762 | std | 0.1 | 2.7 | 1 | 1.60E-05 | 3.70E-03 | NIST_27900 | 0 | 0 | KNSTD |
| CH044 | 23.978 | 100.8 | 1657 | std | 0.1 | 2.7 | 1 | 8.06E-04 | 2.66E-03 | NIST_27900 | 0 | 0 | KNSTD |
| CH045 | 23.992 | 100.85 | 1645 | std | 0.1 | 2.7 | 1 | 6.09E-04 | 2.96E-03 | NIST_27900 | 0 | 0 | KNSTD |
| CH046 | 23.898 | 100.93 | 1654 | std | 0.1 | 2.7 | 1 | 8.37E-04 | 3.36E-03 | NIST_27900 | 0 | 0 | KNSTD |
| CH047 | 23.894 | 100.96 | 1735 | std | 0.1 | 2.7 | 1 | 7.89E-04 | 2.98E-03 | NIST_27900 | 0 | 0 | KNSTD |
| CH048 | 23.852 | 100.97 | 1864 | std | 0.1 | 2.7 | 1 | 1.07E-05 | 3.06E-03 | NIST_27900 | 0 | 0 | KNSTD |
| CH049 | 23.877 | 100.95 | 1724 | std | 0.1 | 2.7 | 1 | 9.06E-04 | 3.23E-03 | NIST_27900 | 0 | 0 | KNSTD |
| CH050 | 23.83 | 100.92 | 1631 | std | 0.1 | 2.7 | 1 | 7.22E-04 | 3.18E-03 | NIST_27900 | 0 | 0 | KNSTD |
| CH052 | 24.051 | 100.81 | 1667 | std | 0.1 | 2.7 | 1 | 6.91E-04 | 2.69E-03 | NIST_27900 | 0 | 0 | KNSTD |
| CH053 | 24.063 | 100.84 | 1658 | std | 0.1 | 2.7 | 1 | 6.26E-04 | 2.44E-03 | NIST_27900 | 0 | 0 | KNSTD |
| CH054 | 23.683 | 100.92 | 1728 | std | 0.1 | 2.7 | 1 | 6.93E-04 | 2.29E-03 | NIST_27900 | 0 | 0 | KNSTD |
| CH056 | 24.063 | 100.84 | 1658 | std | 0.1 | 2.7 | 1 | 5.78E-04 | 2.52E-03 | NIST_27900 | 0 | 0 | KNSTD |
| CH058 | 23.996 | 100.85 | 1668 | std | 0.1 | 2.7 | 1 | 6.72E-04 | 2.39E-03 | NIST_27900 | 0 | 0 | KNSTD |
| CH059 | 23.797 | 100.65 | 1699 | std | 0.1 | 2.7 | 1 | 1.08E-05 | 3.04E-03 | NIST_27900 | 0 | 0 | KNSTD |
| CH062 | 21.891 | 100.53 | 1640 | std | 0.1 | 2.7 | 1 | 1.65E-05 | 4.53E-03 | NIST_27900 | 0 | 0 | KNSTD |
| CH063 | 21.892 | 100.52 | 1681 | std | 0.1 | 2.7 | 1 | 1.70E-05 | 4.36E-03 | NIST_27900 | 0 | 0 | KNSTD |
| CH064 | 21.889 | 100.52 | 1656 | std | 0.1 | 2.7 | 1 | 1.80E-05 | 4.43E-03 | NIST_27900 | 0 | 0 | KNSTD |
| CH065 | 21.86 | 100.54 | 1657 | std | 0.1 | 2.7 | 1 | 1.35E-05 | 4.20E-03 | NIST_27900 | 0 | 0 | KNSTD |
| CH066 | 21.83 | 100.57 | 1732 | std | 0.1 | 2.7 | 1 | 2.09E-05 | 4.44E-03 | NIST_27900 | 0 | 0 | KNSTD |
| CH067 | 21.861 | 100.53 | 1599 | std | 0.1 | 2.7 | 1 | 9.61E-04 | 2.94E-03 | NIST_27900 | 0 | 0 | KNSTD |
| CH068 | 21.861 | 100.52 | 1562 | std | 0.1 | 2.7 | 1 | 1.26E-05 | 4.24E-03 | NIST_27900 | 0 | 0 | KNSTD |
| CH069 | 21.747 | 100.45 | 1655 | std | 0.1 | 2.7 | 1 | 1.32E-05 | 4.12E-03 | NIST_27900 | 0 | 0 | KNSTD |
| CH070 | 21.759 | 100.36 | 1560 | std | 0.1 | 2.7 | 1 | 1.19E-05 | 5.17E-03 | NIST_27900 | 0 | 0 | KNSTD |
| CH071 | 21.818 | 100.44 | 1510 | std | 0.1 | 2.7 | 1 | 1.73E-05 | 5.59E-03 | NIST_27900 | 0 | 0 | KNSTD |
| CH075 | 21.919 | 100.36 | 1448 | std | 0.1 | 2.7 | 1 | 1.51E-05 | 3.50E-03 | NIST_27900 | 0 | 0 | KNSTD |
| CH077 | 22.086 | 100.18 | 1644 | std | 0.1 | 2.7 | 1 | 3.72E-05 | 7.77E-03 | NIST_27900 | 0 | 0 | KNSTD |
| CH078 | 22.035 | 100.15 | 1546 | std | 0.1 | 2.7 | 1 | 2.48E-05 | 6.07E-03 | NIST_27900 | 0 | 0 | KNSTD |
| CH079 | 21.951 | 100.17 | 1600 | std | 0.1 | 2.7 | 1 | 1.76E-05 | 8.61E-03 | NIST_27900 | 0 | 0 | KNSTD |
| CH080 | 21.874 | 100.18 | 1711 | std | 0.1 | 2.7 | 1 | 1.90E-05 | 4.70E-03 | NIST_27900 | 0 | 0 | KNSTD |

[a]For more information about required input for CRONUS see the CRONUS documentation at http://hess.ess.washington.edu/

**Table S1.** Input table to CRONUS-Earth Online Calculator for each sample presented in this study. All physiographic properties are calculated from 30 m ASTER GDEM. A complete description of the CRONUS-Earth Online Calculator can be found in *Balco et al.* [2008].

1.1 Column "Sample name," the unique identifier of each sample.

1.2 Column "Mean Latitude," decimal degrees, the mean latitude of the basin represented by the sample.

1.3 Column “Mean Longitude,” decimal degrees, the mean longitude of the basin represented by the sample.

1.4 Column “Effective Elevation,” meters above sea level, the effective elevation of the basin represented by the sample calculated using polynomials from *Lal* [1991].

1.5 Column “Elv/pressure flag,” no units, parameter to select standard elevation-pressure relationship or Antarctic elevation-pressure relationship. Further information can be found in *Stone* [2000].

1.6 Column “Thickness,” cm, thickness of sample. In the case of active channel sediment samples, the thickness is modeled as minimal, at 0.1 cm.

1.7 Column “Density,” g/cm$^3$, assumed density of parent rock material.

1.7 Column “Shielding Correction,” unitless, gives the ratio of the isotope production rate integrated over the entire sample basin to the production rate over the same basin with no cosmic ray obstruction. Here we assume that cosmic ray shielding is insignificant given other studies where significantly steeper and higher-relief catchments result in minimal scaling factors [e.g., *Portenga et al.*, 2015].

1.8 Column “$^{10}$Be,” atoms/g, concentration of 10Be in sample.

1.9 Column “+/-,“ atoms/g, analytical standard deviation of the sample.

1.10 Column “$^{10}$Be Standard,” no units, the standard identifier for the ratio to which the AMS results are standardized.

1.11 Column “$^{26}$Al,” placeholder column for CRONUS-Earth Online Calculator.

1.12 Column “+/-,”placeholder column for CRONUS-Earth Online Calculator.

1.13 Column “$^{26}$Al Standard,” placeholder column for CRONUS-Earth Online Calculator.

**Table S2**. Summary of data for each sample

| Sample ID | Mean Lattitude | Mean Longitude | Nesting Order | Mean Elevation (m) | Mean Slope ($^o$) | Basin Area ($km^2$) | MAP (mm/yr) |
|---|---|---|---|---|---|---|---|
| CH-001 | 27.115 | 99.356 | 6 | 2931 | 19.8 | 198 | 869 |
| CH-003 | 27.049 | 99.384 | 0 | 3104 | 21.1 | 4 | 869 |
| CH-004 | 27.055 | 99.329 | 0 | 2979 | 22.0 | 6 | 869 |
| CH-005 | 27.057 | 99.372 | 1 | 2962 | 20.1 | 16 | 869 |
| CH-009 | 27.056 | 99.359 | 2 | 2949 | 20.5 | 23 | 869 |
| CH-010 | 27.061 | 99.375 | 0 | 3049 | 22.3 | 6 | 869 |
| CH-011 | 27.069 | 99.322 | 0 | 2945 | 21.9 | 8 | 869 |
| CH-012 | 27.062 | 99.351 | 3 | 2928 | 20.9 | 34 | 869 |
| CH-013 | 27.175 | 99.407 | 0 | 3296 | 12.0 | 13 | 869 |
| CH-016 | 27.163 | 99.409 | 1 | 3265 | 14.1 | 18 | 869 |
| CH-017 | 27.127 | 99.431 | 0 | 3191 | 18.0 | 18 | 869 |
| CH-020 | 27.153 | 99.422 | 2 | 3220 | 16.2 | 37 | 869 |
| CH-021 | 27.077 | 99.353 | 4 | 2878 | 20.2 | 63 | 869 |
| CH-023 | 27.115 | 99.377 | 5 | 2948 | 18.9 | 132 | 869 |
| CH-024 | 27.141 | 99.401 | 3 | 3026 | 18.0 | 67 | 869 |
| CH-031 | 24.192 | 100.740 | 0 | 1804 | 22.9 | 90 | 989 |
| CH-032 | 24.115 | 100.740 | 0 | 1823 | 22.6 | 27 | 989 |
| CH-033 | 24.184 | 100.750 | 1 | 1799 | 22.8 | 120 | 989 |
| CH-034 | 24.184 | 100.750 | 1 | 1799 | 22.8 | 120 | 989 |
| CH-035 | 24.261 | 100.810 | 0 | 1831 | 17.9 | 177 | 993 |
| CH-036 | 24.247 | 100.790 | 2 | 1817 | 19.9 | 297 | 991 |
| CH-037 | 24.082 | 100.840 | 0 | 1398 | 14.0 | 7 | 989 |
| CH-039 | 24.177 | 100.810 | 3 | 1698 | 19.1 | 662 | 989 |
| CH-041 | 24.106 | 100.810 | 4 | 1649 | 18.8 | 923 | 1000 |
| CH-042 | 23.875 | 100.600 | 0 | 1828 | 17.9 | 27 | 1084 |
| CH-043 | 23.676 | 100.600 | 0 | 1755 | 20.1 | 17 | 1141 |
| CH-044 | 23.978 | 100.800 | 10 | 1629 | 19.0 | 2508 | 1050 |
| CH-045 | 23.992 | 100.850 | 9 | 1613 | 19.8 | 1877 | 1038 |
| CH-046 | 23.898 | 100.930 | 0 | 1633 | 19.9 | 37 | 1030 |
| CH-047 | 23.894 | 100.960 | 1 | 1714 | 20.2 | 91 | 1022 |
| CH-048 | 23.852 | 100.970 | 0 | 1849 | 20.0 | 31 | 1017 |
| CH-049 | 23.877 | 100.950 | 0 | 1711 | 22.1 | 20 | 1017 |

| | | | | | | | |
|---|---|---|---|---|---|---|---|
| CH-050 | 23.830 | 100.920 | 2 | 1604 | 20.3 | 302 | 1030 |
| CH-052 | 24.051 | 100.810 | 5 | 1635 | 19.0 | 1137 | 1009 |
| CH-053 | 24.063 | 100.840 | 6 | 1627 | 19.3 | 1441 | 1014 |
| CH-054 | 23.683 | 100.920 | 0 | 1699 | 22.6 | 262 | 1104 |
| CH-056 | 24.063 | 100.840 | 7 | 1626 | 19.3 | 1445 | 1014 |
| CH-058 | 23.996 | 100.850 | 8 | 1636 | 19.8 | 1711 | 1028 |
| CH-059 | 23.797 | 100.650 | 1 | 1681 | 16.6 | 624 | 1088 |
| CH-062 | 21.891 | 100.530 | 0 | 1634 | 15.6 | 7 | 1283 |
| CH-063 | 21.892 | 100.520 | 0 | 1678 | 14.9 | 12 | 1283 |
| CH-064 | 21.889 | 100.520 | 1 | 1652 | 15.0 | 20 | 1283 |
| CH-065 | 21.860 | 100.540 | 2 | 1651 | 15.2 | 42 | 1283 |
| CH-066 | 21.830 | 100.570 | 0 | 1727 | 16.1 | 14 | 1283 |
| CH-067 | 21.861 | 100.530 | 3 | 1593 | 15.5 | 95 | 1283 |
| CH-068 | 21.861 | 100.520 | 4 | 1554 | 15.2 | 128 | 1283 |
| CH-069 | 21.747 | 100.450 | 0 | 1651 | 16.2 | 128 | 1282 |
| CH-070 | 21.759 | 100.360 | 0 | 1553 | 16.3 | 38 | 1297 |
| CH-071 | 21.818 | 100.440 | 5 | 1499 | 14.4 | 487 | 1289 |
| CH-075 | 21.919 | 100.360 | 6 | 1435 | 13.5 | 1006 | 1299 |
| CH-077 | 22.086 | 100.180 | 0 | 1633 | 16.4 | 11 | 1325 |
| CH-078 | 22.035 | 100.150 | 0 | 1535 | 15.8 | 18 | 1329 |
| CH-079 | 21.951 | 100.170 | 0 | 1591 | 19.3 | 12 | 1296 |
| CH-080 | 21.874 | 100.180 | 0 | 1697 | 19.0 | 51 | 1297 |

[1] Delivery rate calculated from equation derived by *Graly et al.* [2011]

[2] Land-use reported from values calulcated from GLC30 land cover dataset [Chen et al., 2014]

| | | Catchment $k_{sn}$ | | | | |
|---|---|---|---|---|---|---|
| Sample ID | Basin Relief (m) | Mean | Standard Deviation | Median | $^{10}Be_m$ Delivery Rate ($10^5$ atoms/cm$^2$ yr)[1] | $^{137}$Cs (Bq/kg) |
| CH-001 | 1787 | 158 | 131 | 118 | 9.30 | ± |
| CH-003 | 870 | 114 | 23 | 112 | 9.26 | ± |
| CH-004 | 812 | 90 | 17 | 85 | 9.26 | ± |
| CH-005 | 1006 | 100 | 37 | 95 | 9.26 | ± |
| CH-009 | 1021 | 102 | 40 | 94 | 9.26 | ± |
| CH-010 | 813 | 109 | 38 | 102 | 9.27 | ± |

| | | | | | | | | |
|---|---|---|---|---|---|---|---|---|
| CH-011 | 1086 | 104 | 24 | 99 | 9.27 | | ± | |
| CH-012 | 1099 | 94 | 39 | 89 | 9.27 | | ± | |
| CH-013 | 321 | 33 | 15 | 33 | 9.33 | 4.02 | ± | 0.98 |
| CH-016 | 793 | 168 | 183 | 61 | 9.33 | 4.86 | ± | 1.00 |
| CH-017 | 823 | 148 | 125 | 135 | 9.31 | 2.87 | ± | 1.04 |
| CH-020 | 881 | 177 | 165 | 119 | 9.32 | | ± | |
| CH-021 | 1249 | 113 | 62 | 96 | 9.27 | | ± | |
| CH-023 | 1249 | 129 | 94 | 104 | 9.30 | | ± | |
| CH-024 | 1109 | 150 | 118 | 112 | 9.31 | | ± | |
| CH-031 | 1142 | 100 | 42 | 99 | 8.85 | | ± | |
| CH-032 | 1144 | 109 | 27 | 113 | 8.81 | | ± | |
| CH-033 | 1189 | 109 | 49 | 103 | 8.84 | | ± | |
| CH-034 | 1189 | 109 | 49 | 103 | 8.84 | | ± | |
| CH-035 | 1676 | 138 | 86 | 124 | 8.91 | | ± | |
| CH-036 | 1676 | 126 | 75 | 111 | 8.89 | | ± | |
| CH-037 | 1058 | 52 | 16 | 51 | 8.79 | | ± | |
| CH-039 | 1802 | 108 | 69 | 93 | 8.84 | | ± | |
| CH-041 | 1905 | 112 | 89 | 95 | 8.90 | | ± | |
| CH-042 | 809 | 85 | 31 | 85 | 9.53 | | ± | |
| CH-043 | 784 | 84 | 27 | 72 | 9.93 | | ± | |
| CH-044 | 2006 | 179 | 262 | 103 | 9.28 | | ± | |
| CH-045 | 2006 | 147 | 190 | 103 | 9.18 | | ± | |
| CH-046 | 1088 | 96 | 44 | 88 | 9.07 | | ± | |
| CH-047 | 1246 | 104 | 52 | 92 | 8.99 | | ± | |
| CH-048 | 1142 | 121 | 60 | 101 | 8.93 | | ± | |
| CH-049 | 921 | 100 | 53 | 79 | 8.94 | | ± | |
| CH-050 | 1433 | 126 | 98 | 96 | 9.04 | | ± | |
| CH-052 | 1941 | 143 | 201 | 102 | 8.95 | | ± | |
| CH-053 | 1941 | 140 | 187 | 100 | 9.00 | | ± | |
| CH-054 | 1648 | 126 | 70 | 110 | 9.60 | | ± | |
| CH-056 | 1941 | 140 | 187 | 100 | 9.00 | | ± | |
| CH-058 | 1941 | 138 | 173 | 103 | 9.10 | | ± | |
| CH-059 | 1591 | 248 | 338 | 103 | 9.52 | | ± | |
| CH-062 | 577 | 53 | 28 | 53 | 10.25 | | ± | |
| CH-063 | 470 | 48 | 21 | 51 | 10.25 | | ± | |
| CH-064 | 590 | 53 | 27 | 53 | 10.25 | | ± | |
| CH-065 | 772 | 63 | 32 | 59 | 10.23 | | ± | |
| CH-066 | 724 | 78 | 30 | 78 | 10.22 | | ± | |
| CH-067 | 933 | 67 | 35 | 64 | 10.23 | | ± | |

| | | | | | | |
|---|---|---|---|---|---|---|
| CH-068 | 933 | 64 | 34 | 59 | 10.23 | ± |
| CH-069 | 853 | 125 | 131 | 70 | 10.17 | ± |
| CH-070 | 842 | 68 | 29 | 66 | 10.30 | ± |
| CH-071 | 1004 | 80 | 85 | 57 | 10.26 | ± |
| CH-075 | 1179 | 84 | 147 | 53 | 10.39 | ± |
| CH-077 | 874 | 79 | 13 | 80 | 10.67 | ± |
| CH-078 | 898 | 62 | 18 | 59 | 10.68 | ± |
| CH-079 | 692 | 71 | 22 | 72 | 10.38 | ± |
| CH-080 | 995 | 86 | 40 | 85 | 10.35 | ± |

| Sample ID | $^{210}Pb_{ex}$ (Bq/kg) | $^{10}Be_m$ ($10^7$ atoms/g) | Erosion Index | $^{10}Be_i$ ($10^5$ atoms/g) | Erosion Rate (mm/kyr) |
|---|---|---|---|---|---|
| CH-001 | 7.25 ± 2.50 | 4.85 ± 0.16 | 1.30 ± 0.14 | 1.92 ± 0.07 | 93 ± 8 |
| CH-003 | ± | 11.90 ± 0.24 | 1.22 ± 0.13 | 5.37 ± 0.11 | 35 ± 3 |
| CH-004 | ± | 3.97 ± 0.13 | 1.41 ± 0.14 | 1.49 ± 0.08 | 122 ± 12 |
| CH-005 | ± | 4.15 ± 0.29 | 0.83 ± 0.15 | 2.60 ± 0.08 | 69 ± 6 |
| CH-009 | 2.71 ± 1.15 | 9.39 ± 0.54 | 1.74 ± 0.14 | 2.78 ± 0.10 | 64 ± 5 |
| CH-010 | ± | 68.11 ± 0.61 | 7.55 ± 0.13 | 4.84 ± 0.09 | 38 ± 3 |
| CH-011 | 6.86 ± 3.06 | 2.88 ± 0.24 | 1.76 ± 0.16 | 0.86 ± 0.05 | 209 ± 20 |
| CH-012 | ± | 2.74 ± 0.13 | 0.96 ± 0.14 | 1.47 ± 0.04 | 120 ± 10 |
| CH-013 | 7.93 ± 1.01 | 30.13 ± 0.75 | 1.05 ± 0.13 | 16.74 ± 0.22 | 12 ± 1 |
| CH-016 | 6.70 ± 1.05 | 28.74 ± 1.62 | 1.01 ± 0.14 | 16.20 ± 0.21 | 12 ± 1 |
| CH-017 | 5.07 ± 2.16 | 12.99 ± 1.35 | 1.30 ± 0.17 | 5.72 ± 0.18 | 34 ± 3 |
| CH-020 | 4.64 ± 0.92 | 11.26 ± 0.50 | 0.98 ± 0.14 | 6.63 ± 0.11 | 30 ± 2 |
| CH-021 | ± | 6.39 ± 0.50 | 0.93 ± 0.15 | 3.40 ± 0.07 | 50 ± 4 |
| CH-023 | 6.35 ± 1.30 | 12.53 ± 0.54 | 0.66 ± 0.14 | 9.47 ± 0.12 | 18 ± 1 |
| CH-024 | 6.04 ± 2.51 | 13.50 ± 0.70 | 0.68 ± 0.14 | 10.32 ± 0.12 | 17 ± 1 |
| CH-031 | 3.67 ± 1.69 | 1.87 ± 0.05 | 0.74 ± 0.13 | 0.72 ± 0.03 | 130 ± 11 |
| CH-032 | ± | 1.01 ± 0.11 | 0.60 ± 0.17 | 0.49 ± 0.02 | 193 ± 16 |
| CH-033 | 4.38 ± 1.55 | 1.03 ± 0.11 | 0.41 ± 0.17 | 0.72 ± 0.03 | 129 ± 10 |
| CH-034 | ± | 1.04 ± 0.12 | 0.51 ± 0.17 | 0.59 ± 0.02 | 160 ± 13 |
| CH-035 | ± | 1.05 ± 0.11 | 0.38 ± 0.16 | 0.80 ± 0.03 | 119 ± 9 |
| CH-036 | 3.60 ± 1.72 | 0.97 ± 0.11 | 0.49 ± 0.17 | 0.58 ± 0.03 | 166 ± 15 |
| CH-037 | 2.33 ± 0.63 | 2.23 ± 0.11 | 0.55 ± 0.14 | 0.93 ± 0.04 | 80 ± 6 |
| CH-039 | 3.43 ± 0.86 | 0.77 ± 0.11 | 0.26 ± 0.19 | 0.81 ± 0.03 | 109 ± 9 |

| | | | | | | | | | | | | | | | | |
|---|---|---|---|---|---|---|---|---|---|---|---|---|---|---|---|---|
| CH-041 | 4.02 | ± | 1.85 | 0.57 | ± | 0.10 | 0.28 | ± | 0.22 | 0.53 | ± | 0.02 | 165 | ± | 13 |
| CH-042 | 7.33 | ± | 1.65 | 1.68 | ± | 0.13 | 0.27 | ± | 0.15 | 1.63 | ± | 0.04 | 57 | ± | 4 |
| CH-043 | 6.43 | ± | 1.48 | 1.36 | ± | 0.11 | 0.20 | ± | 0.15 | 1.60 | ± | 0.04 | 55 | ± | 4 |
| CH-044 | 4.22 | ± | 1.61 | 0.84 | ± | 0.03 | 0.26 | ± | 0.13 | 0.81 | ± | 0.03 | 106 | ± | 8 |
| CH-045 | 6.89 | ± | 1.84 | 0.79 | ± | 0.03 | 0.33 | ± | 0.14 | 0.61 | ± | 0.03 | 140 | ± | 12 |
| CH-046 | | ± | | 1.39 | ± | 0.04 | 0.42 | ± | 0.13 | 0.84 | ± | 0.03 | 101 | ± | 8 |
| CH-047 | 4.55 | ± | 2.20 | 1.84 | ± | 0.04 | 0.62 | ± | 0.13 | 0.79 | ± | 0.03 | 113 | ± | 9 |
| CH-048 | 8.52 | ± | 2.92 | 1.64 | ± | 0.19 | 0.44 | ± | 0.17 | 1.07 | ± | 0.03 | 89 | ± | 7 |
| CH-049 | 5.84 | ± | 1.96 | 1.47 | ± | 0.13 | 0.43 | ± | 0.15 | 0.91 | ± | 0.03 | 97 | ± | 8 |
| CH-050 | 4.56 | ± | 1.93 | 1.02 | ± | 0.11 | 0.35 | ± | 0.17 | 0.72 | ± | 0.03 | 116 | ± | 9 |
| CH-052 | | ± | | 0.65 | ± | 0.14 | 0.24 | ± | 0.25 | 0.69 | ± | 0.03 | 125 | ± | 10 |
| CH-053 | 5.44 | ± | 1.80 | 0.83 | ± | 0.03 | 0.34 | ± | 0.13 | 0.63 | ± | 0.02 | 137 | ± | 11 |
| CH-054 | 6.33 | ± | 2.07 | 1.32 | ± | 0.03 | 0.47 | ± | 0.13 | 0.69 | ± | 0.02 | 128 | ± | 10 |
| CH-056 | 5.28 | ± | 1.71 | 0.77 | ± | 0.03 | 0.34 | ± | 0.13 | 0.58 | ± | 0.03 | 149 | ± | 12 |
| CH-058 | 7.84 | ± | 1.78 | 0.95 | ± | 0.03 | 0.36 | ± | 0.13 | 0.67 | ± | 0.02 | 128 | ± | 10 |
| CH-059 | 4.89 | ± | 1.51 | 0.71 | ± | 0.03 | 0.16 | ± | 0.13 | 1.08 | ± | 0.03 | 80 | ± | 6 |
| CH-062 | 9.94 | ± | 2.91 | 2.07 | ± | 0.11 | 0.26 | ± | 0.14 | 1.65 | ± | 0.05 | 48 | ± | 4 |
| CH-063 | 6.79 | ± | 2.68 | 1.72 | ± | 0.12 | 0.22 | ± | 0.14 | 1.70 | ± | 0.04 | 48 | ± | 4 |
| CH-064 | 11.72 | ± | 2.67 | 1.25 | ± | 0.11 | 0.15 | ± | 0.15 | 1.80 | ± | 0.04 | 45 | ± | 3 |
| CH-065 | 14.10 | ± | 2.59 | 1.66 | ± | 0.12 | 0.26 | ± | 0.15 | 1.35 | ± | 0.04 | 60 | ± | 5 |
| CH-066 | 9.78 | ± | 2.86 | 2.58 | ± | 0.07 | 0.27 | ± | 0.13 | 2.09 | ± | 0.04 | 40 | ± | 3 |
| CH-067 | 10.61 | ± | 3.28 | 1.61 | ± | 0.11 | 0.35 | ± | 0.14 | 0.96 | ± | 0.03 | 83 | ± | 6 |
| CH-068 | | ± | | 4.82 | ± | 0.14 | 0.78 | ± | 0.13 | 1.26 | ± | 0.04 | 61 | ± | 5 |
| CH-069 | 6.02 | ± | 2.48 | 2.44 | ± | 0.12 | 0.40 | ± | 0.13 | 1.32 | ± | 0.04 | 61 | ± | 5 |
| CH-070 | 8.27 | ± | 3.28 | 2.51 | ± | 0.12 | 0.43 | ± | 0.14 | 1.19 | ± | 0.05 | 65 | ± | 5 |
| CH-071 | 15.60 | ± | 4.20 | 4.11 | ± | 0.13 | 0.46 | ± | 0.13 | 1.73 | ± | 0.06 | 43 | ± | 3 |
| CH-075 | | ± | | 6.07 | ± | 0.14 | 0.75 | ± | 0.13 | 1.51 | ± | 0.04 | 48 | ± | 3 |
| CH-077 | 5.17 | ± | 2.03 | 2.81 | ± | 0.12 | 0.15 | ± | 0.13 | 3.72 | ± | 0.08 | 21 | ± | 2 |
| CH-078 | 6.50 | ± | 0.82 | 1.16 | ± | 0.11 | 0.09 | ± | 0.16 | 2.48 | ± | 0.06 | 30 | ± | 2 |
| CH-079 | | ± | | 5.15 | ± | 0.13 | 0.59 | ± | 0.13 | 1.76 | ± | 0.09 | 44 | ± | 4 |
| CH-080 | 11.84 | ± | 2.43 | 6.68 | ± | 0.13 | 0.76 | ± | 0.13 | 1.90 | ± | 0.05 | 43 | ± | 3 |

| | Land-use (percent of total area)[2] | | | | | | |
|---|---|---|---|---|---|---|---|
| Sample ID | Cultivated | Forest | Grassland | Shrubland | Wetland | Water | Artificial |
| CH-001 | 15 | 62 | 8 | 15 | 0 | 0 | 0 |

| | | | | | | | |
|---|---|---|---|---|---|---|---|
| CH-003 | 9 | 80 | 1 | 10 | 0 | 0 | 0 |
| CH-004 | 7 | 79 | 3 | 11 | 0 | 0 | 0 |
| CH-005 | 14 | 65 | 4 | 16 | 0 | 0 | 0 |
| CH-009 | 14 | 68 | 4 | 14 | 0 | 0 | 0 |
| CH-010 | 5 | 71 | 5 | 19 | 0 | 0 | 0 |
| CH-011 | 13 | 72 | 4 | 10 | 0 | 0 | 0 |
| CH-012 | 13 | 70 | 4 | 13 | 0 | 0 | 0 |
| CH-013 | 10 | 38 | 24 | 27 | 0 | 0 | 0 |
| CH-016 | 8 | 44 | 22 | 27 | 0 | 0 | 0 |
| CH-017 | 6 | 48 | 11 | 35 | 0 | 0 | 0 |
| CH-020 | 7 | 46 | 16 | 31 | 0 | 0 | 0 |
| CH-021 | 14 | 69 | 4 | 13 | 0 | 0 | 0 |
| CH-023 | 15 | 61 | 7 | 17 | 0 | 0 | 0 |
| CH-024 | 14 | 53 | 11 | 22 | 0 | 0 | 0 |
| CH-031 | 38 | 62 | 0 | 0 | 0 | 0 | 0 |
| CH-032 | 23 | 77 | 0 | 0 | 0 | 0 | 0 |
| CH-033 | 34 | 66 | 0 | 0 | 0 | 0 | 0 |
| CH-034 | 34 | 66 | 0 | 0 | 0 | 0 | 0 |
| CH-035 | 20 | 80 | 0 | 0 | 0 | 0 | 0 |
| CH-036 | 26 | 74 | 0 | 0 | 0 | 0 | 0 |
| CH-037 | 35 | 65 | 0 | 0 | 0 | 0 | 0 |
| CH-039 | 26 | 74 | 0 | 0 | 0 | 0 | 0 |
| CH-041 | 25 | 75 | 0 | 0 | 0 | 0 | 0 |
| CH-042 | 13 | 87 | 0 | 0 | 0 | 0 | 0 |
| CH-043 | 6 | 94 | 0 | 0 | 0 | 0 | 0 |
| CH-044 | 22 | 77 | 0 | 0 | 0 | 0 | 0 |
| CH-045 | 23 | 76 | 0 | 0 | 0 | 0 | 0 |
| CH-046 | 26 | 72 | 0 | 0 | 0 | 1 | 0 |
| CH-047 | 22 | 77 | 0 | 0 | 0 | 1 | 0 |
| CH-048 | 20 | 79 | 0 | 0 | 0 | 0 | 0 |
| CH-049 | 11 | 89 | 0 | 0 | 0 | 0 | 0 |
| CH-050 | 24 | 76 | 0 | 0 | 0 | 0 | 0 |
| CH-052 | 24 | 75 | 0 | 0 | 0 | 0 | 0 |
| CH-053 | 24 | 75 | 0 | 0 | 0 | 0 | 0 |
| CH-054 | 18 | 82 | 0 | 0 | 0 | 0 | 0 |
| CH-056 | 24 | 75 | 0 | 0 | 0 | 0 | 0 |
| CH-058 | 23 | 76 | 0 | 0 | 0 | 0 | 0 |
| CH-059 | 19 | 81 | 0 | 0 | 0 | 0 | 0 |
| CH-062 | 25 | 47 | 28 | 0 | 0 | 0 | 0 |

| | | | | | | | |
|---|---|---|---|---|---|---|---|
| CH-063 | 52 | 37 | 11 | 0 | 0 | 0 | 0 |
| CH-064 | 44 | 39 | 17 | 0 | 0 | 0 | 0 |
| CH-065 | 34 | 45 | 21 | 0 | 0 | 0 | 0 |
| CH-066 | 5 | 65 | 29 | 1 | 0 | 0 | 0 |
| CH-067 | 36 | 34 | 28 | 1 | 0 | 0 | 0 |
| CH-068 | 33 | 35 | 32 | 1 | 0 | 0 | 0 |
| CH-069 | 13 | 44 | 37 | 4 | 0 | 1 | 0 |
| CH-070 | 29 | 37 | 33 | 1 | 0 | 0 | 0 |
| CH-071 | 38 | 33 | 26 | 2 | 0 | 0 | 1 |
| CH-075 | 48 | 35 | 14 | 1 | 0 | 1 | 1 |
| CH-077 | 56 | 44 | 0 | 0 | 0 | 0 | 0 |
| CH-078 | 52 | 48 | 0 | 0 | 0 | 0 | 0 |
| CH-079 | 53 | 47 | 0 | 0 | 0 | 0 | 0 |
| CH-080 | 33 | 56 | 9 | 0 | 0 | 1 | 0 |

**Table S2.** Summary of physiographic characteristics, isotopic results, interpreted values, and land-use for each sample.

2.1 Column "Sample ID," no units, the unique identifier for each sample.

2.2 Column "Mean Latitude," decimal degrees, the calculated mean latitude of each basin.

2.3 Column "Mean Longitude," decimal degrees, the calculated mean longitude of each basin.

2.4 Column "Nesting Order," no units, the order in which the samples nest. Samples with no other samples upstream are assigned a nesting order of 0, and increase in increments of 1 with each additional sample upstream.

2.5 Column "Mean Elevation," meters above sea level, the calculated mean elevation of each sample basin.

2.6 Column "Mean Slope," degrees, the calculated mean slope of each basin.

2.7 Column "Basin Area," $km^2$, the area of the entire contributing landscape upstream of the sample location.

2.8 Column "MAP," mm/yr, the mean annual rainfall for the entire contributing area upstream of a sample location, as calculated from APHRODITE APRHO_MA_V1101.

2.9 Column “Basin Relief,” meters, the total difference in elevation between the highest point upstream of the sample location and the sample location.

2.10 Columns “Catchment $k_{sn}$,” $m^{0.9}$, the mean, standard deviation, and median $k_{sn}$ values for each basin as calculated from the DEM.

2.11 Column “$^{10}Be_m$ Delivery Rate,” atoms/$cm^2$ x yr, the estimated number of $^{10}Be$ atoms per unit area delivered through precipitation each year to the entire area upstream of the sample. Delivery rate was estimated using the empirical equation derived by *Graly et al.* [2011].

2.12 Column “$^{137}Cs$,” Bq/kg, the measured activity of $^{137}Cs$ in each sample. Error is reported as 1 SD. Samples left blank contained no measureable $^{137}Cs$.

2.13 Column “$^{210}Pb_{ex}$,” Bq/kg, the measured activity of $^{210}Pb_{ex}$ in each sample. Error is reported as 1 SD. Samples left blank contained no measurable $^{210}Pb_{ex}$.

2.14 Column “$^{10}Be_m$,” atoms/g, the concentration of meteoric $^{10}Be$ measured in each sample. Error is reported as 1 SD.

2.15 Column “Erosion Index,” unitless, the calculated erosion index for each sample. Errors are reported as 1 SD.

2.16 Column “$^{10}Be_i$,” atoms/g, the measured concentration of $^{10}Be_i$ in each sample. Errors are reported as 1 SD.

2.17 Column “Erosion Rate,” mm/kyr, average rate of landscape lowering for the entire area upstream of the sample location as interpreted using information from Table S1 and the CRONUS-Earth Online Calculator. Errors are reported as 1 SD.

2.18 Columns “Land-use,” unitless, the fraction (expressed as a percent) of the total contributing area occupied by a given land-use. Land-use is calculated using the GLC30 land-cover dataset [*Chen et al.*, 2014].

**Table S3.** Matrix of bivariate regression statistics for samples in basin 49

| | Land-use | | Climate | | Topography | | | | | | | |
|---|---|---|---|---|---|---|---|---|---|---|---|---|
| | Fraction Cultivated Land | | MAP (mm/yr) | | Mean Slope ($^o$) | | Mean $k_{sn}$ | | Median $k_{sn}$ | | Basin Relief | |
| | $R^2$ | p-value | $R^2$ | p-value | $R^2$ | p-value | $R^2$ | p-value | $R^2$ | p-value | $R^2$ | p-value |
| $^{210}Pb_{ex}$[1] | 0.35 | 0.007 | | | | | | | | | | |
| $^{10}Be_m$ | | | | | | | 0.41 | 0.001 | 0.33 | 0.003 | 0.55 | <0.0001 |
| Erosion Index | 0.27 | 0.01 | 0.23 | 0.02 | 0.18 | 0.04 | 0.22 | 0.02 | | | | |
| Erosion Rate | 0.21 | 0.02 | 0.35 | 0.002 | 0.21 | 0.03 | | | 0.36 | 0.002 | 0.20 | 0.03 |

[1] Excludes samples below detection limit

**Table S3.** Matrix of $R^2$ and p-values for bivariate regressions shown in in Figure 13 comparing isotopic concentration and isotopically derived values with land-use, climate and topographic metrics. Regressions without significant statistics are not included.

3.1 Column 1, row label showing isotopic system or isotopic derivative considered.

3.2 Colum "Land-use," shows regression statistics for linear bivariate regressions between the fraction cultivated land and a given isotope or isotopic derivative.

3.2 Column "Climate," shows regression statistics for linear bivariate regressions between the mean annual precipitation and a given isotope or isotopic derivative.

3.3 Columns "Topography," shows regression statistics for linear bivariate regressions between each topographic metric and a given isotope or isotopic derivative.

**Table S4.** Summary mixing data

| Junction ID | Downstream Sample | Upstream Samples | Fraction Difference in Agricultural Land Between Contributing Basins | Fraction Agricultural Land Upstream of Junction |
|---|---|---|---|---|
| 35-1 | CH-023 | CH-021, 024 | 0.00 | 0.15 |
| 35-2 | CH-020 | CH-016, 017 | 0.02 | 0.07 |
| 35-3 | CH-012 | CH-009, 011 | 0.01 | 0.13 |
| 35-4 | CH-009 | CH-004, 005 | 0.07 | 0.14 |
| 35-5 | CH-005 | CH-003, 010 | 0.04 | 0.14 |
| 49-1 | CH-044 | CH-045, 059 | 0.04 | 0.22 |
| 49-2 | CH-058 | CH-054, 056 | 0.06 | 0.23 |
| 49-3 | CH-053 | CH-050, 052 | 0.00 | 0.24 |
| 49-4 | CH-047 | CH-046, 048, 049 | 0.10 | 0.22 |
| 49-5 | CH-036 | CH-034, 035 | 0.14 | 0.26 |
| 49-6 | CH-033 | CH-031, 032 | 0.15 | 0.34 |
| 11-1 | CH-065 | CH-064, 066 | 0.39 | 0.34 |
| 11-2 | CH-064 | CH-062, 063 | 0.27 | 0.44 |

| Junction ID | Residual Area ($km^2$) | Fraction Residual Area | Distance Below Junction (m) |
|---|---|---|---|
| 35-1 | 2 | 0.02 | 230 |
| 35-2 | 1 | 0.03 | 220 |
| 35-3 | 3 | 0.09 | 170 |
| 35-4 | 1 | 0.04 | 250 |
| 35-5 | 6 | 0.38 | 160 |
| 49-1 | 7 | 0.00 | 1650 |
| 49-2 | 4 | 0.00 | 510 |
| 49-3 | 2 | 0.00 | 150 |
| 49-4 | 3 | 0.03 | 150 |
| 49-5 | 0 | 0.00 | 100 |
| 49-6 | 3 | 0.03 | 270 |
| 11-1 | 8 | 0.19 | 820 |
| 11-2 | 1 | 0.05 | 370 |

Measured Values

| Junction ID | $^{10}Be_i$ Concentration ($10^5$ atoms/g) | $^{10}Be_m$ Concentration ($10^7$ atoms/g) | $^{210}Pb_{ex}$ Activity (Bq/kg) |
|---|---|---|---|
| 35-1 | 9.47 ± 0.12 | 12.50 ± 0.54 | 5.64 ± 1.30 |
| 35-2 | 6.63 ± 0.11 | 11.30 ± 0.50 | 3.93 ± 0.92 |
| 35-3 | 1.47 ± 0.04 | 2.74 ± 0.13 | 0.00 ± 0.00 |
| 35-4 | 2.78 ± 0.10 | 9.39 ± 0.54 | ± |
| 35-5 | 2.60 ± 0.08 | 4.15 ± 0.29 | ± |
| 49-1 | 0.81 ± 0.03 | 0.84 ± 0.03 | 3.73 ± 1.61 |
| 49-2 | 0.67 ± 0.02 | 0.95 ± 0.03 | 7.24 ± 1.78 |
| 49-3 | 0.63 ± 0.02 | 0.83 ± 0.03 | 4.82 ± 1.80 |
| 49-4 | 0.79 ± 0.03 | 1.84 ± 0.04 | ± |
| 49-5 | 0.58 ± 0.03 | 0.97 ± 0.11 | ± |
| 49-6 | 0.72 ± 0.03 | 1.03 ± 0.12 | 3.74 ± 1.55 |
| 11-1 | 1.35 ± 0.04 | 1.66 ± 0.12 | 13.40 ± 2.59 |
| 11-2 | 1.80 ± 0.04 | 1.25 ± 0.11 | 11.10 ± 2.67 |

| | Modeled Values | | | | |
|---|---|---|---|---|---|
| Junction ID | $^{10}Be_i$ Concentration ($10^5$ atoms/g) | $^{10}Be_m$ Concentration ($10^7$ atoms/g) | $^{210}Pb_{ex}$ Activity (Bq/kg) | Ratio Measured/Modeled $^{10}Be_i$ | Ratio Measured/Modeled $^{10}Be_m$ |
| 35-1 | 5.26 ± 0.31 | 8.30 ± 0.44 | 1.43 ± 0.69 | 0.80 ± 0.11 | 0.51 ± 0.10 |
| 35-2 | 8.46 ± 0.52 | 17.11 ± 1.14 | 4.80 ± 1.62 | -0.22 ± 0.05 | -0.34 ± 0.05 |
| 35-3 | 1.75 ± 0.16 | 5.92 ± 0.35 | 3.32 ± 1.64 | -0.16 ± 0.08 | -0.54 ± 0.04 |
| 35-4 | 2.16 ± 0.13 | 4.08 ± 0.18 | ± | 0.29 ± 0.09 | 1.30 ± 0.17 |
| 35-5 | 5.04 ± 0.12 | 46.65 ± 1.57 | ± | -0.48 ± 0.02 | -0.91 ± 0.01 |
| 49-1 | 0.68 ± 0.04 | 0.78 ± 0.02 | 5.94 ± 1.57 | 0.18 ± 0.08 | 0.08 ± 0.05 |
| 49-2 | 0.59 ± 0.03 | 0.84 ± 0.03 | 4.81 ± 1.51 | 0.13 ± 0.07 | 0.13 ± 0.05 |
| 49-3 | 0.70 ± 0.03 | 0.72 ± 0.11 | 0.78 ± 0.39 | -0.10 ± 0.05 | 0.14 ± 0.18 |
| 49-4 | 0.93 ± 0.04 | 1.49 ± 0.07 | 3.37 ± 1.06 | -0.15 ± 0.05 | 0.24 ± 0.06 |
| 49-5 | 0.70 ± 0.03 | 1.05 ± 0.08 | ± | -0.18 ± 0.06 | -0.07 ± 0.12 |
| 49-6 | 0.65 ± 0.04 | 1.61 ± 0.05 | ± | 0.11 ± 0.07 | -0.36 ± 0.07 |
| 11-1 | 1.91 ± 0.05 | 1.76 ± 0.08 | 10.33 ± 1.98 | -0.29 ± 0.03 | -0.06 ± 0.08 |
| 11-2 | 1.68 ± 0.05 | 1.85 ± 0.09 | 7.29 ± 2.00 | 0.07 ± 0.04 | -0.32 ± 0.07 |

**Table S4.** Summary of land-use and residual area upstream of stream junctions and results of mixing model analysis for each isotope.

4.1 Column 1, “Junction ID,” no units, the assigned label for each junction. The prefix indicates the basin ID, and the junctions are generally labeled with XX-1 at the outlet and higher numbers further upstream in the basin.

4.2 Column 2, “Downstream Sample,” no units, the ID of the sample collected below the junction.

4.3 Column 3, “Upstream Samples,” no units, the ID of the samples collected above the junction.

4.4 Colum 4, “Fraction Difference in Agricultural Land Between Contributing Basins,” unitless, the ratio of the fraction cultivated land for each upstream watershed. At junction 49-4 samples CH-048 and -049 were consolidated.

4.5 Column 5, “Fraction Agricultural Land Upstream of Junction,” unitless, the total fraction of land under cultivation upstream of the junction.

4.6 Column 6, “Residual Area,” $km^2$, the difference in contributing area between the sum of the upstream sample areas and the downstream sample area.

4.7 Column 7, “Fraction Residual Area,” unitless, the ration of the residual area to the total area upstream of the sample collected below the junction.

4.8 Column 8, “Distance Below Junction,” meters, the distance along the channel below the junction a downstream sample is located. Calculated based on the location of the junction as represented by stream lines created from the DEM.

4.9 Column 9, “Measured Values,” various units, the header for the columns representing the isotopic concentration measured in samples collected below each junction. All errors reported as 1 SD.

4.9.1 “$^{10}Be_i$ Concentration,” $10^5$ atoms/g, the concentration of $^{10}Be_i$ in the sample collected below the stream junction.

4.9.2 “$^{10}Be_m$ Concentration,” $10^7$ atoms/g, the concentration of $^{10}Be_m$ in the sample collected below the stream junction.

4.9.3 “$^{210}Pb_{ex}$ Activity,” Bq/kg, the activity of $^{210}Pb_{ex}$ in the sample collected below the stream junction. Blank cells indicate junctions where one of more samples at the junction was below the detection limit.

4.10 Column 10, “Modeled Values,” various units, the header for the columns representing the modeled isotopic concentration below each junction. All errors are reported as 1 SD.

4.10.1 "$^{10}Be_i$ Concentration," $10^5$ atoms/g, the modeled concentration of $^{10}Be_i$ below the stream junction.

4.10.2 "$^{10}Be_m$ Concentration," $10^7$ atoms/g, the modeled concentration of $^{10}Be_m$ below the stream junction.

4.10.3 "$^{210}Pb_{ex}$ Activity," Bq/kg, the modeled activity of $^{210}Pb_{ex}$ below the stream junction. Blank cells indicate junctions where one of more samples at the junction was below the detection limit.

4.11 Colum 11, "Ratio Measured/Modeled $^{10}Be_i$," unitless, the ratio of the measured concentration of $^{10}Be_i$ below the junction to the modeled concentration. Error is reported as 1 SD, and samples where the error at 2 SD is within ~5% of the ratio are considered well mixed.

4.12 Colum 12, "Ratio Measured/Modeled $^{10}Be_m$," unitless, the ratio of the measured concentration of $^{10}Be_m$ below the junction to the modeled concentration. Error is reported as 1 SD, and samples where the error at 2 SD is within ~5% of the ratio are considered well mixed.

References

Balco, G., J. O. Stone, N. A. Lifton, and T. J. Dunai (2008), A complete and easily accessible means of calculating surface exposure ages or erosion rates from $^{10}$Be and $^{26}$Al measurements, *Quaternary Geochronology*, *3*, 174-195.

Chen, J., J. Chen, A. Liao, X. Cao, L. Chen, X. Chen, C. He, G. Han, S. Peng, and M. Lu (2014), Global land cover mapping at 30m resolution: A POK-based operational approach, *ISPRS Journal of Photogrammetry and Remote Sensing*.

Graly, J. A., L. J. Reusser, and P. R. Bierman (2011), Short and long-term delivery rates of meteoric $^{10}$Be to terrestrial soils, *Earth and Planetary Science Letters*, *302*(3–4), 329-336.

Jull, A. J. T., E. M. Scott, and P. Bierman (2015), The CRONUS-Earth inter-comparison for cosmogenic isotope analysis, *Quaternary Geochronology*(0).

Kohl, C. P., and K. Nishiizumi (1992), Chemical isolation of quartz for measurement of *in-situ* -produced cosmogenic nuclides, *Geochimica et Cosmochimica Acta*, *56*, 3583-3587.

Lal, D. (1991), Cosmic ray labeling of erosion surfaces: *In situ* nuclide production rates and erosion models, *Earth and Planetary Science Letters*, *104*(2-4), 424-439.

Portenga, E. W., P. R. Bierman, C. Duncan, L. B. Corbett, N. M. Kehrwald, and D. H. Rood (2015), Erosion rates of the Bhutanese Himalaya determined using in situ-produced 10Be, *Geomorphology*, *233*(0), 112-126.

Stone, J. O. (2000), Air pressure and cosmogenic isotope production, *Journal of Geophysical Research*, *105*(b10), 23753-23759.

# Appendix B: Sample Site Log

The following appendix contains a log of the samples used in this research. The samples included in this log are as follows:

| | | |
|---|---|---|
| CH-001 | CH-034 | CH-056 |
| CH-003 | CH-035 | CH-058 |
| CH-004 | CH-036 | CH-059 |
| CH-005 | CH-037 | CH-062 |
| CH-009 | CH-039 | CH-063 |
| CH-010 | CH-041 | CH-064 |
| CH-011 | CH-042 | CH-065 |
| CH-012 | CH-043 | CH-066 |
| CH-013 | CH-044 | CH-067 |
| CH-016 | CH-045 | CH-068 |
| CH-017 | CH-046 | CH-069 |
| CH-020 | CH-047 | CH-070 |
| CH-021 | CH-048 | CH-071 |
| CH-023 | CH-049 | CH-075 |
| CH-024 | CH-050 | CH-077 |
| CH-031 | CH-052 | CH-078 |
| CH-032 | CH-053 | CH-079 |
| CH-033 | CH-054 | CH-080 |

**Key:**

*Photo of sample site, usually oreinted looking upstream*

**CH-0XX** – *Sample ID*

**Parent Basin:** *ID of the basin the sample was collected in (either 35, 49, or 11)*
**Collection Date:** *Date the sample was collected*
**Latitude: Longitude:** *Latitude and Longitude of sample site location (WGS 84, decimal degrees)*
**Sample Type:** "*RS" indicates active channel sediment, "O" indicates active channel sediment but sample also represents the outlet of the parent basin (i.e. basin 35, 49 or 11).*
**Additional Notes:** *Any additional information regarding sample location, channel features, unusual settings, etc.*

**CH-001**

**Parent Basin:** 35
**Collection Date:** 5/23/13
**Latitude:** 27.156 **Longitude:** 99.321
**Sample Type:** Outlet
**Additional Notes:** Located at sediment gauging site for basin 35.

**CH-003**

**Parent Basin:** 35
**Collection Date:** 5/25/13
**Latitude:** 27.055 **Longitude:** 99.360
**Sample Type:** RS
**Additional Notes:** Channel is heavily laden with sediment, agricultural field just above channel on river right hillslope upstream of sample location.

**CH-004**

**Parent Basin:** 35
**Collection Date:** 5/25/13
**Latitude:** 27.059 **Longitude:** 99.350
**Sample Type:** RS
**Additional Notes:** Channel shares valley floor with small road, which sometimes occupies the active river channel.

**CH-005**

**Parent Basin:** 35
**Collection Date:** 5/25/13
**Latitude:** 27.064 **Longitude:** 99.351
**Sample Type:** RS
**Additional Notes:** Braided channel surrounded by agricultural fields ~2.5 meters above river level. 2.5 m tall cut-bank downstream of sample site.

**CH-009**

**Parent Basin:** 35
**Collection Date:** 5/25/13
**Latitude:** 27.070 **Longitude:** 99.350
**Sample Type:** RS
**Additional Notes:** Sample collected immediately after confined section of channel.

**CH-010**

**Parent Basin:** 35
**Collection Date:** 5/25/13
**Latitude:** 27.064 **Longitude:** 99.358
**Sample Type:** RS
**Additional Notes:** Sample collected in channel ~50 m upstream of 5 m tall sediment check dam. A road crosses the channel just below the sample site.

**CH-011**

**Parent Basin:** 35
**Collection Date:** 5/25/13
**Latitude:** 27.074 **Longitude:** 99.351
**Sample Type:** RS
**Additional Notes:** Confined channel surrounded by agricultural fields.

**CH-012**

**Parent Basin:** 35
**Collection Date:** 5/25/13
**Latitude:** 27.075 **Longitude:** 99.352
**Sample Type:** RS
**Additional Notes:** Sample taken at head of reservoir during reservoir low-stand. Channel was obviously altered by people moving sediment.

**CH-013**

**Parent Basin:** 35
**Collection Date:** 5/26/13
**Latitude:** 27.155 **Longitude:** 99.414
**Sample Type:** RS
**Additional Notes:** Channel drains low-relief high elevation pasture.

**CH-016**

**Parent Basin:** 35
**Collection Date:** 5/26/13
**Latitude:** 27.132 **Longitude:** 99.408
**Sample Type:** RS
**Additional Notes:** Sample collected immediately below very steep heavily incised canyon containing a major knickzone separating CH-016 from CH-013 further upstream.

**CH-017**

**Parent Basin:** 35
**Collection Date:** 5/26/13
**Latitude:** 27.131 **Longitude:** 99.406
**Sample Type:** RS
**Additional Notes:** Steep mountain stream emerging below knickzone.

**CH-020**

**Parent Basin:** 35
**Collection Date:** 5/26/13
**Latitude:** 27.132 **Longitude:** 99.406
**Sample Type:** RS
**Additional Notes:** Steep boulder choked channel below junction of streams sampled by CH-016 and -017.

**CH-021**

**Parent Basin:** 35
**Collection Date:** 5/27/13
**Latitude:** 27.118 **Longitude:** 99.354
**Sample Type:** RS
**Additional Notes:** Braided channel at outlet of S. Arm of basin 35, above junction with N. Arm.

**CH-023**

**Parent Basin:** 35
**Collection Date:** 5/27/13
**Latitude:** 27.121 **Longitude:** 99.353
**Sample Type:** RS
**Additional Notes:** Sample collected from below junction of S. and N. Arms.

**CH-024**

**Parent Basin:** 35
**Collection Date:** 5/27/13
**Latitude:** 27.122 **Longitude:** 99.362
**Sample Type:** RS
**Additional Notes:** Sample from outlet of N. Arm above junction with S. Arm.

**CH-031**

**Parent Basin:** 49
**Collection Date:** 5/30/13
**Latitude:** 24.134 **Longitude:** 100.778
**Sample Type:** RS
**Additional Notes:** Channel surrounded by steep hillsides with some very steep agricultural fields

**CH-032**

**Parent Basin:** 49
**Collection Date:** 5/30/13
**Latitude:** 24.130 **Longitude:** 100.779
**Sample Type:** RS
**Additional Notes:** Similar stream setting to CH-031

**CH-033**

**Parent Basin:** 49
**Collection Date:** 5/30/13
**Latitude:** 24.130 **Longitude:** 100.781
**Sample Type:** RS
**Additional Notes:** Sample collected immediately below junction of streams sampled by CH-031 and -032

**CH-034**

**Parent Basin:** 49
**Collection Date:** 5/30/13
**Latitude:** 24.129 **Longitude:** 100.798
**Sample Type:** RS
**Additional Notes:** Collected a short distance below CH-033, a small old landslide scar was identified between CH-033 and this sample, motivating the collection of this sample so close to CH-033.


**CH-035**

**Parent Basin:** 49
**Collection Date:** 5/30/13
**Latitude:** 24.129 **Longitude:** 100.800
**Sample Type:** RS
**Additional Notes:** Collected on upper main stem of Weiyuan River.

**CH-036**

**Parent Basin:** 49
**Collection Date:** 5/30/13
**Latitude:** 24.126 **Longitude:** 100.799
**Sample Type:** RS
**Additional Notes:** Collected below junction of streams sampled by CH-035 and -034.


**CH-037**

**Parent Basin:** 49
**Collection Date:** 5/30/13
**Latitude:** 24.060 **Longitude:** 100.808
**Sample Type:** RS
**Additional Notes:** Small drainage with extensive agriculture immediately upstream of sample site.

**CH-039**

**Parent Basin:** 49
**Collection Date:** 5/30/13
**Latitude:** 23.980 **Longitude:** 100.799
**Sample Type:** RS
**Additional Notes:** Main-stem sample of Weiyuan River, surrounded by agriculture.

**CH-041**

**Parent Basin:** 49
**Collection Date:** 5/31/13
**Latitude:** 23.858 **Longitude:** 100.814
**Sample Type:** RS
**Additional Notes:** Main stem sample of Weiyuan River.

**CH-042**

**Parent Basin:** 49
**Collection Date:** 6/1/13
**Latitude:** 23.852 **Longitude:** 100.636
**Sample Type:** RS
**Additional Notes:** Tributary stream to W. arm of basin 49, sampled at outlet of gorge.

**CH-043**

**Parent Basin:** 49
**Collection Date:** 6/1/13
**Latitude:** 23.695 **Longitude:** 100.634
**Sample Type:** RS
**Additional Notes:** Small tributary of W. arm of basin 49, sampled above a series of sandstone ledges.

**CH-044**

**Parent Basin:** 49
**Collection Date:** 6/1/13
**Latitude:** 23.546 **Longitude:** 100.717
**Sample Type:** O
**Additional Notes:** Outlet of basin 49, collected at the sediment gauging station

**CH-045**

**Parent Basin:** 49
**Collection Date:** 6/1/13
**Latitude:** 23.569 **Longitude:** 100.717
**Sample Type:** RS
**Additional Notes:** Sample near outlet of main stem, above junction with W. arm.

**CH-046**

**Parent Basin:** 49
**Collection Date:** 6/2/13
**Latitude:** 23.848 **Longitude:** 100.903
**Sample Type:** RS
**Additional Notes:** Small stream in E. arm of basin 49

**CH-047**

**Parent Basin:** 49
**Collection Date:** 6/2/13
**Latitude:** 23.845 **Longitude:** 100.902
**Sample Type:** RS
**Additional Notes:** Sample collected below triple junction of CH-046, -048, and -049.

**CH-048**

**Parent Basin:** 49
**Collection Date:** 6/2/13
**Latitude:** 23.844 **Longitude:** 100.927
**Sample Type:** RS
**Additional Notes:** Small stream in E. arm above junction with CH-047. Boulder filled channel.

**CH-049**

**Parent Basin:** 49
**Collection Date:** 6/2/13
**Latitude:** 23.845 **Longitude:** 100.925
**Sample Type:** RS
**Additional Notes:** Small stream in E. arm of basin 49 above junction with CH-047.

**CH-050**

**Parent Basin:** 49
**Collection Date:** 6/2/13
**Latitude:** 23.726 **Longitude:** 100.830
**Sample Type:** RS
**Additional Notes:** Sample on E. arm immediately above junction with main stem.

**CH-052**

**Parent Basin:** 49
**Collection Date:** 6/2/13
**Latitude:** 23.729 **Longitude:** 100.824
**Sample Type:** RS
**Additional Notes:** Main stem sample immediately above junction with E. arm.

**CH-053**

**Parent Basin:** 49
**Collection Date:** 6/2/13
**Latitude:** 23.721 **Longitude:** 100.825
**Sample Type:** RS
**Additional Notes:** Sample collected below junction of E. arm and main stem.

**CH-054**

**Parent Basin:** 49
**Collection Date:** 6/3/13
**Latitude:** 23.695 **Longitude:** 100.823
**Sample Type:** RS
**Additional Notes:** Large tributary to main stem below junction of E. arm and main stem.

**CH-056**

**Parent Basin:** 49
**Collection Date:** 6/3/13
**Latitude:** 23.700 **Longitude:** 100.816
**Sample Type:** RS
**Additional Notes:** Main stem sample above junction with CH-054.

**CH-058**

**Parent Basin:** 49
**Collection Date:** 6/3/13
**Latitude:** 23.692 **Longitude:** 100.814
**Sample Type:** RS
**Additional Notes:** Sample below junction of streams sampled by CH-054 and -056

**CH-059**

**Parent Basin:** 49
**Collection Date:** 6/3/13
**Latitude:** 23.566 **Longitude:** 100.702
**Sample Type:** RS
**Additional Notes:** Outlet of W. arm just upstream of junction with main stem.

**CH-062**

**Parent Basin:** 11
**Collection Date:** 6/5/13
**Latitude:** 21.873 **Longitude:** 100.543
**Sample Type:** RS
**Additional Notes:** Small incised channel surrounded by sugar and rice paddies.

**CH-063**

**Parent Basin:** 11
**Collection Date:** 6/5/13
**Latitude:** 21.871 **Longitude:** 100.542
**Sample Type:** RS
**Additional Notes:** Small incised channel surrounded by sugar and rice paddies.

**CH-064**

**Parent Basin:** 11
**Collection Date:** 6/5/13
**Latitude:** 21.869 **Longitude:** 100.544
**Sample Type:** RS
**Additional Notes:** Sample below junction of samples CH-062 and -063.

**CH-065**

**Parent Basin:** 11
**Collection Date:** 6/5/13
**Latitude:** 21.851 **Longitude:** 100.547
**Sample Type:** RS
**Additional Notes:** Sample below junction of CH-064 and -066.

**CH-066**

**Parent Basin:** 11
**Collection Date:** 6/5/13
**Latitude:** 21.848 **Longitude:** 100.558
**Sample Type:** RS
**Additional Notes:** Small slightly steeper stream upstream of junction with CH-064.

**CH-067**

**Parent Basin:** 11
**Collection Date:** 6/6/13
**Latitude:** 21.835 **Longitude:** 100.472
**Sample Type:** RS
**Additional Notes:** Sample collected along upper portion of S. arm, some gravel mining upstream.

**CH-068**

**Parent Basin:** 11
**Collection Date:** 6/6/13
**Latitude:** 21.829 **Longitude:** 100.448
**Sample Type:** RS
**Additional Notes:** Sample below CH-067 on S. arm in heavily incised channel.

**CH-069**

**Parent Basin:** 11
**Collection Date:** 6/6/13
**Latitude:** 21.798 **Longitude:** 100.424
**Sample Type:** RS
**Additional Notes:** Major tributary to S. arm of basin 11.

**CH-070**

**Parent Basin:** 11
**Collection Date:** 6/6/13
**Latitude:** 21.794 **Longitude:** 100.367
**Sample Type:** RS
**Additional Notes:** Moderate sized tributary to S. arm of basin 11.

**CH-071**

**Parent Basin:** 11
**Collection Date:** 6/7/13
**Latitude:** 21.944 **Longitude:** 100.341
**Sample Type:** RS
**Additional Notes:** Sample from S. arm upstream of junction with N. arm of basin 11.

**CH-075**

**Parent Basin:** 11
**Collection Date:** 6/8/13
**Latitude:** 21.952 **Longitude:** 100.425
**Sample Type:** O
**Additional Notes:** Outlet of basin 11 from near sediment gauging station.

**CH-077**

**Parent Basin:** 11
**Collection Date:** 6/8/13
**Latitude:** 22.073 **Longitude:** 100.183
**Sample Type:** RS
**Additional Notes:** Small stream draining northern portion of basin 11. Surround by tea plantation.

**CH-078**

**Parent Basin:** 11
**Collection Date:** 6/8/13
**Latitude:** 22.049 **Longitude:** 100.173
**Sample Type:** RS
**Additional Notes:** Small tributary in NW portion of basin 11. Sample from immediately above a small diversion structure.

**CH-079**

**Parent Basin:** 11
**Collection Date:** 6/8/13
**Latitude:** 21.958 **Longitude:** 100.179
**Sample Type:** RS
**Additional Notes:** Small tributary of N. arm of basin 11 with anabranching channel. Sample collected from immediately above small diversion structure.

**CH-080**

**Parent Basin:** 11
**Collection Date:** 6/8/13
**Latitude:** 21.883 **Longitude:** 100.223
**Sample Type:** RS
**Additional Notes:** Sample from ~1-2 km below large dam on westernmost portion of N. arm.